Determination of the energy scale uncertainty for the measurement of F_2 at low values of Q^2 using the H1 detector

dem Fachbereich Physik
der Universität Dortmund
zur Erlangung des akademischen Grades
eines Doktors der Naturwissenschaften
vorgelegte

Dissertation

von

MSc. Phys. Andrea del Rocio Vargas Treviño
aus Puebla (Mexico)

Dortmund July 2006

Abstract – Kurzfassung – Resumen

Systematic studies for the measurement of the cross section measurement of the $ep \to e'X$ reaction and for the extraction of the proton structure function $F_2(x, Q^2)$ are performed. The data sample analyzed has a luminosity of $450\,\mathrm{nb}^{-1}$ and corresponds to a special data taking period taken in the year 2000, where the interaction point of the ep scattering was moved from its nominal position. In order to minimize the total systematic error of the measurement, detailed studies concerning the calibration of the main calorimeters of the H1 detector are required. Such studies and their influence on the cross section measurement are the main subject of the thesis. The kinematic region of the measurement has values of $9.5 \times 10^{-6} < x < 8.0 \times 10^{-3}$ and $0.2 < Q^2 < 3.5\,\mathrm{GeV}^2$ and extends the kinematic coverage of the previous shifted vertex analysis based on data taken by the H1 detector in the year 1995. Also, the total systematic error is significantly reduced in comparison to the previous shifted vertex analysis.

In dieser Analyse werden die systematischen Fehler zur Messung des Wirkungsquerschnitts $ep \to e'X$ und der Extraktion der Protonstrukturfunktion $F_2(x, Q^2)$ untersucht. Analysiert wird eine spezielle Datennahmeperiode, die mit dem H1 Detektor im Jahre 2000 genommen wurde. Der Wechselwirkungspunk ist von der nominellen Position verschoben, so daß kleinere Werte von Q^2 erreichbar sind. Die gesamte Luminosität der Datanahmeperiode beträgt $450\,\mathrm{nb}^{-1}$. Um die systematischen Fehler des Wirkungsquerschnitts zu minimieren, ist eine preäzise Kalibrierung der Kalorimeter notwendig, die einen Schwerpunkt dieser Arbeit darstellt. Die Messung des Wirkungsquerschnitts umfaßt einen Wertebereich von $9.5 \times 10^{-6} < x < 8.0 \times 10^{-3}$ und $0.2 < Q^2 < 3.5\,\mathrm{GeV}^2$ und erreicht eine verbesserte Präzision im Vergleich zu einer vorherigen Messung, die mit Daten des 1995 Jahres durchgefürhrt wurde.

En el presente trabajo se realizan estudios sistematicos para medir la sección eficaz del proceso $ep \to e'X$ y para la extracción de la función de estructura de el protón $F_2(x, Q^2)$. El intervalo cinemático corresponde a valores de $9.5 \times 10^{-6} < x < 8.0 \times 10^{-3}$ y $0.2 < Q^2 < 3.5\,\mathrm{GeV}^2$. Los datos analizados corresponden a un período especial tomado en el año 2000. El punto de interacción entre el electrón y el protón es movido de su posición nominal con el próposito de obtener pequeños valores de Q^2. La medida de la sección eficaz y la extracción de la función de estructura de el proton require de una detallada calibración de los principales calorímetros de el detector H1. La calibración y la determinación de los errores sistematicos son parte del análisis realizado en el presente trabajo. La sección eficaz aqui medida extiende las mediciones realizadas con datos tomados con el detector H1 en el año 1995. La precisión de la medicion aqui realizada supera las mediciones previas.

Contents

Chapter 1

Introduction

One of the most amazing questions in physics is how matter is composed and created. One method used to investigate the structure of the matter, uses the scattering of elementary particles. Since electrons seem to be elemental they have been used to probe the structure of the matter. For example one needs electrons of few keV of energy to resolve the size of the atom better than 1A (10^{-10}m). In order to discover the structure of the nucleus one has to resolve distances of approximately 1 fermi. These distances can be studied using the scattering of nucleus with electrons having an energy of a few hundred of MeV.

Similar to the nucleus structure one can probe the structure of the proton using electrons with a few GeV of energy. In the electron energy spectrum of such ep collisions there is an elastic peak in which the proton recoils as a whole and secondary peaks appear due to the excitation of the proton into various higher-mass N^* resonant states. After the resonance region a continuum distribution is observed and this corresponds to those electrons which have been scattered by the constituents of the proton, now known as *quarks*.

The suggestion that the protons and neutrons could be composed of more basic objects called "quarks" was made in 1964 by Gell-Mann and Zweig [1]. Experiments to probe the structure of the proton by scattering electrons began at Stanford in the late 1960 and there it was revealed that protons contain point-like constituents. It was Feynman [2] who called them "partons" and only after the identification of the "partons" with "quarks" it was possible to establish the first two of the three families which summaries the standard model of particles.

Deep inelastic scattering has thus played an important role in the development of the standard model of particles. In this thesis the structure of the proton is studied using also the deep inelastic scattering of electrons with protons. In order to understand the kinematic region explored, the most important variables and experimental results of DIS will be summarized in

the following sections.

1.1 Deep inelastic scattering

The generic diagram of the electron proton scattering is shown in Fig. 1.1, where k and p represent the four momemtum of the incoming electron and proton, respectively. The four momentum of the outcoming lepton is denoted by k' while P_x represent the four momentum of the hadronic final state. Depending on which vector boson V^* is exchanged, the electron proton scattering can be divided in Neutral Current (NC) and Charge Current processes (CC).

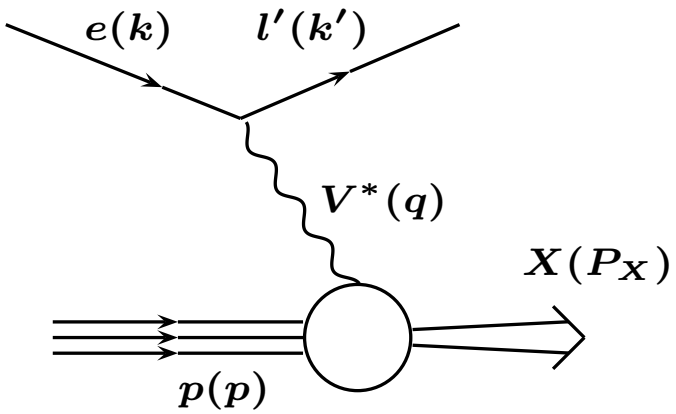

Figure 1.1: Schematic diagram of lepton proton scattering via vector-boson exchange

In case a CC process occurs a charged boson $W^{\pm}$ mediates the electron proton interaction, producing a neutrino as the outcoming lepton. In NC events a neutral boson (γ or Z^0) is exchanged, and then an scattered lepton is observed in the final state. While CC events are produced purely by weak interaction, the NC events will be dominated by the electromagnetic interaction for low values of the virtuality $Q = \sqrt{-(k-k')^2}$.

The kinematic of the electron-proton reaction is usually described by the following Lorentz-invariant quantities:

- The center of mass energy of the electron proton interaction,

$$s = (p+k)^2 \tag{1.1}$$

- The invariant mass squared of the virtual exchanged boson,

$$Q^2 = -q^2 \tag{1.2}$$

- The Bjorken x variable, which is interpreted in the lowest order of QCD, as the fraction of the momentum of the incoming proton taken by the struck quark,

$$x = \frac{Q^2}{2p \cdot q} \tag{1.3}$$

- The inelasticity y, which gives a measure of the amount of energy transferred between the electron and the proton.

$$y = \frac{p \cdot q}{p \cdot k} \tag{1.4}$$

Due its definition x and y vary in the interval $[0, 1]$. Ignoring the electron and proton masses, from Eqs.1.2, 1.3, 1.4 follows:

$$Q^2 \approx sxy \tag{1.5}$$

therefore only two of these quantities are independent, and then the ep scattering can be described in terms of s, Q^2 and x.

An additional variable used to describe the hadronic final state is the center of mass energy of the γp system:

$$\begin{aligned} W^2 &= (q+p)^2 = P_x^2 \\ &= Q^2 \frac{1-x}{x} + m_p^2 \end{aligned}$$

One speaks of deep inelastic scattering of electron proton collisions, if the virtuality $\sqrt{Q^2}$ of the exchanded boson is above the proton mass and if the center of mass energy of the γp system goes beyond the resonance domain $W^2 >> m_p^2$.

If we concentrate on NC processes in the region where the photon exchange dominates ($Q^2 < 100\,\mathrm{GeV}^2$) then the amplitude of the $ep \to eX$ reaction is proportional to

$$\mathcal{A} \propto \frac{1}{q^2} L_{\mu\nu} W^{\mu\nu}$$

where $L_{\mu\nu}$ is the leptonic tensor which describes the interaction between the electron and the photon and is calculable throught QED. $W^{\mu\nu}$ is the hadronic tensor associated to the γp vertex.

In contrast to the leptonic tensor $L_{\mu\nu}$, the exact form of the current in the hadronic vertex can not be calculated. The hadronic tensor $W^{\mu\nu}$ has to be parametrized in terms of so called proton structure functions. The proton structure functions will describe the $\gamma p \rightarrow X$ transition. For NC processes only two arbitrary functions F_2, F_1 depending on x and Q^2 are relevant [4, 5].

The differential cross section for $ep \rightarrow eX$ is given by:

$$\frac{d^2\sigma}{dxdQ^2} = k \left[F_2(x, Q^2) - \frac{y^2}{Y_+} F_L(x, Q^2) \right] \tag{1.6}$$

where

$$Y_+ = 1 + (1 - y)^2 \qquad k = \frac{2\pi\alpha^2}{Q^4 x} Y_+$$
$$F_L = F_2 - 2xF_1$$

Thus the proton structure functions can be obtained from the experiment if the cross section, gets measured differentially in Q^2 and x. One useful quantity is obtained from Eq. 1.6, absorving the kinematic factor k, and is known as the reduced cross section σ_{red}.

$$\sigma_{red} = F_2(x, Q^2) - \frac{y^2}{Y_+} F_L(x, Q^2) \tag{1.7}$$

1.1.1 The Naive Quark Parton Model

The quark parton model (QPM) introduced by Feynman in 1969 [2] provides a simple physical interpretation of the electron proton scattering. This model considers that at large values of Q^2 the γp interaction can be expressed as the sum of incoherent scattering from point like quark constituents which behaves as free inside the proton during the interaction. This picture can only be correct if the scattering process occurs over a short time scale during which the photon sees a frozen state of non interacting quarks [3].

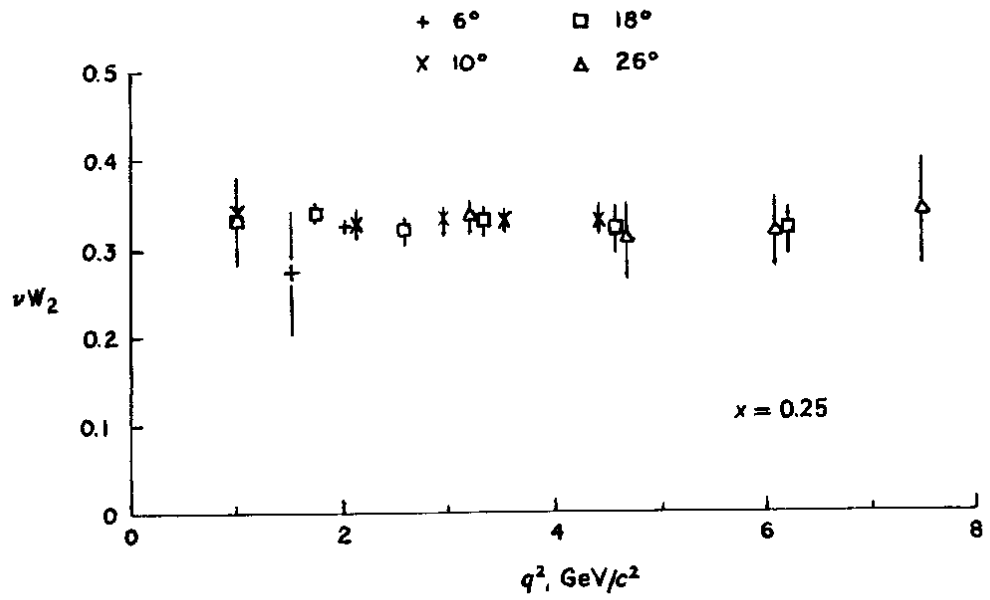

Figure 1.2: The $\nu F_2 = F_2$ structure function as function of Q^2 at fixed $x = 0.25$, as it was measured by the SLAC-MIT group [6]

Let f_i be the probability to find a quark-i in the proton with a fraction χ of the proton momentum. If the quarks do not interact with each other, and assuming partons of spin 0, then the total ep cross section can be expressed as:

$$\begin{aligned}
\frac{d^2\sigma}{dxdQ^2} &= \sum_i \int d\chi f_i(\chi) \left(\frac{d^2\sigma_i}{dxdQ^2}\right)_{eq_i \to eq_i} \\
&= \sum_i \int d\chi f_i(\chi) \frac{4\pi\alpha^2}{Q^4} \frac{e_i^2}{2} [1 + (1-y)^2] \delta(x - \chi) \\
&= \sum_i \frac{2\pi\alpha^2}{Q^4} e_i^2 Y_+ f_i(x) \qquad (1.8)
\end{aligned}$$

where in Eq. 1.8 the elastic $eq_i \to eq_i$ cross section have been introduced.

Comparing the two ep cross section formulae in Eqs. 1.8, 1.6 it follows that:

$$F_2(x, Q^2) = \sum_i f_i(x) x e_{qi}^2 \qquad (1.9)$$

The QPM predicts that F_2 is a function of x only, a phenomenon known as *scaling*. Fig. 1.2 shows the measurement of F_2 as function of Q^2 performed by the SLAC group. The relation $F_2(x) = 2xF_1(x)$ was derived by Callan-Gross [15], representing a direct consequence of the spin $1/2$ of the quarks.

Soon after the SLAC experiments were performed the violation of the scale was observed in muon nucleon [7] scattering and later confirmed by neutrino nucleon scattering experiments [8, 10]. It was not clear how to reconcile the picture of the free partons into the experimental observations.

1.2 The QCD improved parton model

Altough the QPM provides a simple picture of the electron proton scattering and can describe the scaling behaviour of the SLAC and Gargamelle data [9], it was not able to explain the scaling violation behavior observed afterwards. Also it can not explain the fact that quarks are not detected as free particles but always build bound systems as observed in hadron spectra experiments, a phenomenon called "confinement". It turns out that the QPM is the lowest order approximation of a more general theory known as Quantum Chromodynamics (QCD).

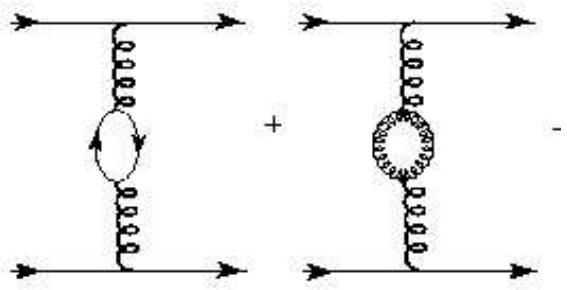

Figure 1.3: Loop diagrams illustrating the interaction between quarks and gluons.

QCD is a non-abelian theory based on the symmetry group $SU(3)_c$, there quarks besides electric charge, also carry "color charge" which can be of three types "red, green, blue". The interaction between quarks is mediated through the exchange of one of the eight-gluons which generate the symmetry group. The gluons play a equivalent role as the photons in QED do, but contrary to the photons, the interaction between gluons is possible. Therefore within QCD, the interaction between quarks considers diagrams as shown in Fig. 1.3. The contributions of the loop diagrams to any amplitude diverge but can be resummed introducing a Q^2 dependence of the coupling between the quarks and gluons α_s. Formally this behaviour is known as the "running" of the strong coupling constant, which in the leading order logarithmic approximation is

given by:

$$\alpha_s(Q^2) = \frac{12\pi}{(33 - 2N_f)\ln(Q^2/\Lambda^2)} \tag{1.10}$$

where N_f is the number of quarks flavours with the mass $m_q^2 < Q^2$, and $\Lambda \approx 100MeV$ determines the energy scale at which α_s becomes large.

Two important limits are deduced from Eq. 1.10. Since momentum is related to distance due to the uncertainty principle, at low momentum the coupling between quarks is leading to quark *confinement*. An opposite behaviour is seen at high Q^2, since α_s becomes small meaning that the coupling between quarks is weak and therefore can be treated as nearly free particles [11, 12]. The running of the strong coupling constant α_s is able to describe at the same time the experimental results of confinement related to the existence of hadron spectra and asymptotic freedom seen in DIS experiments. Note however that confinement has not been proven exactly to follow from Eq. 1.10.

The introduction of gluons in QCD changed the picture of the proton and the interpretation of the ep interaction as follows. The proton is composed of three "valence quarks" which interact throught the exchange of gluons. The gluons can produce quark-antiquark pairs also known as "sea quarks" and radiation of gluons due to their self-interaction is possible.

At lowest order, QCD reproduces the QPM picture of the interaction, but considering the first order of the α_s expansion (LO), the calculations of the ep cross section involve integrals which are divergent and have to be resummed (renormalized) as in the case of α_s. This resummation introduces a "mass factorization scale" which separates the short distance partonic effects from the long distance hadronic effects. The choise of the separation is arbitrary and in case the DIS scheme is used, then:

$$F_2(x, Q^2) = \sum_i e_i^2 x q_i(x, Q^2) \tag{1.11}$$

and contrary to the QPM, F_2 depends on x and Q^2. The parton distribution $q_i(x, Q^2)$ in Eq. 1.11 can not be predicted. But the requirement that they should not depend on the "factorization scale" leads to the prediction of its evolution in Q^2, which in leading order can be written as:

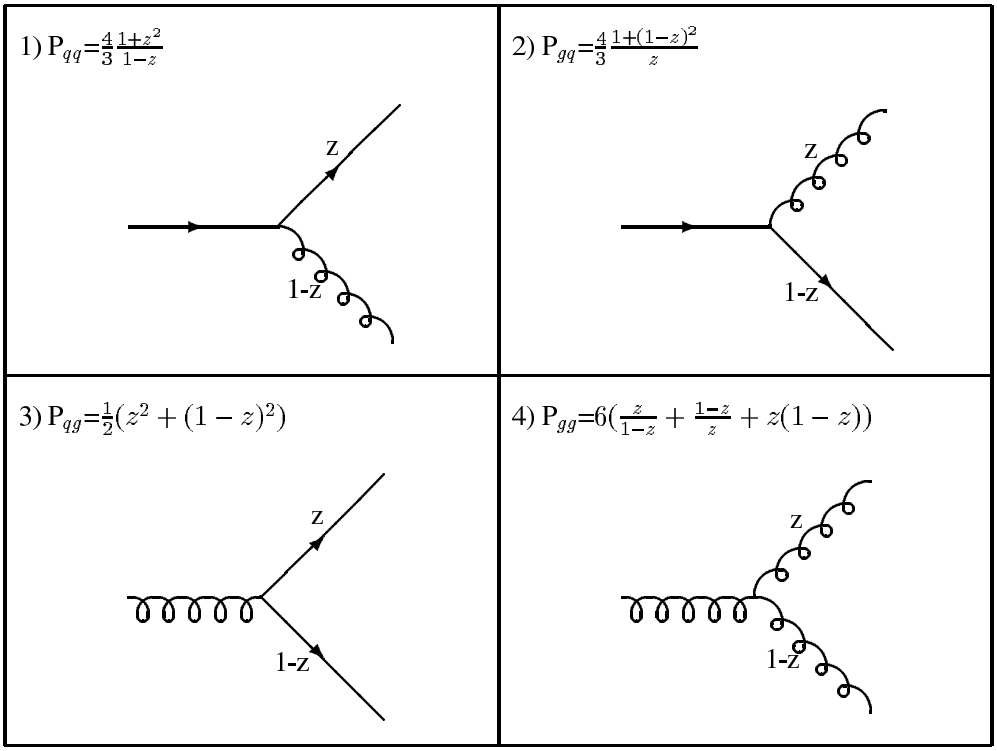

Figure 1.4: Splitting functions

$$\frac{\partial q_i(x,Q^2)}{\partial \ln Q^2} = \frac{\alpha_S(Q^2)}{2\pi}\int_x^1 \frac{dz}{z}\left[\sum_j q_j(z,Q^2)P_{ij}^{(0)}\left(\frac{x}{z}\right) + g(z,Q^2)P_{ig}^{(0)}\left(\frac{x}{z}\right)\right] \tag{1.12}$$

where the functions P_{ij} and P_{ig} are known as splitting functions. In LO the splitting functions have a natural physical meaning e.g., P_{ij} is the probability that a quark i with momentum z radiates a gluon with $1-z$ of its momentum. Since quarks are coupled to gluons, the evolution of the gluon density function is also required and is given by:

$$\frac{\partial g(x,Q^2)}{\partial \ln Q^2} = \frac{\alpha_S(Q^2)}{2\pi}\int_x^1 \frac{dz}{z}\left[\sum_j q_j(z,Q^2)P_{gj}^{(0)}\left(\frac{x}{z}\right) + g(z,Q^2)P_{gg}^{(0)}\left(\frac{x}{z}\right)\right] \tag{1.13}$$

where P_{gj}, P_{gg} are the probability that a gluon splits in a quark antiquark pair or split to 2 gluons (see Fig 1.4). The set of equations 1.12, 1.13 are known as Altarelli Parisi equations [13, 14]. The evolution of the parton distribution function on x is not predicted, but for a given scale Q^2 its

dependence on x can be parametrized using the counting rules. The free parameters of the parametrization will be determined using the measured data over several order of magnitude of x and Q^2. There are several parametrizations used, by example Glueck, Reya and Vogt (GRV) [17], Martin,Ryskin,Sterling and Thorne MRST [18] and die CTEQ group [19].

Using this picture of the proton, the phenomenon of scaling violations observed at several experiments is one of the most important successes of QCD. Fig 1.5 shows the measurement of F_2 as function of Q^2 for different values of x. A good agreement is found between the measured data which cover almost five orders of magnitude in Q^2 with the predictions of pQCD. As it can be seen from Fig. 1.5 the lower values of x are accessed mainly at low values of Q^2. This kinematical region will be discussed in the next sections.

1.3 The behavoiur of the cross section at low Q^2

At low values of $Q^2 < 1\,\mathrm{GeV}^2$, pQCD can not predict the behaviour of the electron proton scattering since the strong coupling constant α_s is large. This kinematic domain can only be investigated in terms of phenomenological models and hadron-hadron descriptions like Regge theory.

A powefull method used to investigate the behaviour of F_2 at very low Q^2 proceeds via its connection to the total $\gamma^* p$ cross section.

$$\sigma_{tot}^{\gamma^* p} = \frac{4\pi^2\alpha}{Q^2} F_2(W^2, Q^2) \tag{1.14}$$

thus the electron can be seen as a source of quasi real photons which interact with the proton. This is almost a hadron hadron interaction which can be studied in terms of Regge theory.

1.3.1 Introduction to Regge theory

Regge theory investigates the dynamics of hadrons by studying the two particle scattering $A + B \to C + D$ (see Fig. 1.6) [20]. The physical idea is to relate the high energy behaviour of the $s-$channel amplitude to the quantum numbers that are exchanged in the $t-$channel. Instead of considering the exchange of single particles as QCD does, Regge theory considers the exchange of a complete trajectory of particles $\alpha(t)$ having the *same internal quantum number* (strangeness,

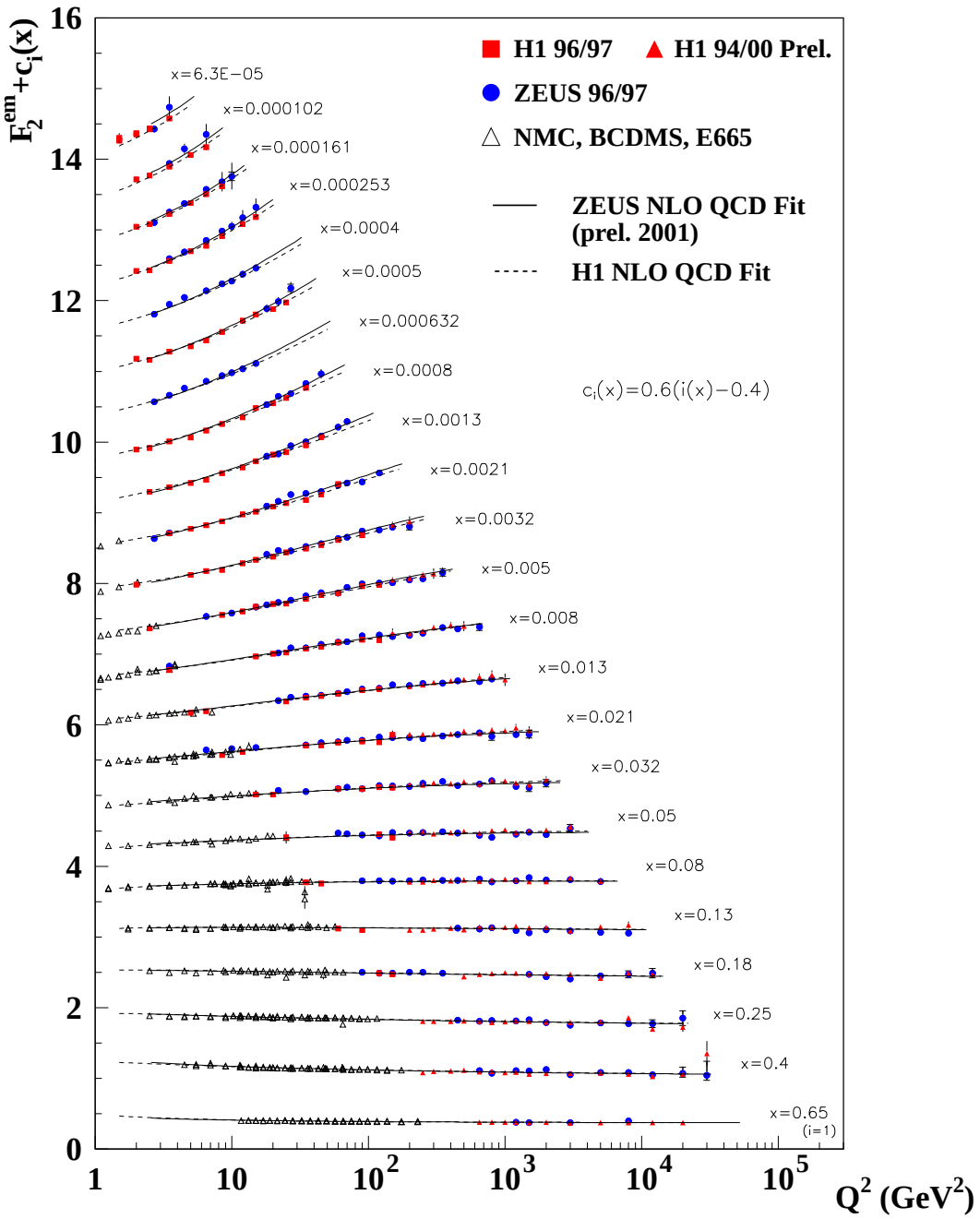

Figure 1.5: Scaling violations measured in lepton proton scattering experiments [21, 22, 23, 24, 25, 26, 27, 28].

isospin, bayon number, etc) but *different spin*. The particles lying on a Regge-trayectory relate their spin (J) and mass (m) such that in good aproximation $m^2 = J$.

In order to describe the total hadron-hadron cross section (σ_{tot}) measurements, two universal

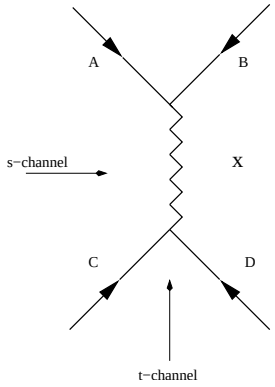

Figure 1.6: Contributions to the reaction $A + B \rightarrow B + C$ in the t-channel from a Reggeon or Pomeron trajectory $\alpha(t)$

trajectories known as Pomeron (α_P) and Reggeon (α_R) are needed. A Reggeon exchange usually is related with a exchange of quantum numbers, while a pomeron exchange involves the exchange of the vacuum quantum numbers. Donnachie and Landshoff (1992) [29] performed a global fit to all existing hadron-hadron total cross section data and discovered that all Reggeon intercepts can be represented by one effective intercept having a value of $\alpha_R(0) \approx 0.5$. In order to reproduce the rising behaviour of the hadron-hadron cross section at high energies, DL parametrized the Pomeron intercept as $\alpha_P(0) = 1 + \epsilon$ obtaining a value of ϵ varying between $[0.08, 0.09]$. Following this ideas, the total cross section of any hadron-hadron interaction can be written as:

$$\sigma_i^{tot}(s) = A_i^P s^{\alpha_P(0)-1} + A_i^R s^{\alpha_R(0)-1} \tag{1.15}$$

where the coefficients A_i, B_i dependend on the process under study and on Q^2. Donnachie and Landshoff (1993) [30] showed that the Pomeron plus Reggeon exchange model could as well describe successfully the existing data on $\sigma_{tot}^{\gamma^* p}$ up to values of $Q^2 \leq 10$ GeV^2. The measurement at high energies of the total photoproduction cross section at $Q^2 \approx 0\,\text{GeV}^2$,was performed by HERA in 1992 [31], and the measurement was fully in agreement with the Regge theory prediction.

This result has an important impact on the proton structure function F_2 at low x, since F_2 is related to the total $\gamma^* p$ cross section (see Eq. 1.14) and then, the Regge description of DL predicts a rise of F_2 at low x as:

$$F_2 \propto x^{-0.08} = x^{-\lambda}$$

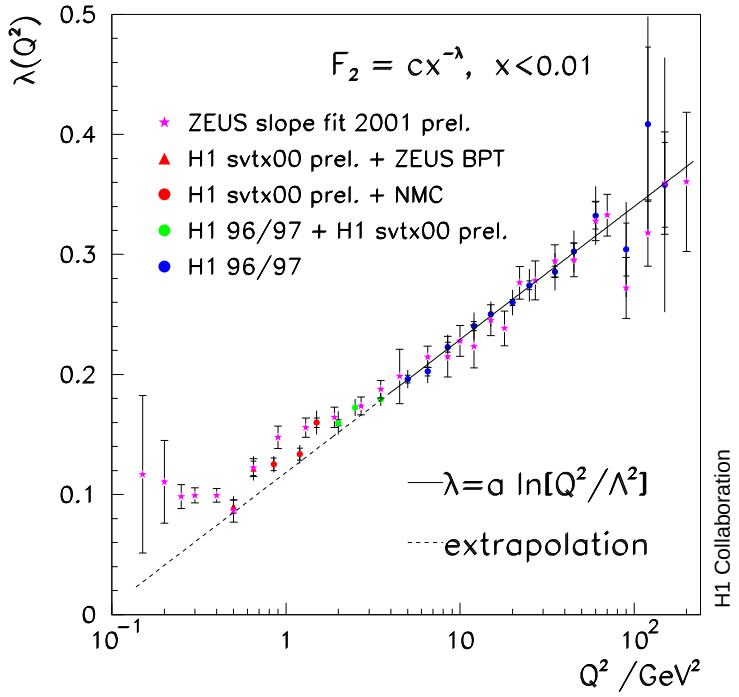

Figure 1.7: Fits of the rise λ of F_2 parametrized at low x as $cx^{-\lambda}$ [32]

H1 and ZEUS collaborations have measured the proton structure function $F_2(x, Q^2)$ over a large range of values of x, Q^2, and therefore the rise λ can be derived from the derivative of F_2 for differents values of Q^2 and for low x ($x < 0.02$).

$$\left[\frac{\partial \ln F_2(x, Q^2)}{\partial \ln x}\right]_{Q^2} = -\lambda(x, Q^2)$$

The measurements of the rise λ are summarized in Fig. 1.7 [32]. One can clearly see that the predicted value of $\alpha_P(0) \approx 0.08$ of Regge theory is compatible with the data for the region of low $Q^2 < 0.5\,\mathrm{GeV}^2$. On the other hand, the rise of F_2 is well described by pQCD for values of $Q^2 > 1.5\,\mathrm{GeV}^2$.

1.3.2 The behaviour of F_2 in the transition region

The model of Donnachie and Landshof is in agreement with the data for low values of Q^2, but can not describe the transition of photoproduction to deep inelastic scattering. In order to

improve the description of the data over the whole phase space, the model of Donnachie and Landshoff has been extended. The model of Abramowicz, Levin, Levy and Maor (ALLM97 [33]) makes the assumption that the intercept $\alpha_P(0)$ depends on Q^2. Using the data of deep inelastic scattering and of hadron and hadron scattering, the free parameters are fixed. This parametrization is used in this thesis.

In addition to the ALLM97 parametrisation based on Regge theory, there are other phenomelogical models which have been developed in order to describe the transition region $Q^2 \approx 1$ GeV^2 of the electron proton scattering. Some of such models involves dipole interactions [34], vector meson dominance models [35], and the fractal structure of the proton [105, 36].

In QCD the behaviour of the sea quark densities is described by gluon emissions and splitting. The higher the resolution power Q^2 is, the deeper the proton structure is probed and thus more gluon-gluon interactions can be "observed". Taking this interpretation in analogy to fractals, the proton could be treated of fractal nature only at low values of x, in the region where the sea quark densities dominates. Two magnification factors are used to simulate the fractal structure of the proton, which are defined in terms of Q^2 and x as $1 + Q^2/Q_0^2$ and $1/x$ [36]. Using this two magnification factors, the proton structure F_2 is predicted to be described by

$$F_2(x, Q^2) = \frac{e^{D_0 Q_0^2 x^{-D_2+1}}}{1 + D_3 - D_1 log(x)} \left[x^{-D_1 log(1+Q^2/Q_0^2)} \left(1 + \frac{Q^2}{Q_0^2}\right)^{D_3+1} - 1 \right] \tag{1.16}$$

where D_i and Q_0^2 are the five parameters that the fractal model needs to parametrize the behavior of F_2 as function of x and Q^2. The value of the parameters were determined using data from the HERA experiments H1 [21] and ZEUS [37] in the range $x < 0.01$ and $1.5 \leq Q^2 \leq 120$GeV^2, $0.045 \leq Q^2 \leq 0.65\,$GeV^2, respectively. In addition to ALLM97 this parametrization will be compared to the data in this analysis.

1.4 Motivation of this Analysis

This analysis is concentrated on the behaviour of the proton structure function F_2 in the transition region of non-perturbative to perturbative QCD. The data set which is analysed here are ep scattering data recorded by the H1 detector at the HERA collider. In order to measure the cross section at low values of Q^2, a special data sample is analysed where the interaction point was moved from its nominal position.

The measurement of the inclusive DIS cross section $ep \rightarrow e + X$ and the extraction of the proton

structure function F_2 at low values of Q^2 is dominated by systematic errors than by statistical uncertanties. The first analysis of the data sample which is investigated in this thesis was performed in [105] obtaining preliminary results [38]. This thesis together with the analysis developed in [100] performs an independent cross section measurement using the same data sample, but analysing in more detail the sources of systematic errors.

The inclusive cross section measurement can be obtained using *two independent* main detector components. Therefore two independent analysis are performed to determine the cross section measurement. In order to identify and quantify the systematic errors obtained from both analysis, detailed studies concerning the vertex reconstruction and the energy measurement of the particles building the final state are required. The investigations performed in [100] concentrates on the uncertainties due to the reconstruction of the interaction point of the ep collision. The cross section measurements of the *two analysis*, the one presented in this thesis and the one from [100] are also compared there.

This analysis includes detailed studies on the systematic errors resulting from the uncertainty of the energy measurement of the scattered electron and of the energy flow of the particles building the hadronic final state. Therefore, special emphasis is given to the influence of the noise identification algorithms on the reconstruction of the kinematical variables x and Q^2, which are essential for the measurement of the proton structure function F_2.

The thesis is organized as follows. In chapter 2 the H1 detector is introduced, special emphasis will be given to the subdetector components which are used to measure the inclusive cross section for low values of Q^2. In chapter 3 the data sample and the methods used to identify the scattered electron coming from the ep collision will be presented. The methods used to reconstruct the kinematical variables x and Q^2 are also subject of chapter 3. The techniques used to calibrate the main calorimeters of the H1 detector will be in detail discussed in chapter 4 and 5. In chapter 6 the cross section measurement and the extraction of the proton structure function F_2 is presented.

Chapter 2

The H1 Detector

The data sample of this analysis were collected in the year 2000 by the H1 detector at the HERA collider. In this chapter an overview of the HERA accelerator and the H1 detector is presented. Special emphasis is given to the H1 subdetector components used to measure the proton structure function for low values of Q^2.

2.1 HERA Storage Ring

The "Hadron-Elektron-Ring-Anlage" HERA at DESY is the first machine constructed to collide electrons or positrons with protons, where *both* electrons and protons are accelerated. In Fig. 2.1 a schematic layout of HERA and the pre-accelerator complex is shown.

HERA consists of two independent accelerators, with a circumference of 6,3 km. Electrons are injected with an initial energy of 12 GeV, while the protons are injected with an energy of 40 GeV into a ring of superconducting dipole magnets. In the year 2000, HERA delivered positrons [1] and protons with a final energy of 27.5 GeV and 920 GeV respectively.

In HERA proton and electron beams are composed of packets of particles called "bunches". The HERA rings can store maximally 220 bunches of particles. The electron bunches are short and the profile in beam direction is approximatly of Gaussian shape, the protons have a more complex structure with a central (main) bunch of high intensity, which is surrounded by additional bunches of much less intensity called "satellite bunches".

The electron and proton bunches cross the North and South interaction regions every 96 ns,

[1] during the following description the term "electron" is used to describe generically electrons or positrons

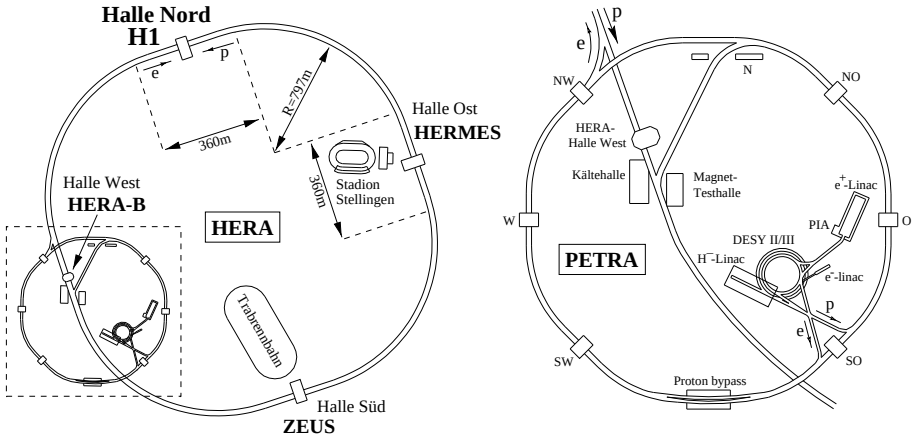

Figure 2.1: Schematic view of HERA (left) and the preaccelerator system (b)

where the H1 and Zeus detectors are installed. In order to directly determine the beam induced background in the interaction region, some electron and proton bunches are *not* filled. Therefore in addition to the *colliding bunches* there are a number of non colliding bunches (*empty bunches*) and also the so called *electron and proton pilot bunches*. Electron bunches not having a colliding proton bunch are known as *electron-pilot* bunches, in analogy proton bunches without a corresponding colliding electron bunch are known as *proton pilot* bunches. Thus, from the 220 bunches that HERA can fill, in average only 174 collide, 24 are empty bunches and 7, 15 correspond to proton and electron pilot bunches, respectively [100].

2.2 The H1 Detector

The H1 detector is a multipurpose detector, designed to study inclusive and exclusive final states of ep interactions.

In Fig. 2.2 a three dimensional view of the H1 detector is shown, where the sub-detector components are marked with numbers. The H1 detector is situated concentrically around the beam axis 1. The interaction point (marked in red) defines the origin of the H1 coordinate system. The direction of the incoming proton defines the positive z direction of the coordinate system. Since the centre of mass energy of the ep collisions is boosted along the proton direction, the H1 detector is more massive and finer segmented in that direction.

The interaction point is surrounded by the central and backward silicon trackers (not visible in Fig. 2.2). The central and forward trackers 2,3 enclose the silicon detectors and the beam pipe. They are used to identifies charged particles and to measures their momenta. The liquid

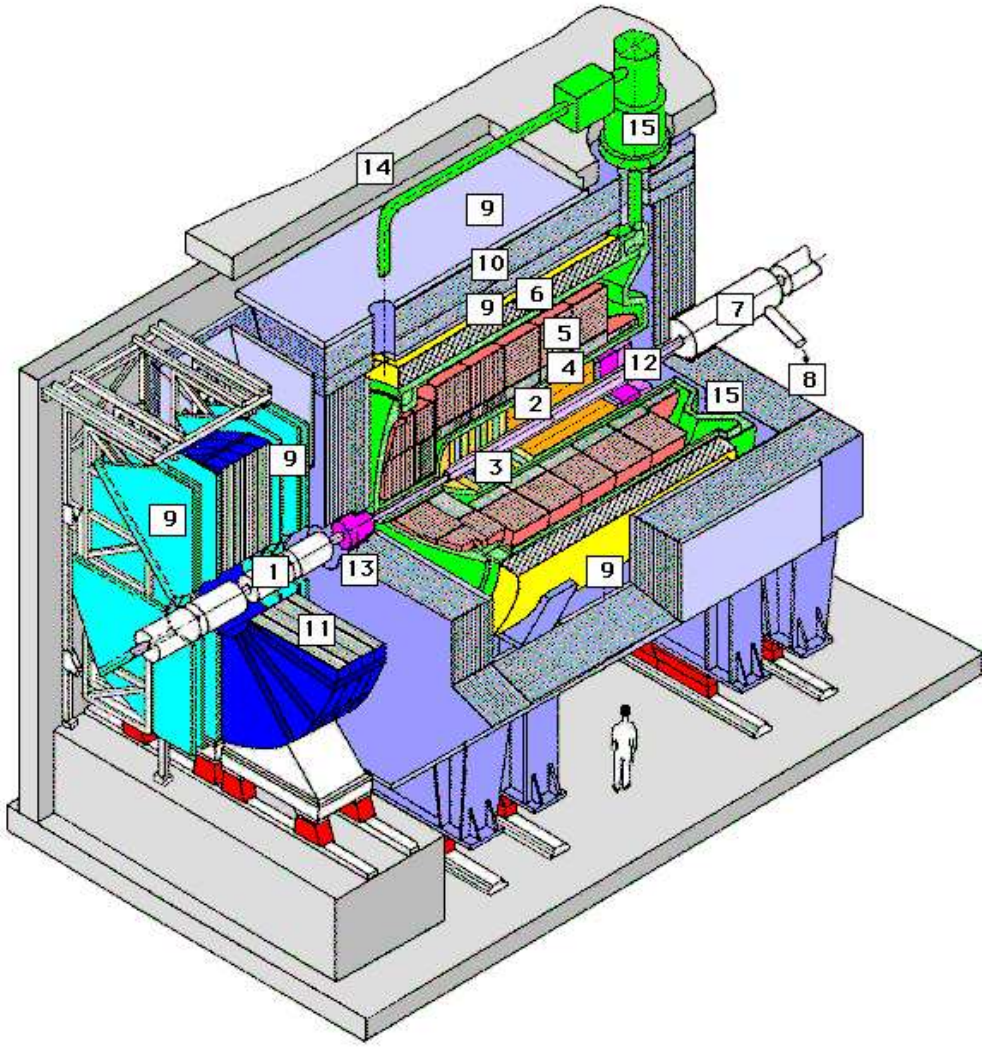

Figure 2.2: Three dimensional view of the H1 detector, the numbers denote:

1	Beam pipe and beam magnets	9	Muon Chambers
2	Central tracking chambers	10	Instrumented iron yoke
3	Forward tracking chambers	11	Forward muon toroid
4	Electromagnetic LAr calorimeter	12	Backward calorimeter Spacal
5	Hadronic LAr calorimeter		and backward drift chamber
6	Superconducting coil (1.16T)	13	Forward plug calorimeter
7	Compensating magnet	14	Concrete shielding
8	Helium supply for 7	15	Liquid Argon cryostat

argon calorimeter (LAr) surrounds the tracking devices [4,5] and is used to measure the energy and momenta of high energetic particles. The superconducting coil [6] surrounds both the tracking devices and the LAr calorimeter, producing a constant magnetic field of 1.16 T parallel to the beam axis. The compensating magnet [7] provides a longitudinal field equal in size and opposite in direction to that of the superconducting coil. The magnetic field configuration of H1 is designed to not disturb the circulating beams of HERA.

Muons are detected in a streamer tube system placed inside the iron of the return yoke [10]. The muons are recognised since they can penetrate large quantities of material almost without deflection, meanwhile other particles are absorbed. In order to recognise muons produced in the forward direction, the forward muon spectrometer [11] is used.

Particles scattered into the backward direction deposit their energy in the SpaCal calorimeter [12]. In front of the SpaCal, the backward drift chamber BDC is located. Using the SpaCal calorimeter and the BDC chamber, it is possible to identify the scattered electron coming from DIS events for values of $2 < Q^2 < 100\,\mathrm{GeV}^2$. In Fig. 2.3 a schematic $r - z$ view of the backwards detectors is shown. The essential subdetector components used in the low Q^2 analysis are:

- the **SpaCal** calorimeter since it provides trigger information, identify the scattered electron and measure their energy.
- the **Central Trackers** devices (CTD) which measure the position of the interaction point (vertex) and the momenta of particles belonging to the final state.
- the **Backward Drift Chamber** (BDC) provide information of the exact position of the scattered electron in the radial direction and measure the angle of the scattered electron, together with the CT devices.
- the **Backward Silicon Trackers** (BST) measures precisely the vertex position and the angle of the scattered electron.
- the **Liquid Argon** calorimeter measures the momenta of particles coming from the hadronical final state.
- the **Luminosity system** measures the luminosity.

In the following sections, these subdetectors components will be explained in detail.

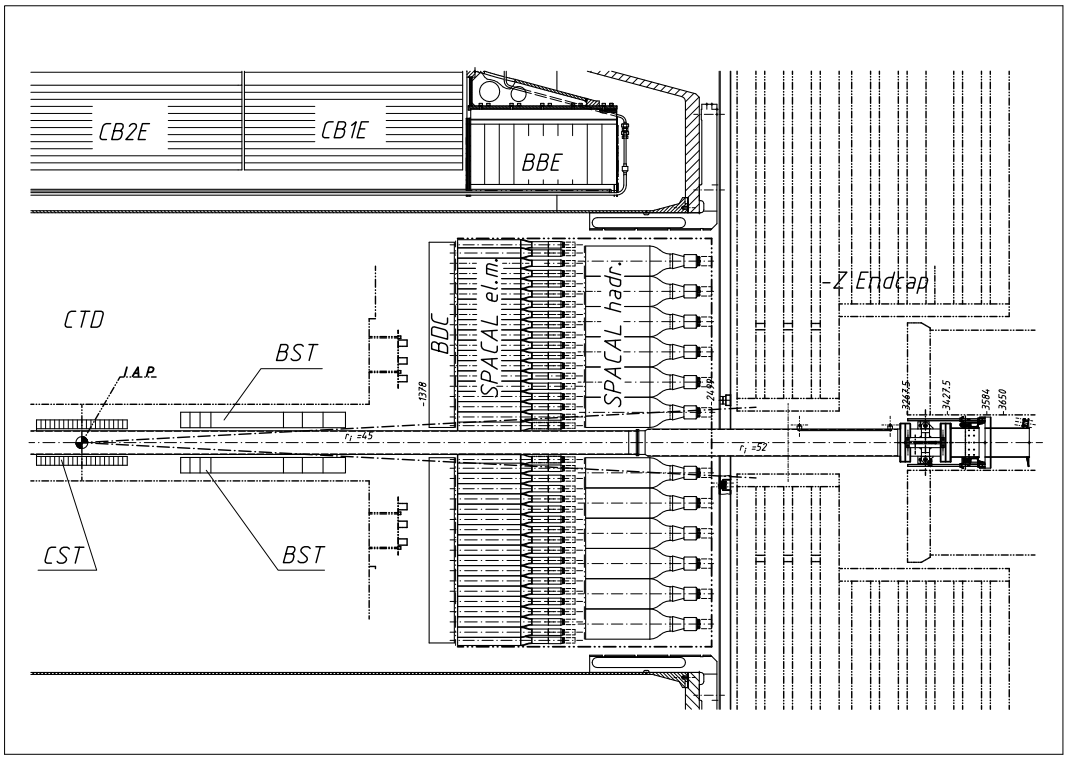

Figure 2.3: $z - r$ view of the backward devices of the H1 detector. The interaction point (IAP) is surrounded by the central silicon tracker (CST). In front of the Backward silicon tracker (BST) are localised the Backward Drift Chamber (BDC) and the SpaCal calorimeter. Some modules of the electromagnetic section of the LAr calorimeter labelled as BBE, CB1E, CB2E are also shown.

2.2.1 SpaCal Calorimeter

The SpaCal is a sampling calorimeter which uses lead as convertor material and scintillating-fibre as active material [45]. The SpaCal is localised at $z = -160\,\text{cm}$ and has a diameter of 160 cm, having an angular acceptance of $168^\circ < \theta_e < 177.8^\circ$ for electrons scattered from the nominal vertex position. The SpaCal calorimeter is divided into two sections, one electromagnetic and one hadronic. In Fig. 2.3 an $r - z$ view of the electromagnetic section of the SpaCal calorimeter is shown.

The electromagnetic part of the SpaCal calorimeter consists of 1192 cells, each cell has an active cross section area of $40.5 \times 40.5\,\text{mm}^2$ and a depth of 250 mm. The SpaCal cells are made of grooved lead plates and scintillating fibres with a lead-fibre ratio of 2.27 : 1. The electromagnetic SpaCal corresponds to 27.47 radiation lengths (X_0) and one hadronic interaction length. A drawing of the SpaCal calorimeter in the $r - \phi$ view is shown in Fig. 2.4(a).

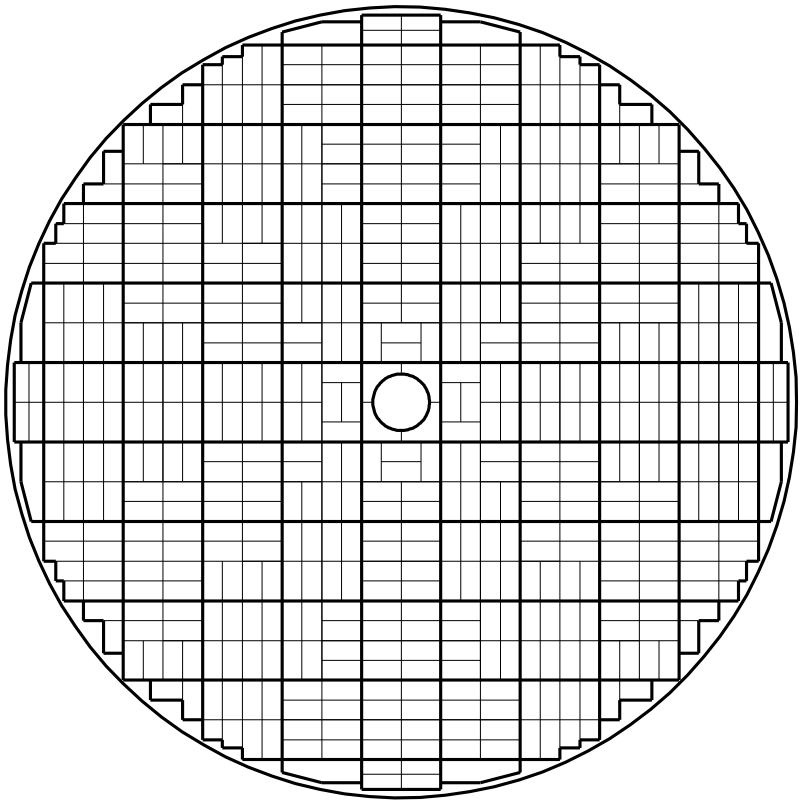

(a) $r - \phi$ view of the electromagnetic section of the SpaCal calorimeter. The border of the 16-cell modules are drawn with bold lines.

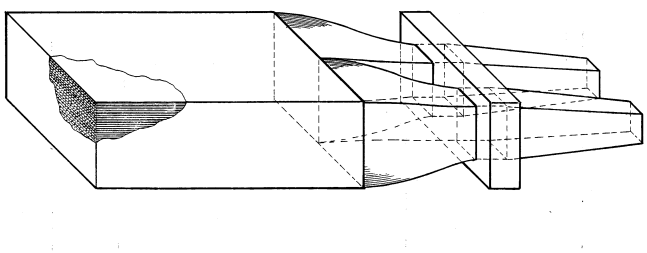

(b) The 2-cell module configuration showing lead fibre matrix, fibre bundles and the light mixers.

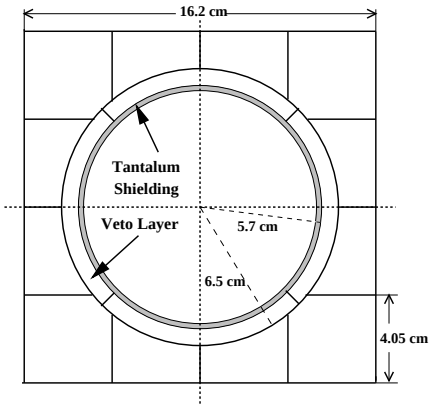

(c) $r - \phi$ drawing of the insert module

Figure 2.4: The geometry of the SpaCal calorimeter and its basic components [45].

The smallest construction unit of the detector are 2-cell modules. They consist of a stack of 52 lead plates each containing 90 fibres (see Fig. 2.4(b)). The fibres ends are arranged into two fibre bundles of 70 mm length. The scintillation light of each cell is converted to a electric pulse using photomultipliers tubes, which operates in the magnetic field of 1.16 T and reach an amplification gain of $\approx 10^4$ [47].

Groups of 2-cell modules are combined to form a 16−cell module, which represent the main building block of the electromagnetic section (see Fig. 2.4(a)). The innermost module is called the insert module and has the same size as the other 16−cell modules (see Fig. 2.4(c)). The cells of the insert module are not of rectangular shape due to the space needed for the beam pipe. The cells closest to the beam pipe are of ring shape and are called "veto cells" (see Fig 2.4(c)). A 2 mm thick tantalum layer protects the detector against synchrotron radiation.

Due to the small diameter of the fibres, an relative energy resolution of $7\%/\sqrt{E[GeV]} \oplus 1\%$ is achieved. The designed energy resolution of the SpaCal calorimeter is 2% for electron energies of 30 GeV, and the angular resolution achieved is 2 mrad. The time resolution of the SpaCal calorimeter is 1 ns and is used to reject beam related background (beam-gas and beam-wall) events. The time of the SpaCal is used for trigger purposes.

The hadronic section of the SpaCal calorimeter has a structure similar to the electromagnetic section. The diameter of the scintillation fibres is 1 mm being two times bigger than the electromagnetic ones. The lead-to-fibre ratio for the hadronic part of the SpaCal calorimeter is 3.4 : 1. The calorimeter consists of 136 modules surrounding the beam pipe, each module has a cross section area of $119.3 \times 119.0\,\mathrm{mm}^2$ and a depth of 250 mm, corresponding to one nuclear interaction length.

2.2.2 Backward Drift Chamber

The scattering angle measurement of the SpaCal can be improved using the Backward Drift Chamber (BDC) [52]. The BDC is placed in front of the SpaCal calorimeter (see Fig. 2.3). The chamber is built of four double layers, which are divided into eight octants. Each octant comprises 32 drift cells with sense wires. The radial wire spacing is 1 cm for the inner 16 cells and 3 cm for the outer cells. Each double layer is consequently revolved by 11.25° to enable the azimuthal ϕ angle measurement. A schematic view of the chamber is shown in Fig. 2.5.

In order to optimise the polar angle measurement, the wires of the BDC are oriented in the azimuthal direction like a spiderweb. In that way the drift in the cells takes place in the radial direction. The BDC has the same angular acceptance as the SpaCal and provides a polar angle measurement with a resolution of 0.5 mrad.

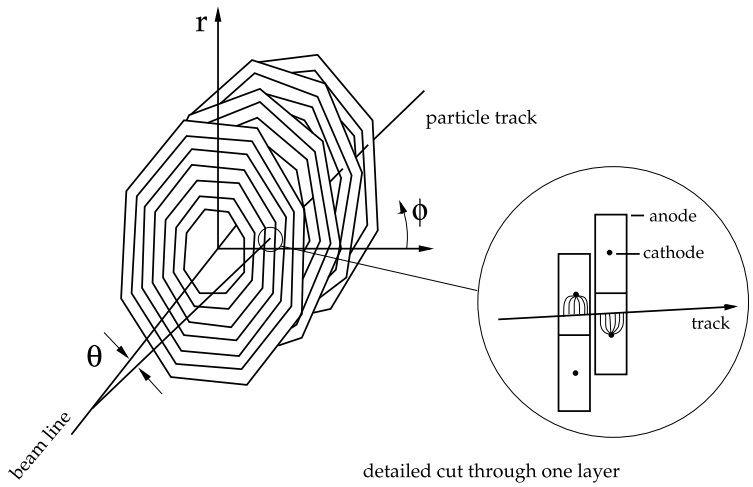

Figure 2.5: Schematic drawing of the Backward Drift Chamber [52].

2.2.3 Tracking Devices

The track reconstruction in the central region of the H1 detector is based on two large concentric drift chambers CJC1 and CJC2 (detector 2 in Fig. 2.2), having wires strung parallel to the beam axis. The drift cells are inclined with respect the radial direction. From the signals recorded in those chambers the transverse track momentum is determined and in addition the specific energy loss dE/dx is used to perform particle identification. A transversal view of the tracking devices of the H1 detector is shown in Fig. 2.6 The chambers allow the measurement of the z position comparing the signals in the read out from both wire ends.

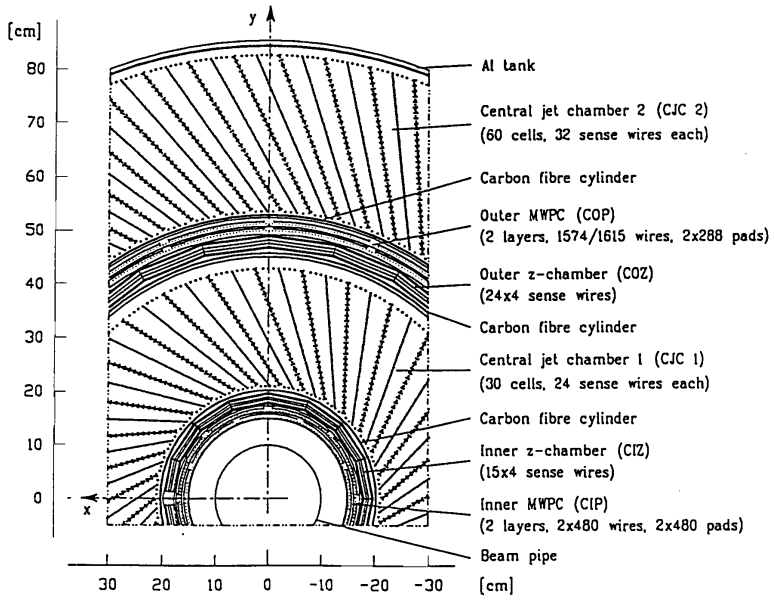

Figure 2.6: Radial view of the tracking detectors [40]

The central inner $z-$chamber (CIZ) and the central outer $z-$chambers (COZ) measure the z

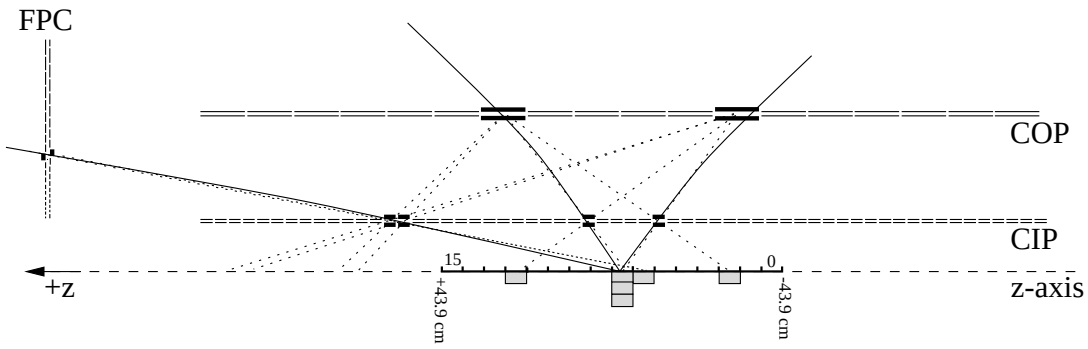

Figure 2.7: The trigger of the z position of the interaction vertex [53].

coordinate with better accuracy than CJC1 and CJC2. They deliver track elements with a resolution in z of $300\mu m$, which is combined with the measurement of the CJC. The CIZ is placed inside CJC1, while the COZ is located between CJC1 and CJC2. The polar angles covered by CIZ and COZ are $16^\circ < \theta < 25^\circ$ and $25^\circ < \theta < 156^\circ$ respectively.

In the central and forward regions, combinations of pad hits in the central inner proportional chamber (CIP), central outer proportional chamber (COP) and the forward proportional chambers (FWPC) are used to trigger on tracks coming from a nominal interaction vertex. The principal task of the trigger of the proportional chambers is the determination of the vertex in the z axis. Fig. 2.7 illustrates the concept to determine the vertex. For each ep collision, the hits in the chambers are connected by a straight line which is extrapolated to the beam axis. The interception of the line tracks with the beam axis make an entry in a z-histogram. One expects that the maximum of the histogram corresponds to the position of the vertex. The vertex histogram is constructed with 16 bins in an interval in z from $-43.9\,\text{cm}$ to $43.9\,\text{cm}$ [40].

2.2.4 BST

The Backward Silicon Tracker (BST), is one of the two silicon detectors placed close to the beam pipe. The BST serves for the precise measurement and identification of the scattered electron in the backward region. A schematic view of the detector is shown in Fig 2.8.

The detector consists of two subdetector parts BST1 and BST2, each one is arranged perpendicularly to the beam axis between $z = -35.8\,\text{cm}$ and $-95.7\,\text{cm}$. Both BST1 and BST2 are composed of two symmetric shells, each containing 8 planes of active sensors called *wafers* (see Fig. 2.8(a)).

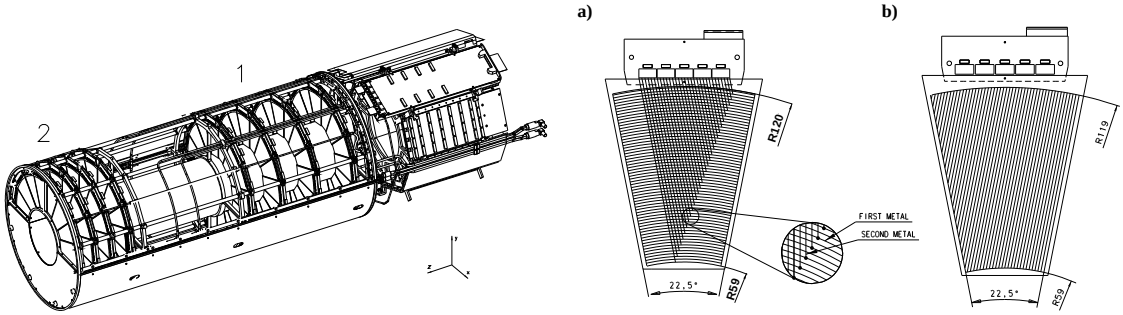

(a) Three dimensional view of the backward silicon tracker. The label 1 and 2 represent the detectors BST1 and BST2.

(b) The structure of the silicon sensors (a)r and (b)u.

Figure 2.8: The Backward Silicon Tracker in its configuration in the year 2000 [90].

Each plane of the BST is made of 16 so called r sensors and 1 u sensors. The u sensor is a single metal sided silicon, which is located on each plane at $45^\circ < \phi < 67.5^\circ$. Combining the information from the r and u sensors it is possible to measure the momentum and the charge of a track with the BST.

The active sensors or the wafers are made of 250 μm thick n-type silicon. A single minimizing ionization particle creates about 22000 electron-hole pairs, which is sufficient to produce a signal. Each wafer provides 640 readout channels, the signals are collected with an integrated front-end system [90].

The BST provides a polar angle measurement independent of the central tracking devices, covering the interval $164^\circ < \theta < 176^\circ$ with an accuracy of about 0.2 mrad. Through the extrapolation of the reconstructed track to the beam line a measurement of the z-vertex position is also possible.

2.2.5 Liquid Argon Calorimeter

The Liquid Argon calorimeter (LAr) is the biggest calorimeter of the H1 detector (see 4 and 5 in Fig. 2.2). It is divided in an electromagnetic and an hadronic section. The LAr is a sampling calorimeter which uses liquid argon as active material, and lead as absorber material in the electromagnetic section and steel in the hadronic section. In order to keep the liquid argon fluid, the calorimeter is placed in a cryostat. Cooling down to liquid argon temperature is achieved by circulating helium gas cooled in an external and movable liquid nitrogen heat exchanger. Fig. 2.9 shows the LAr calorimeter in the $r - z$ view.

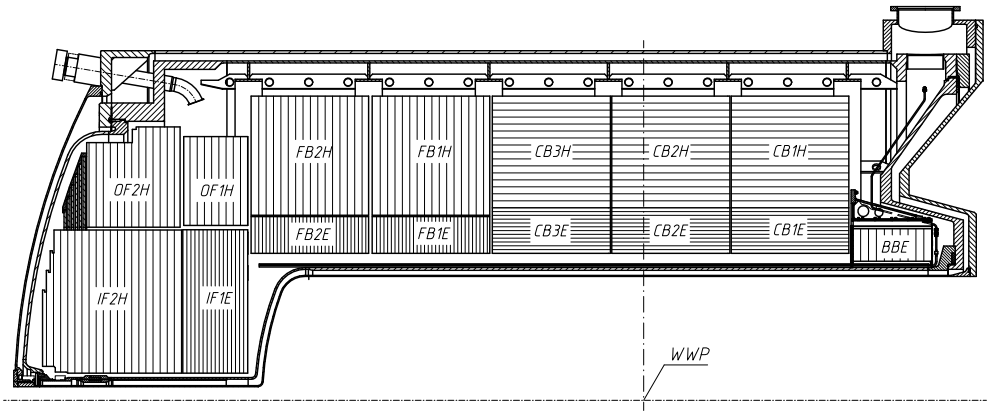

Figure 2.9: $r-z$ view of the LAr calorimeter. The modules are labelled according to its position with respect the interaction point (WWP) either central (CB) backward (B) or forward (IF,OF). The modules corresponding to the electromagnetic and hadronic section are in addition labelled with a E or a H [40, 41].

The calorimeter is build of absorber plates supplemented by high voltage and read out electrodes. The interspaces between the plates are filled with liquid argon. To obtain a uniform energy resolution, the orientation of the plates is arranged such that the angle of incidence of particles coming from the interaction point is always larger than 45°. The absorption length of the electromagnetic part varies between 20 and 30 radiation lengths X_0.

The LAr calorimeter is divided along the $z-$ direction into eight self supporting wheels named according to its position with respect to the proton beam, Backward Barrel (BB), Central Barrel (CB), Forward Barrel (FB1,FB2) and Outer Forward (OF) and Inner Forward (IF). The BBE consists only of an electromagnetic section and the OF of two hadronic sections. In ϕ direction each wheel is further segmented into eight identical units, the so called octants.

The energy resolution of the electromagnetic part of the calorimeter is $\sigma_E/E \approx 11\%/\sqrt{E/GeV} \oplus 1\%$ while the hadronic part has a resolution energy of $\sigma_E/E \approx 50\%/\sqrt{E/GeV} \oplus 2\%$. The LAr calorimeter covers the tracking system and has an angular acceptance of $5^\circ < \theta < 154^\circ$.

2.2.6 The Luminosity system

The luminosity in the H1 experiment is derived from the rate of the Bethe-Heitler events $ep \rightarrow ep\gamma$. In such a process the electron and the proton interact elastically and in addition a photon is emitted.

The luminosity system consist of two arms, the electron tagger (ET) and the photon detector

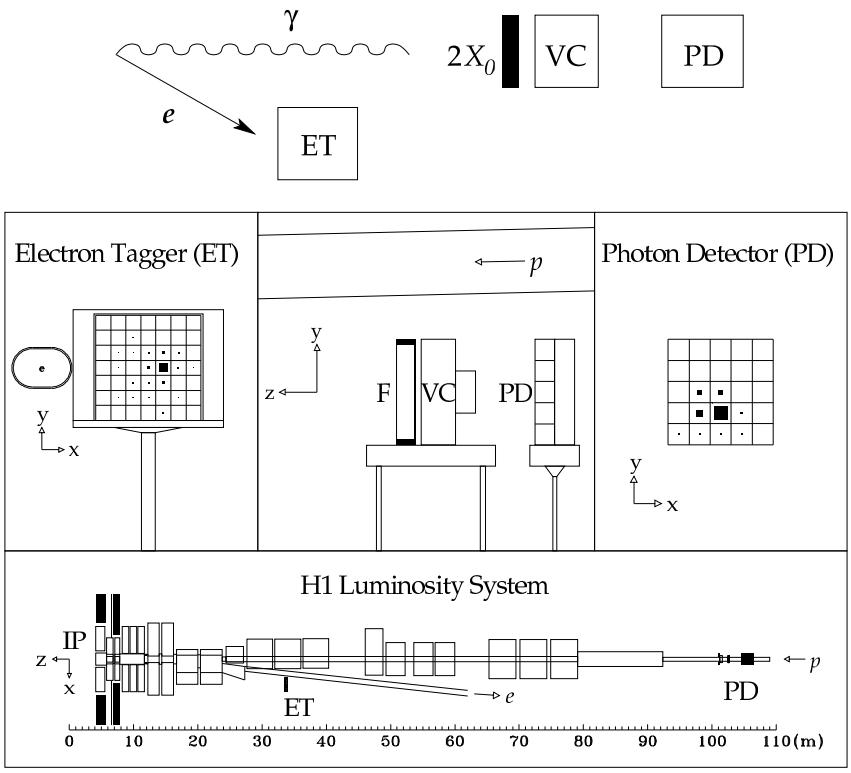

Figure 2.10: Luminosity system [39, 58].

(PD). Since the angular separation between the electron and the photon are of the order or 16μrad, the detectors are placed far away from the H1 interaction point. A schematic view of the luminosity system is shown in Fig. 2.10.

The on-line luminosity is obtained measuring the rate of Bethe-Heitler events detected in coincidence. The scattered electron is deflected by quadrupoles and a bending magnet, being detected with the ET located at $z = -33.4\,\text{m}$. The bremsstrahlung photon is detected in the PD located at $-z = 102.9\,\text{m}$. In order to protect the PD from the high synchrotron flux, a filter of Pb with $2X_0$ followed by a $1X_0$ water Cerenkov counter is located in front of the PD. The main source of background are bremsstrahlung events originating from collisions between the beam electron and the residual gas (e^+gas) in the beam pipe leading to the same event signature. The contribution of such events is estimated using the electron pilot bunches.

A more precise luminosity calculation is performed "off-line" using the energy spectrum of the bremstrahlung photons coming from the Bethe-Heitler process. To minimise the systematic errors, it is important to understand in detail the energy spectrum of the photon and the influence of the acceptance of the PD. In addition the e^+gas background is taken into account and the ef-

fect that more than one photon at the same buch crossing (photon pile-up effect) is produced and detected in the PD [99]. The luminosity calculation needs to consider also contribution coming from the satellite bunches [60]. The resulting uncertainty of the measured luminosity is within 2.2% [61].

2.2.7 The Trigger system

The principal task of the trigger system is to separate real physic events from background events. The trigger system in H1 in the year 2000 selected events in three levels, in the following denoted as L1,L2 and L4, respectively.

During the latency time of the first trigger level L1, all subdetector components store their data in pipelines [62]. The pipeline is designed such that the decision if the event is accepted (or not) has to be taken within 2.3 μs. In order to take this decision selected subdetector components deliver their trigger information to the central trigger. The central trigger receives up to 256 trigger elements (TE), which through logical combinations define the 128 subtrigger elements (SE). If one of those SE accepts the event, the so called L1-keep signal is generated the pipeline system is stopped, causing from that moment and dead time of the detector.

The second trigger level (L2) calculates its decision within 20μs. The decision of L2 is based on two systems, the topological trigger (L2TT) and the neuronal trigger (L2NN). Both use the information of several subdetector components. In case the event is accepted by L2, the full detector data for the triggered event are readout and sent to L4. After that, the pipelines are enabled again.

The level 4 system (L4) consist of a group of 30 farm computers working in parallel. These computers run a optimised version of the H1 reconstruction program. Based on the result of the reconstruction the decision of the early trigger levels is verified. In addition each event gets assigned to various classes of physics. The event will be rejected if does not match the selection of any class.

The capacity of the L4 input has a fixed bandwidth of 50 Hz and has to be distributed over all active SE. Since the rates of the SE might be different, the bandwidth of L4 is not equally distributed over all SE.

In addition to the trigger conditions, also the beam conditions can influence the rate of the various SEs. It is possible that several subtriggers accept so often events that the rate of the SEs exceeds the input rate of L4. Therefore it is necessary to introduce prescale factors. If one subtrigger element j (SE-j) has a prescale-factor k, then it will cause an L1-keep only every

k-time. On analysis level the events triggered by the subtriger SE-j have to have a weight corresponding to the prescale factor *k* [64, 63].

The prescale factors are calculated with a prescale program. It is an automatic tool which analyses the rate of the different subtriggers and performs a prediction on the future behaviour of the rate of the triggers. Using a complicated strategy the distribution of the bandwidth can be optimised.

2.3 Run selection

The time during which the electron and proton beams collide is known as luminosity fill and its duration is limited due to the lifetime of the electron beam. This luminosity fills are divided into "runs", having an average duration of $1-2$ hours, depending on the beam and background conditions. Thus, on analysis level is important to perform a selection of the usable runs.

The selection of the runs is based in the following criteria:

- *Run quality.* Each run is clasified as "good" "medium" or "poor" depending on the status of the subdetectors components. A run can be poor if one of the main components is not available over the whole time. Here will be used only runs which were clasified as "good" and "medium".
- *Readout status.* For each run there is information available over the status of the readout of the subdetector components. Since an inclusive DIS cross section measurement requires the identification of the electron and the hadronical final state, only runs where SpaCal, BDC, BST, CIP, COP, CIZ, CJC and LAr in the readout are considered.
- *Trigger phase and prescale.* At the beginning of the luminosity fill, the trigger phase 2 is declared if the current of the electron and proton beams is high and the background conditions allows turn on the central tracker devices. Since the statistic error of the measurement is calculated through the quadrat of the prescales $\sigma^2 = \sum_i w_i$, only runs with prescale less than 3 will be considered. The trigger used in this analysis is based on energy depositions on the SpaCal calorimeter of particles coming from the interaction point. In section 6.2 a dissusion of the trigger efficiency will be presented.

Chapter 3

Data and Monte Carlo sample

In August of 2000 a special run period was performed by H1 to measure low values of Q^2 below the nominal value of $2\,\mathrm{GeV}^2$. The *ep* interaction point was shifted by 70 cm in the proton direction, reaching higher acceptance in the backward region of the H1 detector. This special "shifted vertex run" took data over 3 days, recording an integrated luminosity of about $600\,\mathrm{nb}^{-1}$. This amount of luminosity represents two times more statistic than the previous shifted vertex run taken in the year 1995.

In this chapter will be described the reconstruction methods used to analyze the shifted vertex data, afterwards the cuts used to identify the scattered electron are introduced and its efficiency is studied. At the end of the chapter will be described the background of DIS events for low values of Q^2.

3.1 The Shifted vertex run

In DIS events for values of $Q^2 \leq 100\,\mathrm{GeV}^2$, the electron is scattered into the backward region of the H1 detector. There are two possibilities to measure the angle of the scattered electron at low values of Q^2: One possibility uses the track measured by the backward silicon tracker (BST), while the other possibility reconstructs the angle with the backward drift chamber (BDC) and the central tracking devices (see section 2.2.4 and 2.2.2).

Usually, when the collision between the electron and the proton beams takes place in the nominal position, the maximum value of the angle of the scattered electron that can be measured by the BST and the BDC is 176.5° and 176.8° respectively. During the shifted vertex run period, the interaction point was moved in the proton direction by 70 cm, increasing the acceptance of

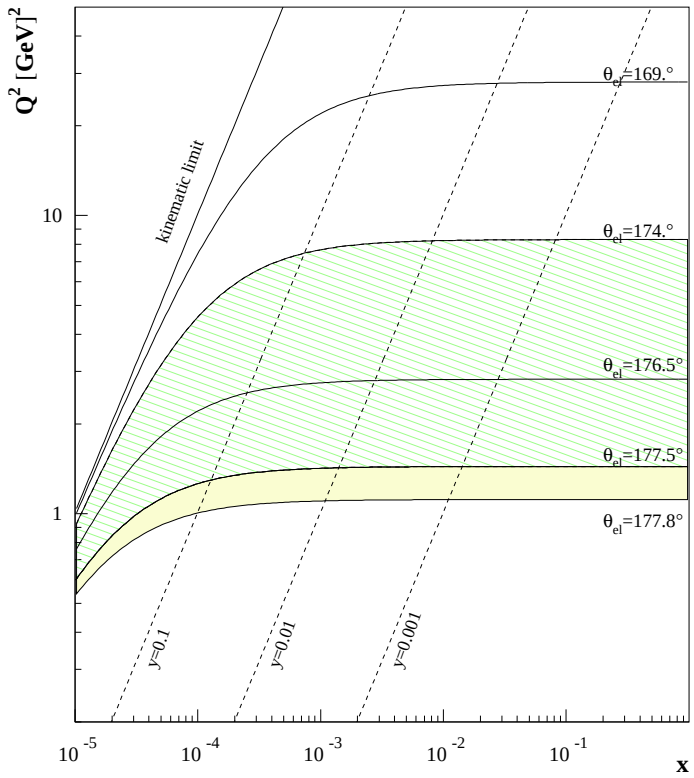

Figure 3.1: Acceptance of the BST during the shifted vertex data period $174^\circ \leq \theta_e \leq 177.5^\circ$ (hatched area) compared to the acceptance of the BST if the vertex is localised at the nominal position $z = 0.\,\text{cm}$ ($169^\circ \leq \theta_e \leq 176.5^\circ$). The additional maximal angular acceptance of the BDC is also shown (solid area $177.5^\circ \leq \theta_e \leq 177.8^\circ$).

the backwards devices as the BST and the BDC.

In Fig. 3.1 the $Q^2 - x$ plane is shown, with lines of constant scattering angles. The solid lines $\theta_e = 176.5^\circ$ and $\theta_e = 169^\circ$, are the maximum and minimum angle of the scattered electron that can be measured by the BST at the nominal vertex position ($z = 0\,\text{cm}$). The hatched area in Fig. 3.1 represents the angular acceptance of the BST in case the vertex is shifted by $z = 70\,\text{cm}$. The solid area in Fig. 3.1 illustrates the additional maximal angular acceptance that the BDC and the CTD have in case the vertex is shifted 70 cm from the nominal position.

From Fig. 3.1 follows that during the shifted vertex period the acceptance of the BST and the BDC shifts towards lower values of Q^2, opening the possibility to measure lower values of x for low values of Q^2.

In order to measure the inclusive cross section of the DIS process $ep \rightarrow eX$ for these low values of x and Q^2, the identification of the scattered electron with the backward devices is a task

of prime importance. In order to profit from the two detector components used to identify the scattered electron and to derive the systematic errors of the measurement, two analysis in parallel were performed. In the analysis developed in [100] the BDC is used as the main detector to reconstruct together with the CTD and the SpaCal the angle of the scattered electron. The analysis presented in this thesis uses the BST and the SpaCal calorimeter to identify the scattered electron.

Several effects like background contributions and detector resolution, have to be studied in order to correctly identify the scattered electron, for example:

- The scattered electron can escape the detection of the backward devices and a charged particle coming from the hadronical final state can be misidentified as the scattered electron. This background events are known as photoproduction events and have a contribution of 5% for $y \geq 0.5$ (see section 3.6). In order to reduce the photoproduction background, not only the electron identification is important but also the hadronical final state had to be studied in detail.
- The reconstruction of the kinematical variables x and Q^2 can be performed using exclusively the energy and momenta measurements of the scattered electron. Although this reconstruction method is the most precise for low values of $x \approx 10^{-4}$, it begins to be less accurate for values of $x \approx 10^{-3}$. Other possibilities used to reconstruct the kinematical variables for high values of x consider also the energy and momenta measurement of the hadronical final state.

In section 3.3 the methods used to reconstruct the kinematical variables x and Q^2 are introduced, there the resolution of the kinematical variables are studied using a Monte Carlo simulation (MC) with the characteristics of the shifted vertex data. This step is necessary since the measured distributions like energies and positions are a convolution of pure physics characteristic with intrinsic detector resolutions, therefore the Monte Carlo simulation is used to reproduce the behavior of the data and to separate as good as possible the pure physic effects from the detector resolutions. The MC used in this analysis is discussed in section 3.2.

In section 3.4 the electron identification using the SpaCal calorimeter and the BST is presented, afterwards in section 3.5 the efficiency of the cuts used to identify the scattered electron are discussed. At the end in section 3.6, the main source of background to DIS events is explained and its contribution during the shifted vertex data is determined.

3.2 Monte Carlo Sample

The Monte Carlo (MC) samples are produced in two steps, first a generator is used and then the detector simulation and the reconstruction of the event is performed.

The generator has the task to produce pure physic events according to theory or models, in such way four vectors and cross sections are obtained. The simulation uses this information to produce the detector response. In this analysis the generator programs DJANGOH1.4 [68] and PHOJET [74] were used to produce the signal and background of DIS events. Next, the package H1SIMREC [65, 66] was used to simulate and produce the detector response. In the following paragraphs the general characteristic of the MC generators and the simulation step are described.

- The DJANGOH1.4 program is based on several packages. HERACLES[69] generates the event at parton level and allows the integration of the differential cross section for $ep \rightarrow e'X$ over kinematical regions which can be defined in terms of x, y, Q^2. HERACLES can perform a separate treatment of the Born term of the cross section and several parts of the QED corrections. For NC processes, the QED corrections include leptonic initial state radiation (ISR), leptonic final state radiation (FSR), a contribution called Compton part and quarkonic radiation. Within HERACLES is possible to choose among a set of parametrizations for input parton distributions. In this analysis are used the parton distribution parametrization from the MRST group [104]. HERACLES can also simulate electroweak processes to first order in α_s and one loop corrections.

  In order to have a complete event simulation not only at parton level, DJANGOH call routines from LEPTO[70] and JETSET [75], in such way the complete event simulation including fragmentation and hadronization of the scattered quark and the proton remmmant are obtained.

  The program LEPTO is used to calculate the QCD matrix elements and generate the hadronic final state on the parton level. Parton cascades are generated by ARIADNE[71] using the Color Dipole Model. While, the fragmentation step is computed using the Lund-String model as implemented in JETSET. In order to simulate the hadronic final state at low W, the SOPHIA[73] package is used. In this analysis a cut on $W = 5\,\text{GeV}$ is performed to define the boundary where SOPHIA and LEPTO+ARIADNE had to be used.

  Diffractive events are simulated with ARIADNE using the Soft Color Interaction (SCI) model. This implementation does not take into account the pomeron quantum numbers. It produces a reasonable description of the inclusive energy flow in DIS events, but it creates huge backgrounds to exclusive process like DVCS[101] and QEDC[102]. A study

of the DJANGOH1.4 excluding the SCI will be discussed in section 5.5

- PHOJET[74] simulates the total photoproduction cross section, incorporating soft and hard hadronic processes. The hadronization is performed by JETSET. Photo-production is the main physical background for DIS events at low Q^2. The amount of photoproduction events in the DIS sample, is studied using part of the luminosity system and will be discussed in section 3.6 in detail.

- H1SIMREC[65, 66]: The generated events are fed into the detector simulation H1SIM based on GEANT[67]. H1SIM simulates the H1 detector response, taking into account the geometry and acceptance of its subdetectors as well as dead material distributed within H1. H1DIGI runs after H1SIM and perform a "digitalisation" of the simulated hits. In this step efficiencies and noise corrections and calibration constants obtained from data and test beam studies are applied. H1REC reconstruct finally the whole event as it is done for real data.

The MC samples used in this analysis have in total 20 millions of events for both DJANGOH and PHOJET.

In the following section, the MC simulation is used to study the resolution of the reconstructed variables x and Q^2. The original generated variables denoted by the subindex *gen* are directly compared with the reconstructed variables having a subindex e, Σ. Since the resolution of the kinematical variables is influenced by several effects, the final deviation of the reconstructed variables from the generated ones is studied using the DIS selection cuts introduced in chapter 6.

3.3 Reconstruction Methods

As we have seen in chapter 2, the H1 detector can measure the energy and the angle of the scattered electron and the energy depositions and momenta of the particles building the hadronic final state. The event kinematic is over-constrained and several reconstruction methods can be defined using the total final state or part of it. In the following sections the relevant reconstruction methods employed are briefly described.

3.3.1 Electron Method

The electron method uses *purely* the measurement of the four vectors of the incoming and scattered electron. The event kinematic is given by:

$$Q_e^2 = E_e^2 \frac{\sin^2 \theta_e}{1 - y_e} \qquad y_e = 1 - \frac{E_e}{E_{inc}^0} \sin^2 \frac{\theta_e}{2} \qquad x_e = \frac{Q_e^2}{s y_e} \tag{3.1}$$

where $E_{inc}^0 = 27.5\,\text{GeV}$ is the energy of the incoming electron. The variables E_e and θ_e are the energy and polar angle of the scattered electron.

The resolution of the event kinematic depends on the accuracy of the energy measurement of the scattered electron E_e and its polar angle θ_e, the resolution is given by:

$$\frac{\delta Q_e^2}{Q_e^2} = \frac{\delta E_e}{E_e} \oplus \tan\left(\frac{\theta_e}{2}\right) \delta\theta_e \tag{3.2}$$

$$\frac{\delta y_e}{y_e} = \frac{1 - y_e}{y_e} \left(\frac{\delta E_e}{E_e} \oplus \frac{\delta \theta_e}{\tan \theta_e / 2} \right) \tag{3.3}$$

From Eq. 3.3 it is clear that the electron method is very precise for high values of y, due to the factor $(1 - y)/y$, and begins to be less precise for low values of y.

Fig. 3.2 show the relative deviation of x_e and Q_e^2 from the generated variables x_{gen} and Q_{gen}^2 for the whole DIS selection.

Each point in Fig. 3.2(a) and (b) correspond to the mean position and spread of a Gaussian fit restricted to the interval:

$$-0.3 \leq \frac{x_e - x_{gen}}{x_{gen}} \leq 0.3 \qquad -0.5 \leq \frac{Q_e^2 - Q_{gen}^2}{Q_{gen}^2} \leq 0.5 \tag{3.4}$$

In such way the Gaussian fit converges giving the correct peak position of the scattered distribution also shown in Fig. 3.2.

Form Fig. 3.2(a) follows that the electron method is very precise for low values of $x \leq 10^{-4}$ (high y) and begins to be less accurate for higher values of $x_{gen} \approx 10^{-3}$. For such values x is reconstructed to lower values as it was generated. The resolution of x degrades from 5% at

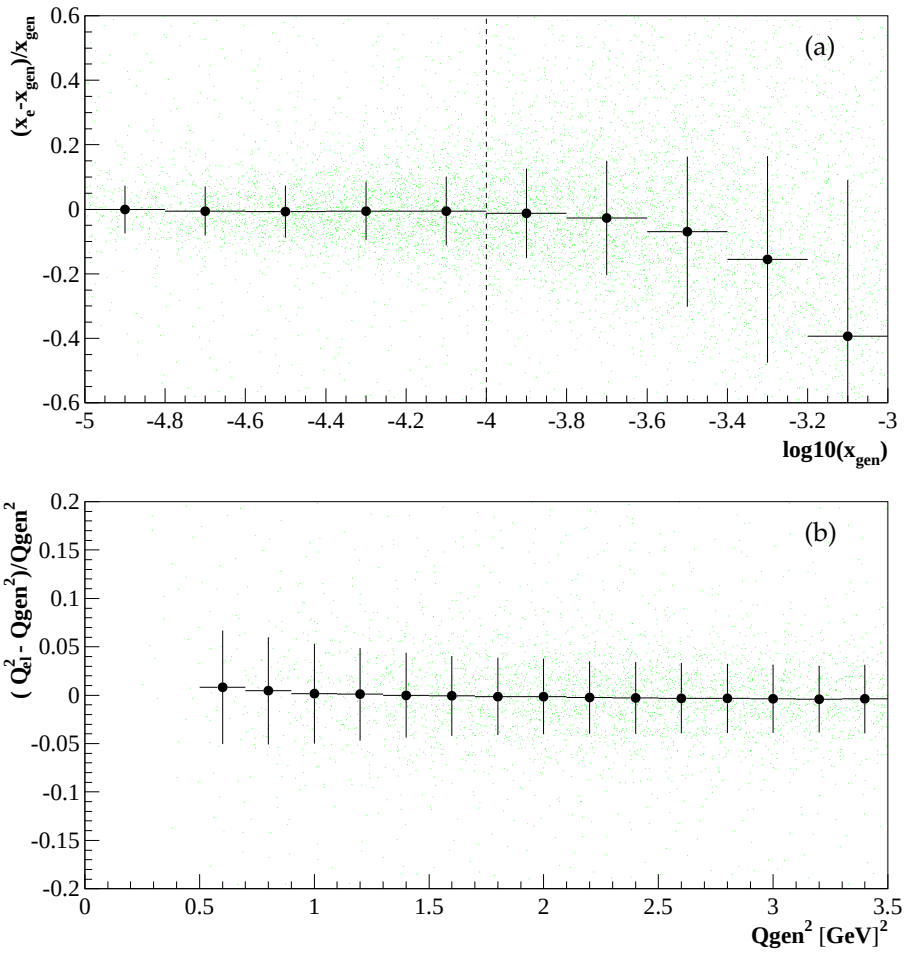

Figure 3.2: Resolution of the kinematical variables (a)x and (b)Q^2 in the case they are reconstructed with the electron method.

$x \approx 10^{-5}$ to almost 20% at $x \approx 10^{-3}$. The reconstruction of Q^2_e is precise, having relative values less than 5% (see Fig. 3.2(b)).

Since the relative resolution of x deviates significantly from the generated quantities for values of $x > 10^{-4}$, the electron method can be used to measure the cross section up to values of $x \approx 10^{-4}$ (see Fig. 3.2(a)).

The resolution of the electron method depends on the precise measurement of the angle of the scattered electron and on a precise energy measurement. This requires good alignment between the H1 subdetectors and a good electromagnetic calibration. The alignment of the detector components was derived in [100], and the calibration of the SpaCal calorimeter is presented in chapter 4.

Two important effects influence the reconstruction of events using the electron method at low

x (high y); photoproduction (γp) and initial state radiation events (ISR), both phenomena will be disscussed in section 3.6 and 6.5.2 respectively.

3.3.2 Hadron or JB Method

This reconstruction method uses the measurement of the four momentum of all particles which define the hadronical final state. In practise unfortunately, some hadrons are undetected due to the uncovered regions of the H1 detector used to inject the beams. Nevertheless it was shown by Jacques and Blondel [76] that the event kinematic can be calculated using the variable:

$$\Sigma = (E_h - p_{z,h}) = (E - p_z)_{had} \tag{3.5}$$

where $(E - p_z)_{had}$ is the difference between the energy E_h and longitudinal momentum $p_{z,h}$ of all particles which define the hadronical final state. Particles having low values of p_t can escape the detection, but these particles have a negligible contribution to the total $(E - p_z)_{had}$. The event kinematic is given by:

$$y_h = \frac{\Sigma}{2E_e} \qquad Q_h^2 = \frac{p_{t,had}^2}{1 - y_h} \qquad x_h = \frac{Q_h^2}{s y_h} \tag{3.6}$$

where $p_{t,had}$ correspond to the total transverse momentum of the hadronic final state:

$$p_{t,had} = \sqrt{(\sum_h p_{x,h})^2 + (\sum_h p_{y,h})^2} \tag{3.7}$$

being $p_{x,h}$ and $p_{y,h}$ the x and y four-momentum components of each particle which build the hadronical final state (see chapter 5 for more details).

The hadron method provides a precise measurement of y for low and medium values $y(< 0.15)$. But, the hadron method is not adequate to measure low Q^2 events, since the measurement of low p_t particles is not precise.

Using the four momentum of the hadronic final state, the angle of the hadronical final state θ_{had}

is reconstructed as:

$$\cos\theta_{had} = \frac{\Sigma^2 - p_{t,had}^2}{\Sigma^2 + p_{t,had}^2} \tag{3.8}$$

3.3.3 Σ Method

The Σ method combines the measurement of the scattered electron and of the hadronic final state. This method has a better precision than the hadron method for the event kinematic at low values of Q^2 and low values of y.

The inelasticity y is reconstructed similar to the hadron method, but the energy of the incoming electron E_{inc} is obtained using the longitudinal energy conservation, thus:

$$\begin{aligned} 2E_{inc} &= (E - p_z)_{had} + (E - p_z)_{el} = (E - p_z)_{tot} && (3.9)\\ &= \Sigma + E_e(1 + \cos\theta_e) && (3.10) \end{aligned}$$

this substitution ensures a correct reconstruction of the event kinematic at the hard interaction, even in the case where a photon from the incoming electron is radiated. The event kinematic is given by:

$$y_\Sigma = \frac{\Sigma}{\Sigma + E_e(1 + \cos\theta_e)} \qquad Q^2_\Sigma = \frac{E_e^2 \sin^2\theta_e}{1 - y_\Sigma} \tag{3.11}$$

Due to the correct reconstruction of ISR events, these can be used for the analysis. Since the emission of the photon of the incoming electron conduces to a reduced centre of mass energy s, the Σ method extends the measurement to low values of y. In contrast to the electron method, the ISR events are considered with the Σ method.

The resolution of the Σ method is given by,

$$\frac{\delta y}{y} = (1 - y)\left(\frac{\delta\Sigma}{\Sigma} \oplus \frac{\delta E_e}{E_e} \oplus \frac{\delta\theta_e}{\tan\theta_e/2}\right) \tag{3.12}$$

and is dominated by the experimental error of the term $\delta\Sigma/\Sigma$. At high values of y, the error on

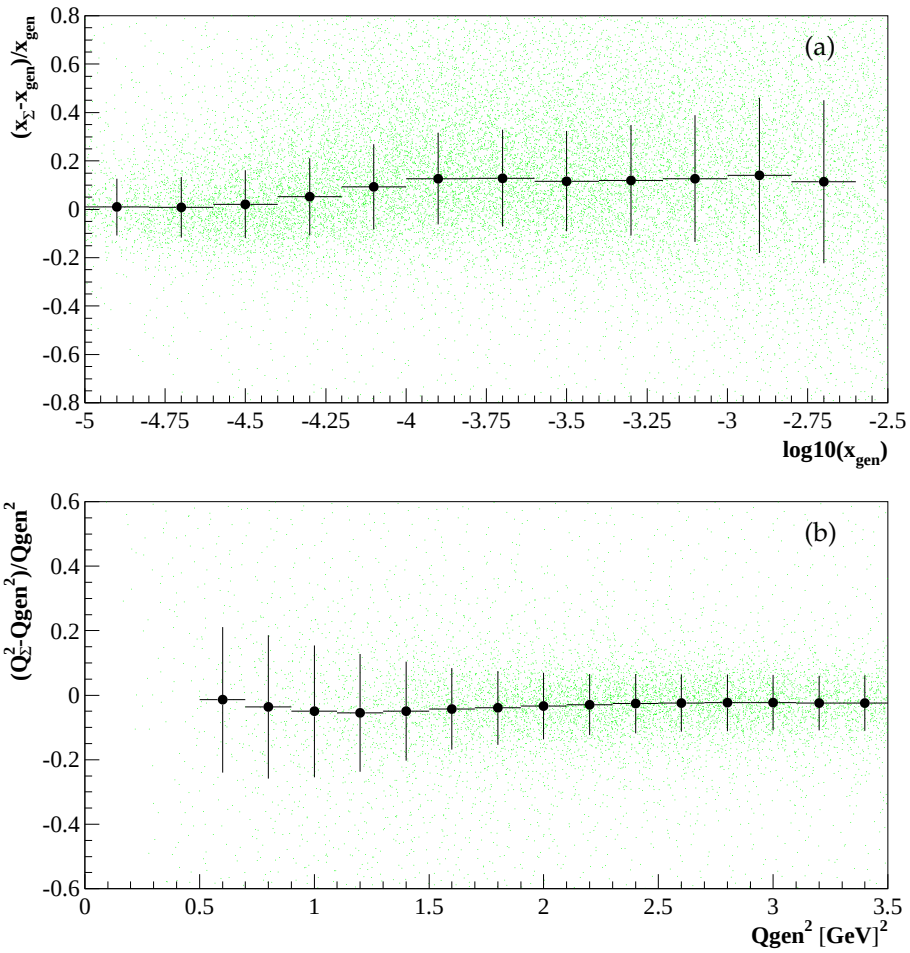

Figure 3.3: Resolution of the kinematical variables (a)x and (b)Q^2 in case they are reconstructed with the Σ method.

y decreases as $(1-y)$ and at low values of y the error is similar as the resolution of the hadron method.

The relative deviation of x_Σ and Q^2_Σ from the generated variables x_{gen}, Q^2_{gen} is shown in Fig. 3.3(a) and (b) respectively. Each point in Fig. 3.3 corresponds to a Gaussian fit restricted in the interval:

$$-0.3 \leq \frac{x_\Sigma - x_{gen}}{x_{gen}} \leq 0.3 \qquad -0.5 \leq \frac{Q^2_\Sigma - Q^2_{gen}}{Q^2_{gen}} \leq 0.5 \tag{3.13}$$

From Fig. 3.3 follows that the Σ method extends the measurement to higher values of x above 10^{-3} but is less precise than the electron method for the low x region (compare Fig. 3.3(a) with Fig. 3.2(a)). The resolution of x using the Σ method for values is of the order of 10% for

values of $x \approx 10^{-5}$. The resolution of Q^2 with the Σ method varies between 10% and 5% for $Q^2 < 1\,\text{GeV}$ and $Q^2 > 1\,\text{GeV}$ respectively.

In the region $10^{-4} \leq x_{gen} \leq 10^{-3}$, the Σ method tends to reconstruct x at higher values than it was generated (see Fig. 3.3(a)).

The projection of the relative deviation between x_Σ and x_{gen} for all values of x_{gen} is shown in Fig. 3.4. There it can be seen that the relative deviation has a tail over the whole generated phase space. The tail is created by the substraction of the identified noise in the LAr calorimeter. The dashed line in Fig. 3.4 show the relative deviation of x_Σ from x_{gen} in case the noise is not substracted. The high x (low y) kinematical region is complicated, because it is sensitive to noise substraction mechanisms, showering effects and losses of low p_t particles coming from the hadronical final state.

The losses and the identification of the noise are two different mechanism which can not be easily separated. The losses of low p_t particles are specially pronounced for low values of $W < 50\,\text{GeV}$. The comparison between W_Σ and W_{gen} improves considerably in case the identified noise is substracted from the measured energy and momenta in the LAr. This comparison is shown in Fig. 3.5(a) and (b). The losses of low p_t particles will be studied in section 6.1.4.

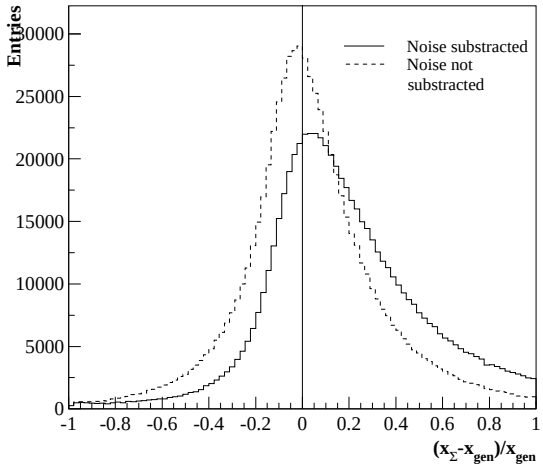

Figure 3.4: Relative deviation of x_Σ from x_{gen} in the case the noise in LAr is substracted (solid line) and not substracted (dashed line)

Although the noise substraction mechanism deteriorate the resolution in x, in chapter 5 it will be shown that the LAr noise has to be substracted in order to reproduce reasonably the behaviour of the data. The noise substraction mechanism and the identification of the noise sources have to be studied in detail, therefore such investigations are the subject of chapter 5.

In order to guarantie that the reconstructed variable x_Σ does not deviate from the generated, a special study of purity and stability will be performed and discussed in chapter 6.

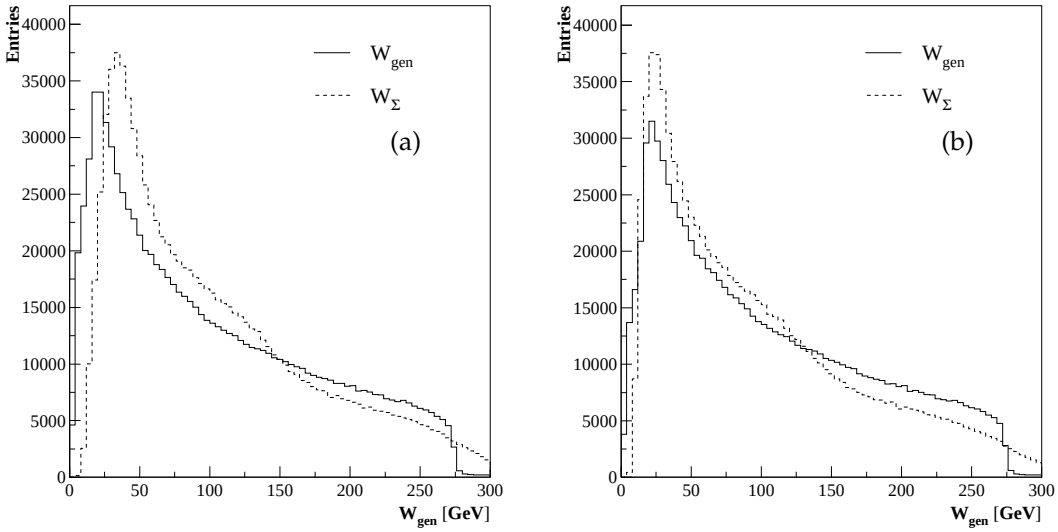

Figure 3.5: Comparison between W_{gen} and W_{Σ} not substracting the identified noise (a) and substracting the identified noise (b)

3.3.4 Double angle method

The double angle method uses the angle measurement of the scattered electron θ_e and hadron systems θ_{had} to calculate the event kinematics.

$$y_{DA} = \frac{\tan(\theta_{had}/2)}{\tan(\theta_{had}/2) + \tan(\theta_e/2)} \qquad Q^2_{DA} = 4(E^0_{inc})^2 \frac{\sin\theta_{had}(1+\cos\theta_e)}{\sin\theta_{had} + \sin\theta_e - \sin(\theta_{had}+\theta_e)} \quad (3.14)$$

where θ_{had} is determined from equation 3.8. To first order the double angle method is independent of the detector energy scale and therefore is mainly used for calibration purposes. For small values of θ_e or θ_{had} the resolution of the double angle method gets worse.

3.4 Electron Identification

As we have seen in the previous sections, the reconstruction of the event kinematic requires a correct identification of the scattered electron and of the hadronical final state. The electron identification for the lowQ^2 values studied in this analysis, start from energy clusters measured in the SpaCal calorimeter, while their corresponding track is reconstructed by the BST. In previous analysis[105] the cuts listed in Table 3.1 were used to identify the scattered electron using

the SpaCal and the BST. In the following sections these variables will be defined precisely.

Electron validation		
SpaCal:	Fiducial volumen	
	$R_{clog} < 4\,\text{cm}$	Eq. 3.17
	$E_{veto} < 1\,\text{GeV}$	
	$f_{had} < 0.15$	Eq. 3.18
BST:	$\Delta R = \lvert R_{bst} - R_{SpaCal}\rvert < 1.5\,\text{cm}$	Eq. 3.19
	$\lvert z_{BST} - 70\rvert < 30\,\text{cm}$	
	$R_{bst} > 10\,\text{cm}$	
	$N_{BST,hits} < 200$	

Table 3.1: Selection used to identify the scattered electron using the SpaCal calorimeter and the BST [105].

3.4.1 Electron identification with the SpaCal

The electron is identified as the most energetic cluster measured in the SpaCal calorimeter. This is justified since for values of $y < 0.5$ the energy of the scattered electron is greater than the energy of the hadronic jet. For high y this criterium is not appropriate, nevertheless in such cases, the energy of the hadrons scattered in the backward region deposit their energy over different cells of the SpaCal calorimeter. Since the hadronic showers are in general broader than the electromagnetic ones, two requirements apart of the maxima energy-cluster criteria are in addition applied to identify the electron.

One requirement is related to the transverse extension of the shower R_{clog} in the electromagnetic section of the SpaCal calorimeter. The other selection criterium is to have behind the electromagnetic cluster a minimal deposition of energy (f_{had}) in the hadronic section of the SpaCal. In the following paragraphs both variables will be defined in detail.

The energy of the scattered electron is commonly deposited over more than one cell of the SpaCal calorimeter, in average 20 cells build the electron cluster. The cluster energy E_{cl} is given by the sum of the energy E_i of all individual cells which belong to the cluster. The cell with the maximum energy is known as the "hottest-cell". The position of the electron cluster is defined as

$$x_{cl} = \sum_{i=1}^{N} x_i w_i \qquad y_{cl} = \sum_{i=1}^{N} y_i w_i \tag{3.15}$$

where x_i and y_i are the geometrical centres of the cells and the weight of the cell is defined as

$$w_i = \frac{max(0, w_{cut} + ln(E_i/E_{cl}))}{\sum_{j=1}^{N} max(0, w_{cut} + ln(E_i/E_{cl}))} \tag{3.16}$$

The parameter w_{cut} decides which cells will be taken into account in the reconstruction of the cluster position. Through the variation of the w_{cut} parameter the cluster position determination was optimized, leading to a value of $w_{cut} = 4.8$ [78].

There are different possibilities to calculate the transverse extension of the shower. In [89] was shown that the logarithmic weighting has the best resolution to distinguish clusters of electromagnetic and hadronic origin. The transverse extension of the shower is defined as:

$$R_{clog} = \sqrt{\sum_i (R_i w_i)^2} \tag{3.17}$$

where R_i is the distance of the cell i to the centre of the cluster. Fig. 3.6 shows the transverse extension of the cluster for electrons having energies $20 < E_e < 30\,\text{GeV}$.

The energy of electromagnetic clusters are mostly contained inside the $27X_o$ electromagnetic section of the SpaCal. The hadronic part of the spacal was used to sum the energy $E_{had,spa}$ deposited behind the most energetic cluster in a cylinder having an extension of 15 cm of radius. If the fraction of the energy E_e of the cluster to $E_{had,spa}$ is greater than 15% then the cluster is identified to have an hadronic origin. The fraction of E_e and $E_{had,spa}$ will be in denoted as f_{had}:

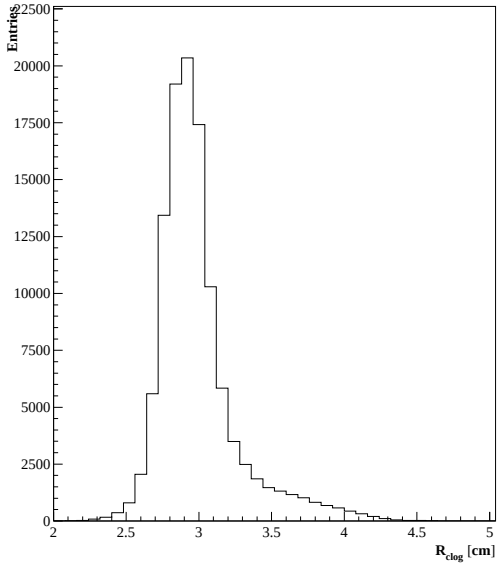

Figure 3.6: The transversal extension of the electron cluster R_{clog}.

$$f_{had} = \frac{E_{had,spa}}{E_e} \tag{3.18}$$

In case the scattered electron is reconstructed inside the insert module of the SpaCal calorimeter, a maximum energy of $E_{veto} < 1\,\text{GeV}$ in the veto cells is required, in order to loose not too

much energy due to shower leakage.

3.4.2 Electron identification using the BST

The identification of the scattered electron is optimised by reconstructing in addition its track. This can be performed using the BST or the BDC and the central tracking devices.

The reconstruction of the electron track with the BST was initially implemented in [90] where the BST consisted only of 4 planes. Afterwards the reconstruction algorithm was implemented in [106], it starts with the measured position of the SpaCal cluster. The three $r-$strip sectors localised around the azimuthal position ϕ_{spa} of the SpaCal cluster are selected. The r coordinate of each BST hit is projected along the line which connects the hit and the SpaCal cluster to the outermost BST plane. The projection of all hits enters into a histogram. The line which connects the maximum of the histogram with the SpaCal cluster is used as the starting point for the track finding.

The track finding is performed using an iterative technique, where all hits of the three selected sectors enters the minimisation procedure. The contribution of each hit is weighted depending on the distance of the hit to the track around an effective corridor. At the beginning of the track finding this corridor is equal to the SpaCal resolution, for the next iteration the corridor is reduced until the BST resolution $5\sigma_{BST} \approx 250\mu$m is reached.

Once a track is reconstructed with the BST, the additional requirement:

$$\Delta R = |R_{BST} - R_{SpaCal}| < 1.5\,cm \tag{3.19}$$

is applied, in order to minimise the influence of background γp events [105].

R_{BST} in Eq. 3.19 is the transverse distance of the impact point of the scattered electron on the SpaCal plane to the centre of the beam pipe. The subindex BST means that the BST track was extrapolated to the SpaCal surface in order to determine the scattered electron position on the SpaCal front plane. In analogy, R_{SpaCal} is the same transverse distance but measured with the coordinates of the hottest cluster.

Due to acceptance problems of the BST during the shifted vertex data period [106], the $R_{BST} >$ 10 cm cut is applied. In the following section, the efficiency of the cuts introduced until now are studied.

3.5 Efficiency of Electromagnetic cuts

The efficiency of the cuts listed in table 3.1 is investigated using a sample which is almost free of background events. This study is performed using data and the Signal MC DJANGOH. The efficiency study is important to guaranty that the applied cut, reject the same fraction of events for data and MC.

To select a sample almost free of background a so called tagged ISR sample is used, where the scattered electron is identified as in the standard selection (table 6.1) and the initial state photon is detected using the photon detector.

For normal DIS events the longitudinal momentum has to be conserved and equal to $2E_{inc} = 55\,\text{GeV}$, nevertheless this requisite is not satisfied in case the electron radiates a photon. In such case, from longitudinal momentum conservation follows:

$$\begin{aligned} 2E_{inc} - (E - P_z)_\gamma &= (E - P_z)_{el} + \Sigma \\ &\approx 2E_e + 2y_{had}E_{inc} \\ E_{inc} &\approx E_e + E_\gamma \end{aligned} \tag{3.20}$$

Thus, for ISR events the energy of the incoming electron is basically distributed between the energy of the photon and the energy of the scattered electron. Since, the radiated photon can be detected in the photon-tagger of the luminosity system and the energy of the electron can be measured in the SpaCal calorimeter, a sample of tagged-ISR events can be used to study the efficiency of the cuts used to identify the scattered electron. In order to have a clean sample, events with *only one* cluster in the SpaCal are selected.

The selection of tagged-ISR events requires a minimal photon energy of 1 GeV. In addition no activity in the electron tagger is required to reduce Bethe Heitler process. Since ISR events are mainly localised at low y, only events with $y_{had} < 0.1$ are considered.

In order to calculate the efficiency of the cut, the electron identification selection given in Table 3.1 in addition to the tagged-ISR selection is applied. The efficiency of the cut is calculated as the fraction of events accepted for the whole sample N_{all} with the events which are accepted

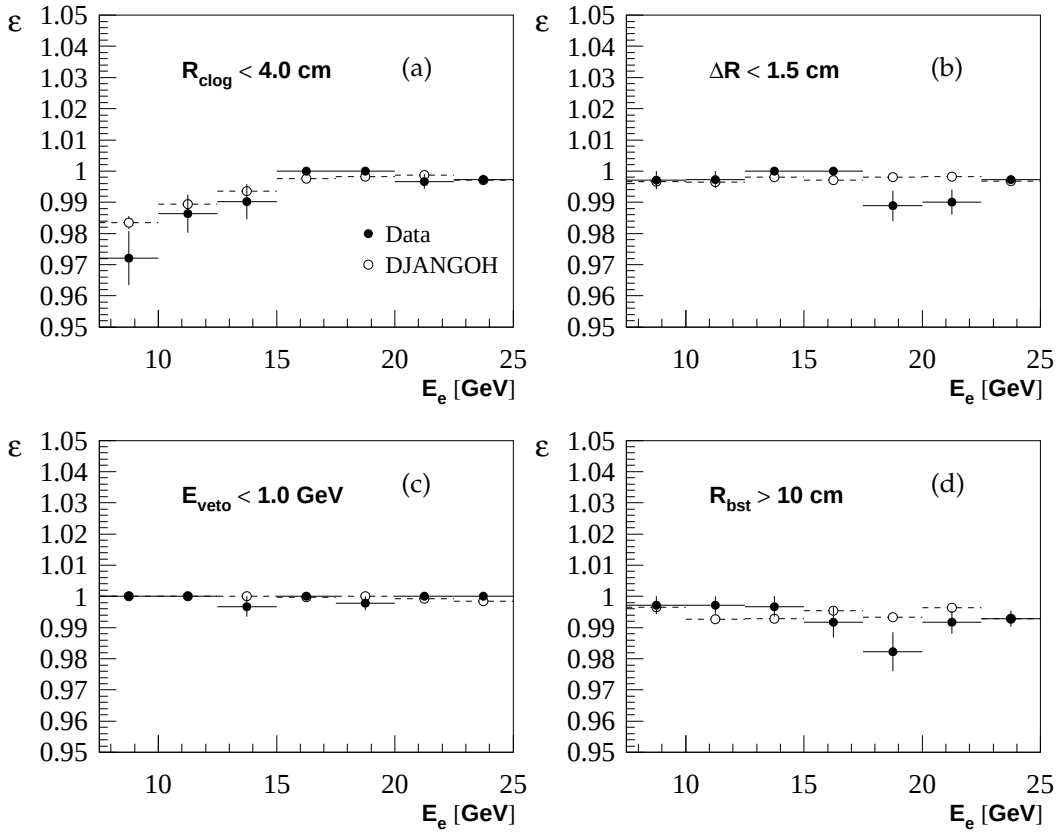

Figure 3.7: Efficiency of the electron identification cuts as function of the energy of the scattered electron E_e. (a) $R_{clog} < 4\,\text{cm}$ (b) $\Delta R < 1.5\,\text{cm}$ (c) $E_{veto} < 1\,\text{GeV}$ and (d) $R_{BST} > 10\,\text{cm}$ cut. The efficiency is derived using tagged-ISR events. Close points are Data and open circles are the signal DJANGOH MC simulation.

relaxing the cut.

$$\epsilon(cut) = \frac{N_{all}}{N_{all} + N_{rej,cut}} \tag{3.21}$$

In Fig. 3.7 the efficiency is shown of the cuts listed in table 3.1 as function of the energy of the scattered electron E_e. In Fig. 3.7(a) is shown the efficiency of the R_{clog} cut. One can see, that the efficiency of the R_{clog} cut is fully in agreement with the signal MC DJANGOH. In Fig. 3.7(b) and (d) are shown the efficiency of the Spacal-BST matching ΔR and the $R_{BST} > 10\,\text{cm}$ cut. In Fig. 3.7(c) is shown the efficiency of the E_{veto} cut. In general, all investigated cuts are well described by the DJANGOH MC, rejecting only a small fraction of events for data and MC having differences which do not exceed 2%.

3.6 Photoproduction

The cut efficiency previously presented compares the data with the signal MC DJANGOH using a sample which is almost free of background. But the real DIS selection is influenced by the photoproduction background. Therefore it is important to estimate the influence using the data and the background MC PHOJET.

In γp events, the interaction between the electron and the proton occurs at very low $Q^2 < 10^{-2}\text{GeV}^2$, having thus an ep interaction mediated by an almost real photon. For small values of Q^2, the transverse momentum of the scattered electron is low, and the probability that the scattered electron escapes the detection of the backward detectors is high. However a fraction of γp events can satisfy the electron identification criteria, when a particle coming from the hadronic final state is wrongly identified as the scattered electron.

In order to determine how many photoproduction events pass the DIS selection, a sample of events where the scattered electron is detected in the ET is used, and at the same time fulfil the DIS selection listed in table 3.1. Part of the photoproduction events are detected directly by the electron tagger ET. The subtrigger 115 is used to select events which posess a shower good contained in the electron tagger. The energy in the electron tagger is required to be greater than 7 GeV and the energy deposited in the photon tagger is required not to exceed 2 GeV to exclude Bethe Heitler events.

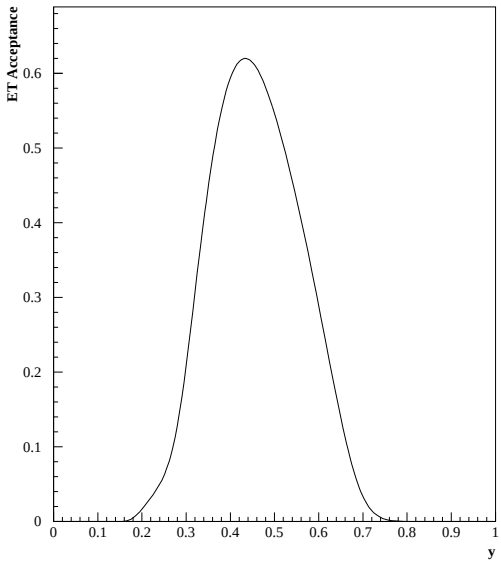

Figure 3.8: Acceptance of the ET as function of y for the shifted vertex period [79].

The acceptance of the ET is limited and only a small fraction of events in a certain kinematic range can be detected. The acceptance of the ET as function of y is show in Fig. 3.8 and is calculated using different fills having the same beam position delivered by HERA. The acceptance function is used to correct event by event the photoproduction contribution in the PHOJET MC.

One additional background source for the γp events are the overlap of Bethe-Heitler and normal DIS events. For such events $E - p_z$ is expected to be greater than 55 GeV. The overlap

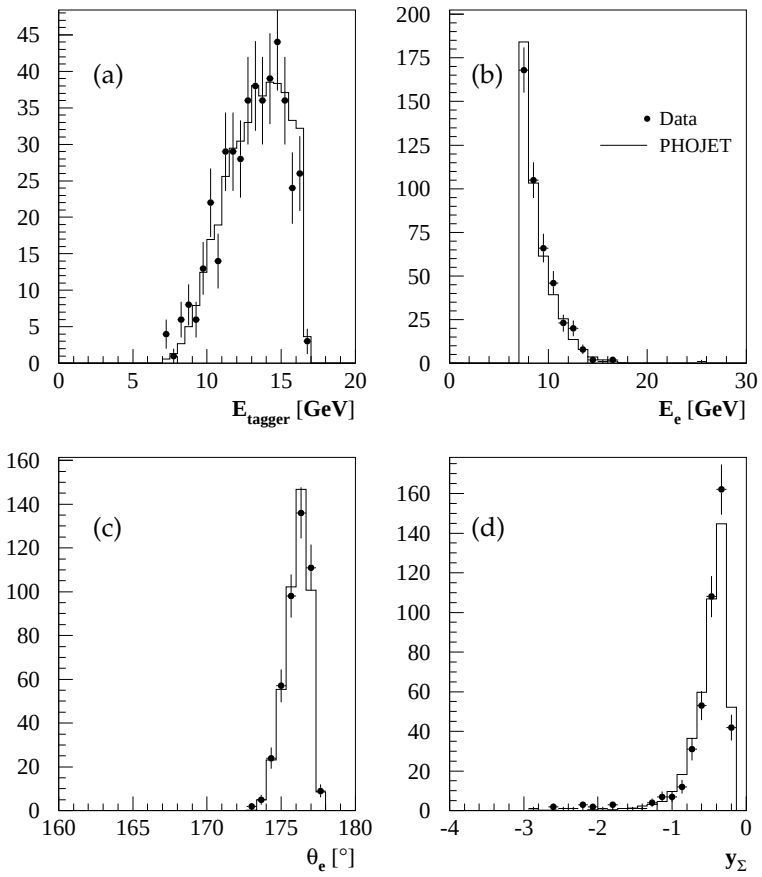

Figure 3.9: Comparison of γp events detected in the ET and passing the DIS selection with the contribution given by the PHOJET MC. (a) Energy measurement of the scattered electron in the ET. (b) Energy of the "misidentified electron" (hadron) measured by the SpaCal calorimeter. (c),(d) polar angle and y_Σ of the misidentified electron

events are suppressed requiring that the $(E - p_z)_{tot}$ defined as in Eq. 3.22 be lower than 70 GeV.

$$(E - P_z)_{tot} = \Sigma + (E - P_z)_{el} + 2E_{e,tagger} + 2E_{\gamma,tagger} \tag{3.22}$$

In Fig. 3.9 is shown the comparison of data and Phojet MC for events which pass the DIS selection and the tagged-selection. The Phojet contribution is normalised to the data using the integral of the distribution of the energy measured by the wrongly identified scattered electron by phojet I_{phojet} and in the data I_{data}. The luminosity of phojet is thus obtained as:

$$L_{phojet} = \frac{I_{phojet}}{I_{data}} L_{data} \tag{3.23}$$

Fig 3.9(a) shows the energy measured in the electron tagger and Fig. 3.9(b) shows the energy of the hadron that was identified as the scattered electron, normalized according to Eq. 3.23. The photoproduction background is correctly described by PHOJET, hence it can be used to estimate the background contribution of the final DIS selection. In such way, the photoproduction contribution will be added to the DJANGO MC sample of DIS events to reproduce the behaviour of the data.

Chapter 4

SpaCal Calibration

As it was mentioned in the last chapter, the measurement of the proton structure function is only possible if the event kinematics is correctly and precisely reconstructed. The resolution of the reconstruction methods relies directly on the precision of the measurement of the angles and energies of the scattered electron and of the hadronical final state.

Since the energy measurement enters directly to the event kinematics, especially for the electron method, and represent the largest source of systematic uncertainty for the measurement of F_2 for values of $x \geq 10^{-4}$, it is important to perform a precise calibration of the energy measured by the SpaCal calorimeter on analysis level. In this chapter the calibration of the SpaCal calorimeter and the determination of its uncertainty is explained.

In section 4.1 the calibration sample is explained, afterwards in section 4.2 the method used to calibrate the shifted vertex data and the MC sample is introduced. Since the energy measurement has to be understood better than the percent level, the double angle calibration procedure originally introduced in [89] is used to calibrate the electromagnetic section of the SpaCal calorimeter. The scale of the electromagnetic energy measurement is derived in section 4.3 using the cluster of the scattered electron with energies of 27.5 GeV. In order to study the scale of the energy measurement at lower energies, the reconstruction of the invariant mass of π^0 decays using the SpaCal calorimeter is presented in section 4.5.

4.1 Calibration Sample

In DIS events at low values of Q^2, the energy distribution of the scattered electron has a characteristic shape with a maximum close to the electron beam energy commonly known as the

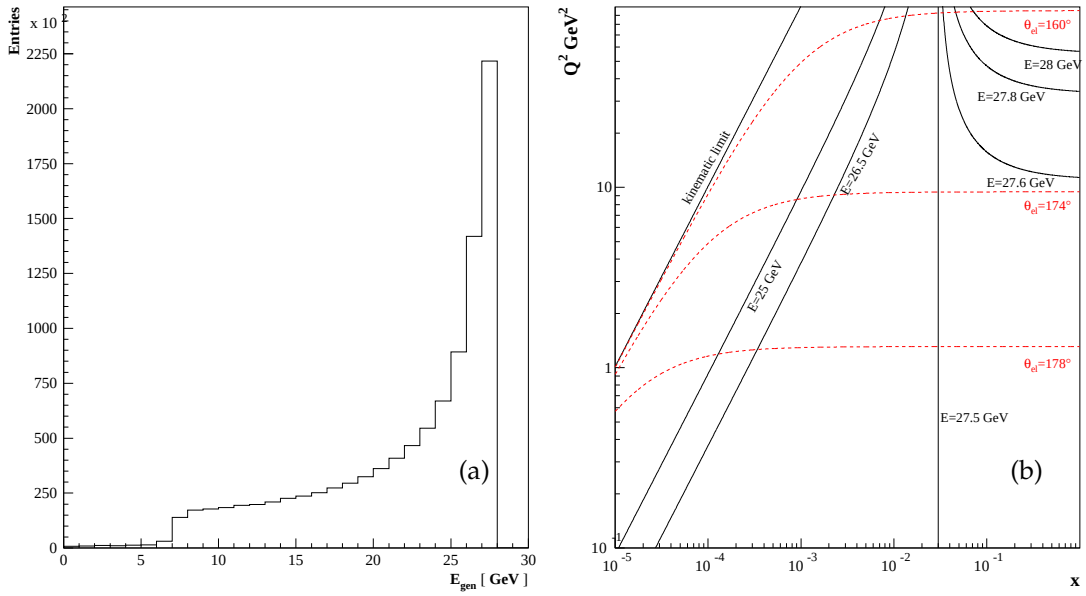

Figure 4.1: (a) Scattered electron energy distribution for DIS events at generator level (b) Kinematical plane trajectories for different energies (solid lines) of the scattered electron. In red lines are also illustrated contours of constant angles of the scattered electron θ_e.

kinematic peak. In Fig. 4.1(a) the energy distribution of the scattered electron at generator level for a DIS selected sample is shown.

The kinematical properties of events located in the kinematic peak region are unique and are used to determine the scale of the electron energy measurement. In Fig. 4.1(b), the $Q^2 - x$ plane is shown with different contours of constant scattered electron energies. If the energy of the scattered electron coincides with the energy of the incoming electron, then the contour correspond to a fixed $x \approx 0.032$ for all values of Q^2. This kinematic region is only accessible for larger electron scattering angles as can be seen from Fig. 4.1(b), where the angle of the scattered electron is also shown. At this value of x the proton structure function F_2 is approximately flat (see Fig. 1.5) therefore events located in the kinematic peak region are almost independent of structure function assumptions and thus appropriate to perform calibration studies [80].

The calibration of the SpaCal calorimeter begins already during the data taking. The variation of the gains of the photomultipliers are measured with the help of the light-emitting-diode (LED) system situated at the back side of the calorimeter [81]. Each photomultiplier receives well defined constant light pulses and afterwards photodiodes are used to identify instabilities of the LED intensity. The instabilities are read out to the data base and afterwards an offline correction of the photomultiplier gain is performed.

After applying the correction factors determined by the LED system, the inner cells of the

calorimeter are calibrated using events localized in the "kinematic peak" region [82]. Due to the decreasing statistic at larger Q^2 the outer part of the calorimeter is calibrated with muons coming from either cosmic rays or from proton beam halo [83] events.

Nevertheless an improved calibration of the SpaCal calorimeter, which is able to reduce the uncertainty of the F_2 measurement at high values of x, can only be achieved on analysis level. The energy calibration has to provide:

- a good energy resolution, therefore it is vital to obtain a relative equalization of response of the calorimeter cells.
- a correct reconstruction of the event kinematics, therefore the absolute energy scale has to be determined.

The method to calibrate the SpaCal calorimeter used in this analysis was introduced in [89] and uses events localized in the kinematic peak region. The SpaCal energy measurement is compared with a reference energy obtained by the double angle (DA) reconstruction method, which will be explained in section 4.2.

In this analysis the "hottest-cell" calibration method introduced in [88] is used as a cross check of the energy calibrated with the DA method. The "hottest-cell" method compares directly the energy distribution of the data and the MC simulation in the kinematic peak region.

4.2 Calibration with the Double angle method

As we have seen in section 3.3.4 the event kinematics can be completely reconstructed using the angle of the scattered electron θ_e and of the hadronic final state θ_{had}. This allows to derive the energy of the scattered electron independently of the SpaCal energy measurement. The energy measured by the DA method (DA energy) is given by:

$$E_{DA} = E^0_{inc} \frac{1 - y_{DA}}{\sin^2 \theta_e / 2} \tag{4.1}$$

Following Eq. 4.1 one can see that the DA energy can be reconstructed in the kinematic peak region $E^0_{inc} \approx 27.5\,\text{GeV}$, if the scattered electron is measured at large angles $\theta_e \approx 180^\circ$ and low values of y (see also Fig. 4.1(b)).

The angle θ_e of the scattered electron is measured with the BST. In case the event is out of the acceptance of the BST, then the BDC and the central tracking devices are used to reconstruct the electron scattering angle. In both cases a well reconstructed vertex around 30 cm with respect the expected collision point at $z = 70$ cm is required. Events at low y are selected applying a cut on the hadronic angle $\theta_{had} < 80°$, this cut allows a maximum value of y of approximately 0.15. The influence of events at very low y where the hadronic final state escapes often undetected in the forward direction, was suppressed by requiring $\theta_{had} > 15°$.

In order to minimize contributions of photoproduction background events, an additional SpaCal selection is applied. Only events with exactly one cluster in the SpaCal calorimeter with an energy in the kinematic peak region 20 GeV$< E_e <$ 32 GeV are accepted. In addition the radius of the cluster R_{clog} must be less than 4 cm. The cuts introduced in this paragraph and in the previous one constitute the *DA selection*.

The energy measured by the SpaCal calorimeter can be calibrated with the DA energy E_{DA} only in case the resolution of the DA energy is better than the resolution of the SpaCal energy measurement. This can be verified using the MC simulation where the generated energy E_{gen} is taken as the reference for both the DA and the SpaCal energy measurements. The resolution of the DA energy and of the SpaCal energy measurement are compared in Fig. 4.2. A shift up to 2% of the generated variable is observed in case of the SpaCal measurement, while E_{DA} deviates by only 0.4%. Therefore the DA energy is well suited to be the reference energy scale for the SpaCal calibration.

The calibration procedure is an iterative process, where the reference energy E_{DA} is compared to the uncalibrated measured energy E^{uncal}_{SpaCal} using the previous DA selection. The calibration gain factors g are obtained such that $E^{cal}_{SpaCal} = (1+g)E^{uncal}_{SpaCal}$, thus the deviation of $\delta = E_{DA}/E^{uncal}_{SpaCal}$ from 1 correspond to the needed calibration factor.

In order to ensure homogeneity over the whole SpaCal plane the following calibration factors are required:

1. **Gain** calibration factors for each cell of the calorimeter.
2. **Inbox and Cracks** calibration factors which correct for the losses of energy due to the SpaCal cell module geometry.
3. **Radial** calibration factors, calculated as function of the transversal distance of the impact point of the scattered electron to the center of the beam pipe R_{SpaCal}.

This set of calibration constants will be applied sequentially to the uncalibrated energy E^{uncal}_{SpaCal}.

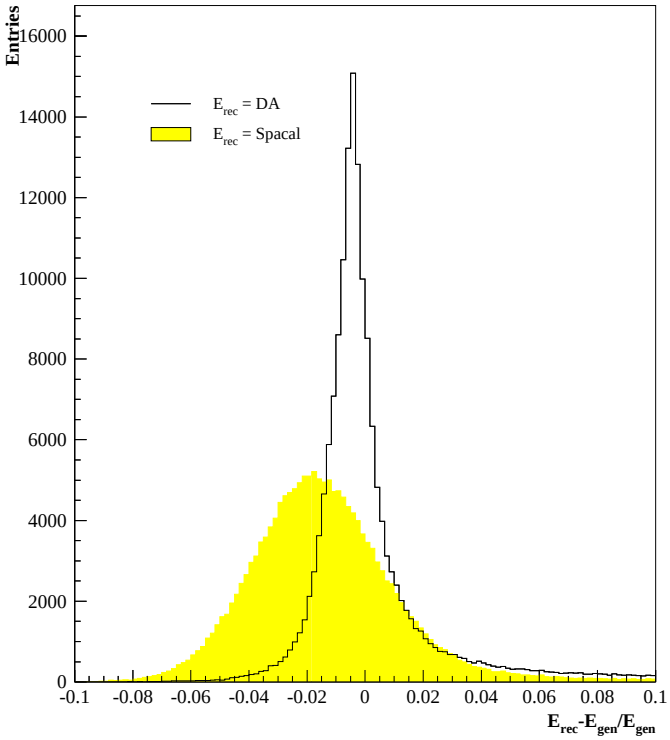

Figure 4.2: Resolution of the reconstructed energy measured by SpaCal (shaded histogram) and determined by the Double angle method (solid line)

First, each cell belonging to the electron cluster is corrected with its corresponding gain factor (see section 4.2.1). Next the inbox corrections will be applied (see section 4.2.2) according to the coordinates of the hottest cell of the electron cluster. Finally, using the coordinates of the hottest cell, the corresponding radial calibration factors are applied (see section 4.2.3). This serie of corrections constitute the main DA calibration chain. The calibration procedure is performed for both data and MC.

4.2.1 Cell Gains

The first calibration constants are derived for each cell of the SpaCal calorimeter. As we have seen from section 3.4.1, the energy measured by SpaCal is constructed as the sum of the energies of the cells which are assigned to the electron cluster.

$$E_{SpaCal} = \sum_{cell_i} E_i \tag{4.2}$$

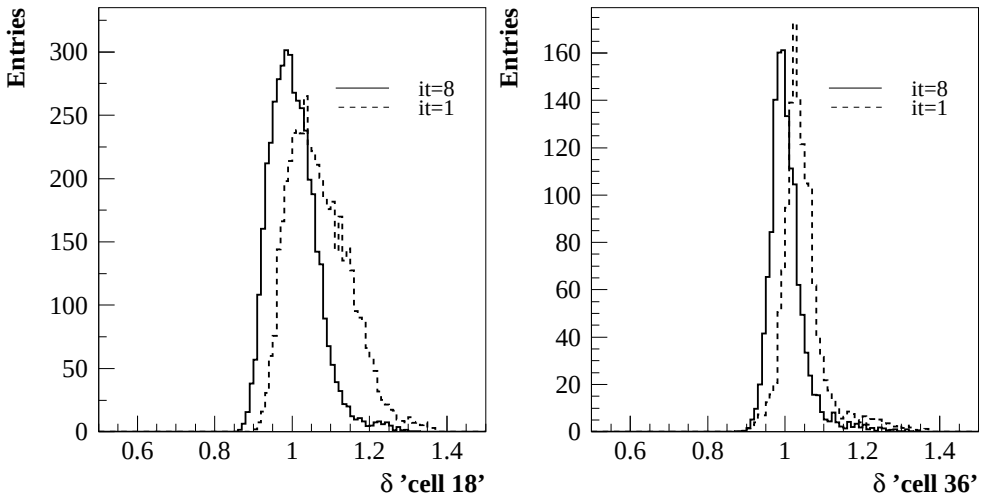

Figure 4.3: δ pull distributions for two cells of the SpaCal calorimeter. The dashed line correspond to the first gain determination while the solid line is the pull distribution obtained after eight iterations

The gain of each calorimeter cell is calculated using an iterative procedure. The energy depositions of all cells which form the electron cluster are used to define individual "cell-pull" distributions δ_{cell-i}.

Each cell contributes to the pull distributions of the entire sample with a weight w_i given by the fraction of its measured energy E_i to the total energy of the electron cluster E_{SpaCal}. Thus, the pull distribution for the $cell - i$ is defined as,

$$\delta_{cell-i} = \frac{E_{DA}}{E^{uncal}_{SpaCal}} \quad \text{having a weight} \quad w_i = \frac{E_i}{E^{uncal}_{SpaCal}} \tag{4.3}$$

If all cells would be already calibrated, the δ_{cell-i} pull distribution should be centered around 1. If this is not the case, then the deviation of the δ_{cell-i} distribution from 1 corresponds to the gain factor with which the cell has to be corrected. The dashed line in Fig. 4.3 shows the pull distribution for two example cells of the SpaCal calorimeter. Since the shape of the pull distribution is generally not of Gaussian shape, the deviation of δ_{cell_i} to 1 is obtained using a robust fit which removes the outliers in the distribution [84]. In cases where cells do not have enough statistics to perform an individual fit, a global fit for all those cells is performed.

In order to ensure the convergence of the calibration method, an iterative gain determination of the cells is performed. The gains of the iteration it are obtained using:

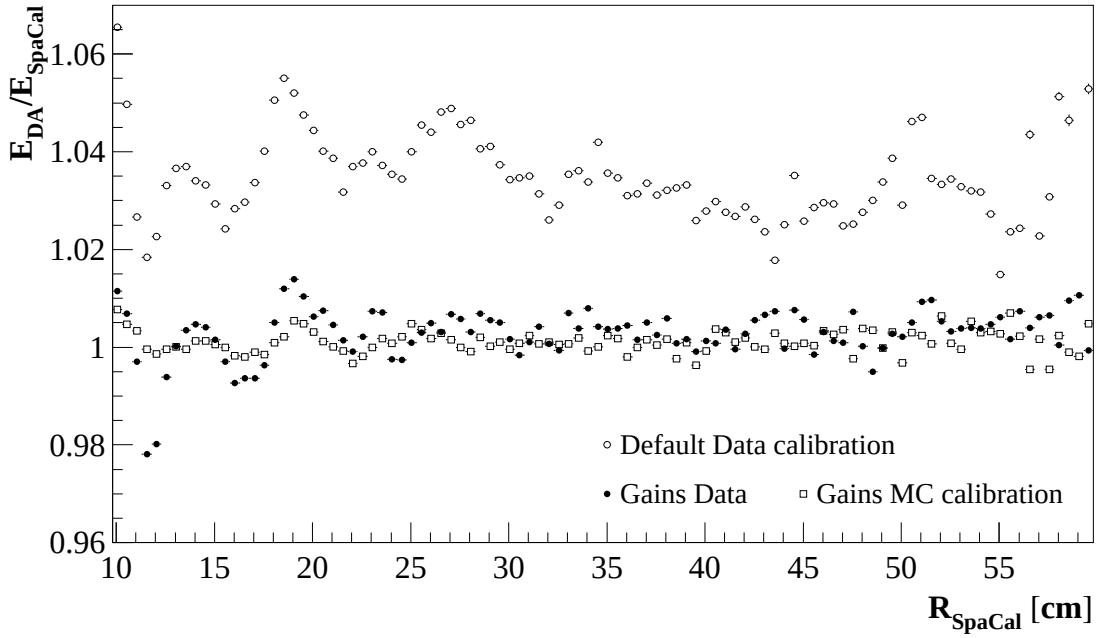

Figure 4.4: Calibrated and uncalibrated E_{DA}/E_{SpaCal} distributions for data and MC of the shifted vertex period, as function of R_{SpaCal}.

$$E^{uncal}_{SpaCal} \rightarrow E^{it}_{SpaCal} = \sum E_i \prod_{k=0}^{k=it-1} (1+g_k)$$

and thus the pull distribution for the $cell-i$ for the iteration it is changed according to:

$$\delta^{it}_{cell-i} = \frac{E_{DA}}{\sum_i E_i \prod_{k=0}^{k=it-1}(1+g_k)} \qquad w^{it}_i = \frac{E_i(1+g^{it}_i)}{\sum_i E_i \prod_{k=0}^{k=it-1}(1+g_k)} \tag{4.4}$$

for $k = 0$ the gains $g_k = 0$ and in this case Eq. 4.4 is equal to Eq.4.3. Usually 8 iterations are needed to achieve a result which is stable within 0.001%. In Fig. 4.3 are also shown the pull distribution for the same SpaCal cells after applying the gains obtained after eight iterations.

The gain factors correct the energy measurement by 2% to 3%. Fig 4.4 shows the variation of δ as function of the transverse distance of the cluster from the center of the beam pipe R_{SpaCal} for the uncalibrated δ and after the gains are applied. A significant improvement is achieved taking the gains into account. Nevertheless some variations stay, which are minimized by the following steps.

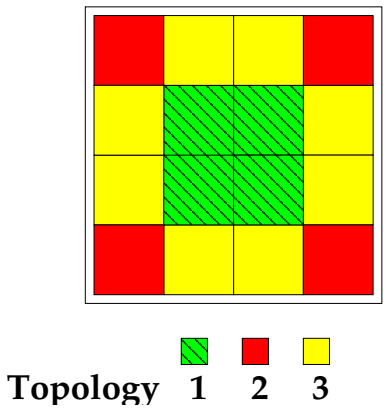

Figure 4.5: Schematic view of one module of the SpaCal calorimeter. Cells in the middle, corner and border define the topology 1,2 and 3, respectively.

4.2.2 Inbox Corrections

Using the gains calibration constants derived in the previous section, the energy measured by the SpaCal calorimeter has to be corrected further due to several effects. As we have seen in section 2.2.1, the SpaCal calorimeter is constructed of supermodules containing 16 cells each. Therefore energy losses due to the dead material present between the supermodules is expected. Cells placed in the corner of the supermodule are more affected by energy losses than the cells situated in the middle of the 16 cell module.

In order to compensate for this losses, the measurement of the energy is corrected as function of the impact point of the electron candidate *inside* the cell. In order to take into account the position of the cell inside the supermodule, three topologies are defined as illustrated in Fig. 4.5. The cells situated in the middle, corners and at the borders define the topologies 1,2 and 3 respectively.

For each inbox topology the cell is divided in a grid with spacing of 8 mm. The coordinates of the hottest cell are used to determine the position of the electron candidate inside the cell. The inbox corrections are derived using the same DA selection as in the the gain determination. Since the insert modules have cells with different geometry and are affected by leakage, an additional cut on $R_{SpaCal} > 10\,\text{cm}$ was applied. The inbox corrections are obtained with the same robust fit procedure as the gain determination, but no iteration for the inbox correction is performed.

Fig. 4.6 shows the correction factors for data and MC due to the energy losses between the modules. For data cells in the corner are corrected up to 2%, while 1% of correction is obtained for the border cells and up to 0.5% for the cells located in the center of the module.

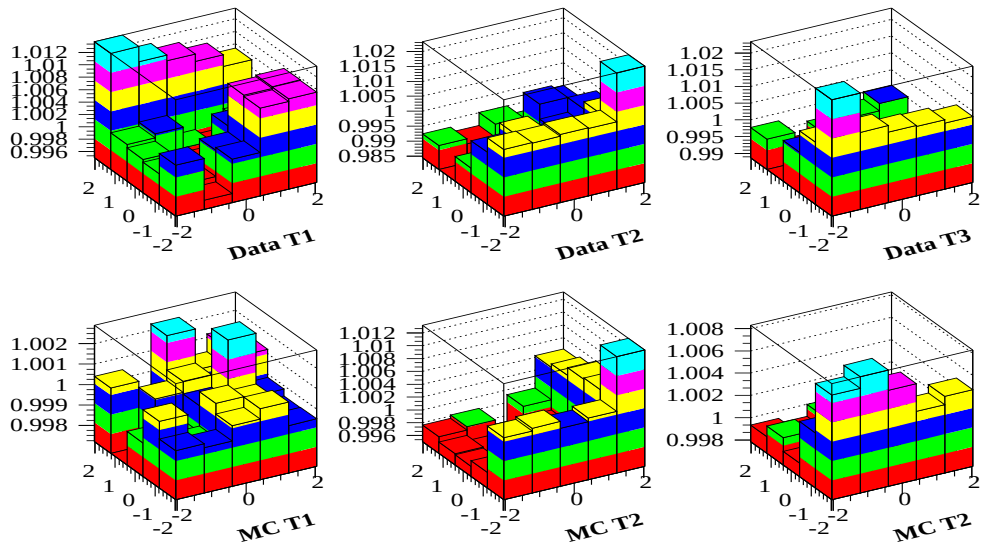

Figure 4.6: Calibration factors for the different cell topology inside the module for data and MC. T1,T2 and T3 correspond to the different topologies.

Another source of energy losses in the calorimeter is due to the inhomogeneity of the SpaCal cells inside the module. Since the variable $R_{box} = max(|x_{cell}|, |y_{cell}|)$ covers the calorimeter surface in squares, it was used to correct the energy losses between the cells. The corrections are derived comparing the DA energy with the calibrated SpaCal energy with gains and inbox corrections. Four sets of calibration factors as function of R_{box} are derived for 4 ϕ sectors, each covering one quarter of the SpaCal surface.

This procedure corrects the energy measurement by 0.3% in addition. Fig. 4.7 show the deviation of the energy measurement from the reference energy E_{DA} as a function of R_{SpaCal} after the inbox and crack calibration factors are applied.

4.2.3 Radial Corrections

As we can see from Fig.4.4 and Fig.4.7 after the gains inbox and crack calibration factors are applied, a significant improvement of the measured energy over the SpaCal plane is achieved. Nevertheless a radial dependence of the calibrated δ pull quantity up to 1.2% still remains. Such a deviation is probably due to dead material located in front of the SpaCal calorimeter which is not properly implemented in the MC simulation. In particular the deviations observed at $R_{SpaCal} \approx 12.20\,\text{cm}$ corresponds to the CIZ and COZ electronics [102]. This dependence is corrected by deriving the last calibration factors as function of the measured radius R_{SpaCal}. In analogy to the crack corrections, four sets of calibration factors are derived for the same 4 ϕ

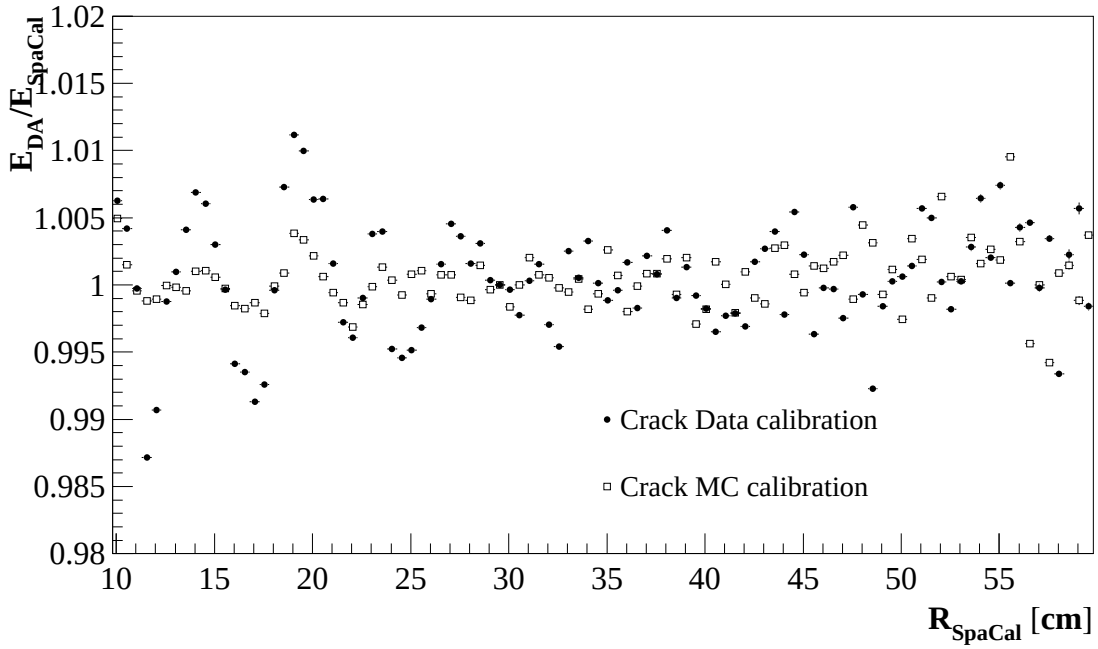

Figure 4.7: E_{DA}/E_{SpaCal} distribution using the gains, inbox and crack calibration factors as function of R_{SpaCal}.

sectors.

In Fig. 4.8 is shown the radial dependence of δ after the complete calibration procedure is applied. The remaining differences between data and MC do not exceed 0.2% for allmost all the regions covered by the SpaCal calorimeter.

4.2.4 MC Smearing

The uncalibrated and calibrated energy distribution of the scattered electron for the whole calibration sample is shown in Fig. 4.9(a) and (b). It can be seen, that the mean value of data and MC of the energy distribution agrees after the whole DA calibration factors are applied. Nevertheless, the MC resolution is better than the resolution of the data. Therefore it is necessary to smear the MC simulation in order to fit its resolution to the one of the data.

In order to determine the optimum value of the smearing, the calibrated energy in the MC was smeared with different factors varying between 0% and 0.4%. The value of χ^2 of the deviation between data and MC was used to determine the optimum value. The best value was found to be 0.2%. In Fig. 4.9(c) the calibrated energy distributions of data and MC with the additional

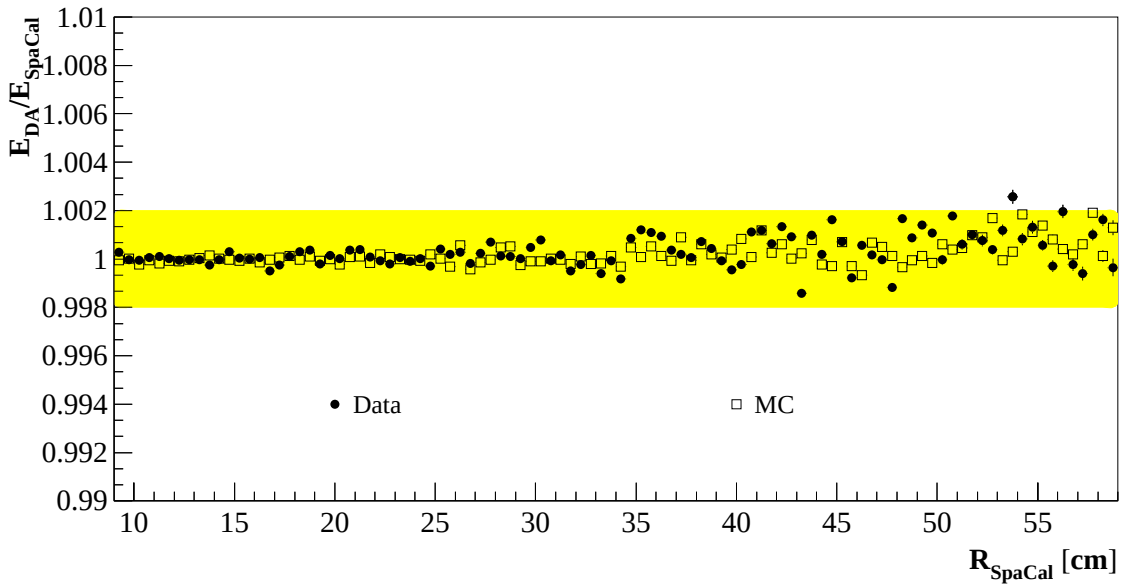

Figure 4.8: E_{DA}/E_{SpaCal} distribution using the whole calibration factors as function of R_{SpaCal}.

smearing of 0.2% are shown.

However the smearing of the MC results in a constant systematic shift of the energy distribution of about 0.15%. This systematic shift can be avoided by introducing in the MC calibration chain, the smearing value starting from the inbox corrections. In Fig. 4.9(d) is shown the calibrated energy distribution when the smearing is applied to the MC calibration. All distributions in Fig. 4.9 are normalized using their total number of events.

4.3 Energy Scale

We have seen in the previous sections that after performing the DA calibration, the agreement between the data and the MC simulation is of the order of 0.2%. Nevertheless the resolution of E_{DA} the energy derived by the DA method has not a completely symmetric shape and it is displaced from zero by 0.4%, as is it shown in Fig. 4.10(a). The long tail of the distribution in Fig. 4.10 (a) is due to showering [85] and due to final state radiation events, where the scattered electron radiates a photon, which deposits its energy indistinguishable in the same cluster as the electron.

The DA energy of the scattered electron relies directly on the measurement of the hadronic and electron scattering angles. The hadronical final state is constructed, combining the tracks

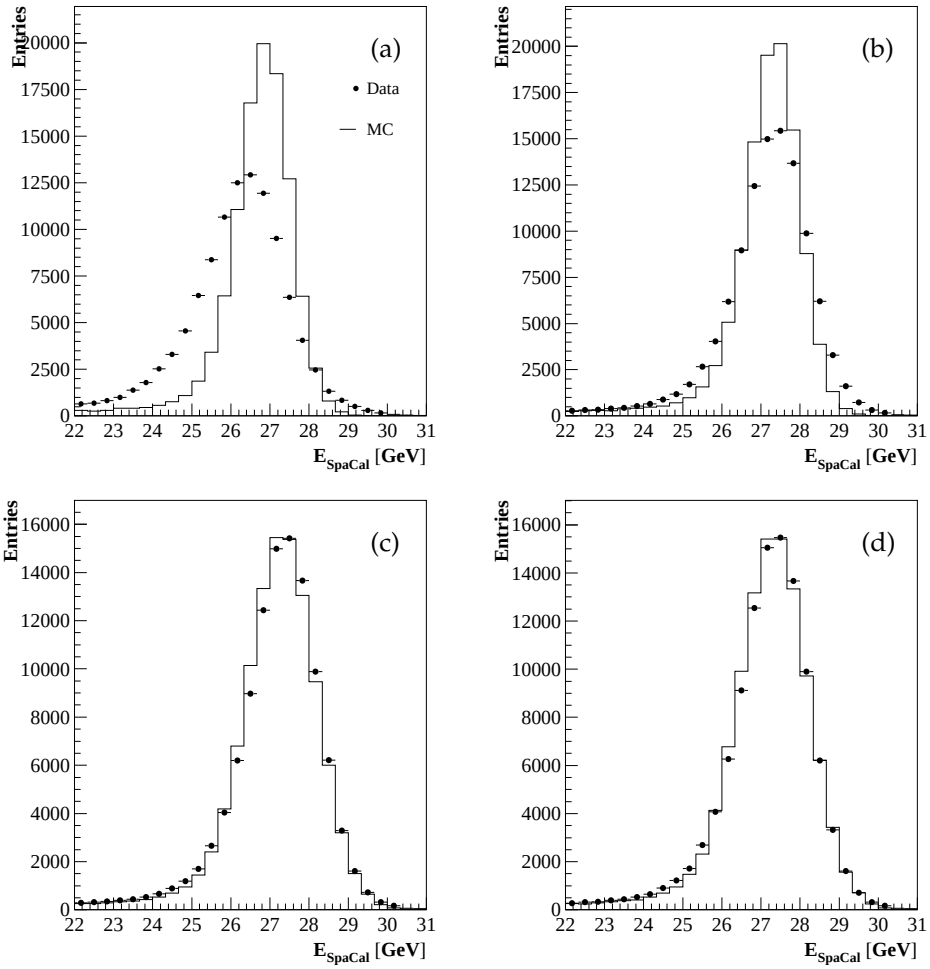

Figure 4.9: Comparison of data and MC of (a) uncalibrated (b) calibrated (c),(d) smeared energy distribution measured by SpaCal.

measured in the central tracking devices with the energy depositions measured by the LAr calorimeter and the SpaCal calorimeter. During the reconstruction, isolated energy depositions in the LAr are investigated in order to identify noise. The recognition of the LAr-noise is performed with different thresholds depending on the position of the energy cluster in the LAr calorimeter (see chapter 5 for more details).

Up to now the identified noise is not subtracted during the reconstruction of θ_{had}. However, this isolated energy deposition can influence the measurement of θ_{had} and therefore the DA energy could be affected. While the resolution of the DA energy is nearly independent of the subtraction of noise in the θ_{had} reconstruction, the mean value decreases considerably and tends to be zero (see Fig. 4.10(b)). The whole calibration procedure is therefore repeated, subtracting the identified noise during the reconstruction of the hadronical angle θ_{had}. The gain calibration

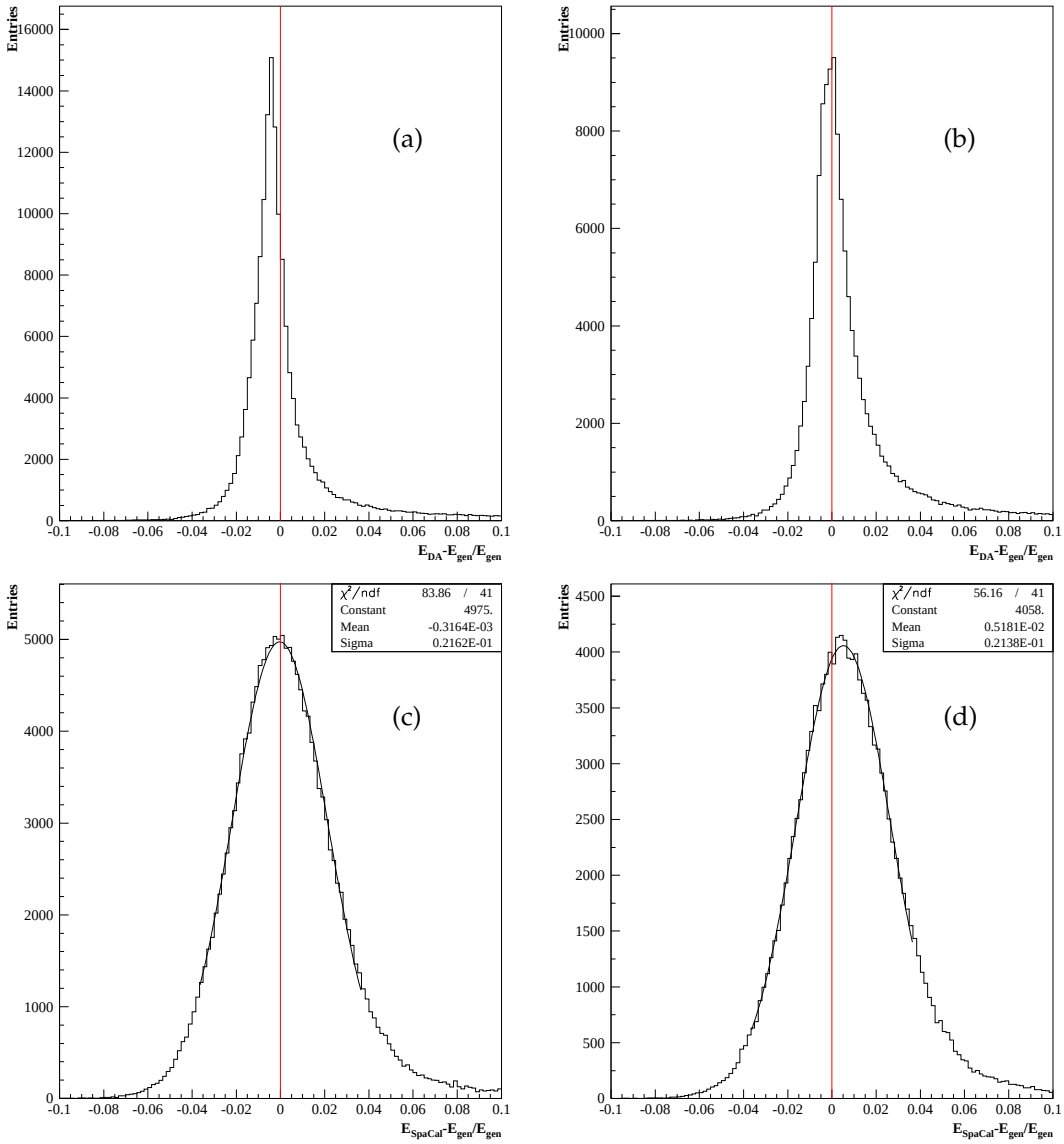

Figure 4.10: Resolution of the DA energy measurement in case the noise is not subtracted (a) and subtracted (b) during the reconstruction of θ_{had}. In figure (c) and (d) is shown the resolution of the SpaCal measurement after applying the DA calibration, in the case θ_{had} is reconstructed not subtracting (c) and subtracting (d) the LAr noise.

factors differ up to 0.5%, while the inbox, cracks, radial corrections stay in the same order.

In order to determine which calibration procedure should be applied during the analysis, the scale of the energy measurement at the kinematic peak for both calibration setups will be compared. Therefore the comparison between the SpaCal calibrated energy and the generated energy is necessary. This comparison is shown in Fig. 4.10 for both calibration schemes. In case the noise is subtracted, the scale of the SpaCal measurement is 0.5% while in case the noise is

not subtracted, the calibrated SpaCal measurement coincides with the generated quantity as it is shown by the lines in Fig. 4.10(c) and (d).

Since the aim of the calibration procedure is to have a SpaCal energy measurement close to the generated energy, the calibration scheme not subtracting the noise is chosen. In such way displacements of the SpaCal energy in the kinematic peak from the generated energy are avoided.

4.4 Cross check with the Hottest cell calibration

The hottest cell calibration method uses as well the kinematic peak region to derive individual cell calibration factors. In contrast to the DA method, the SpaCal measurement of the electron cluster is directly compared with the MC simulation [88].

In order to have an electron energy distribution with a Gaussian shape almost free of tails, the calibration sample uses the following selection:

- Events in which the electron cluster has a energy between 20 and 30 GeV and a cluster radius less than 4 cm.
- Radiative events are suppressed allowing a maximum value of y of 0.05.
- The noise contribution is suppressed applying $y > 0.005$.

The calibration gain factors are derived as:

$$g_i = \frac{< E_{cl,i}^{MC} >}{E_{cl,i}^{data}} \tag{4.5}$$

where $< E_{cl,i} >$ is the mean of the electron cluster energy, which is assigned to the hottest cell i. The statistics of the sample decreases considerably with increasing distances from the beam pipe and thus individual calibration factors can be determined only for the inner cells.

Since in the last sections data and MC were calibrated with the DA method, the hottest cell calibration selection is used only to cross check the DA calibration in a slightly different kinematic region where the effect of the tails due to radiative events is reduced.

In Fig. 4.11 the **DA calibrated** cell distributions for the hottest cell calibration selection are shown. There is no significant *shift* between data and MC for almost all cells. However, this

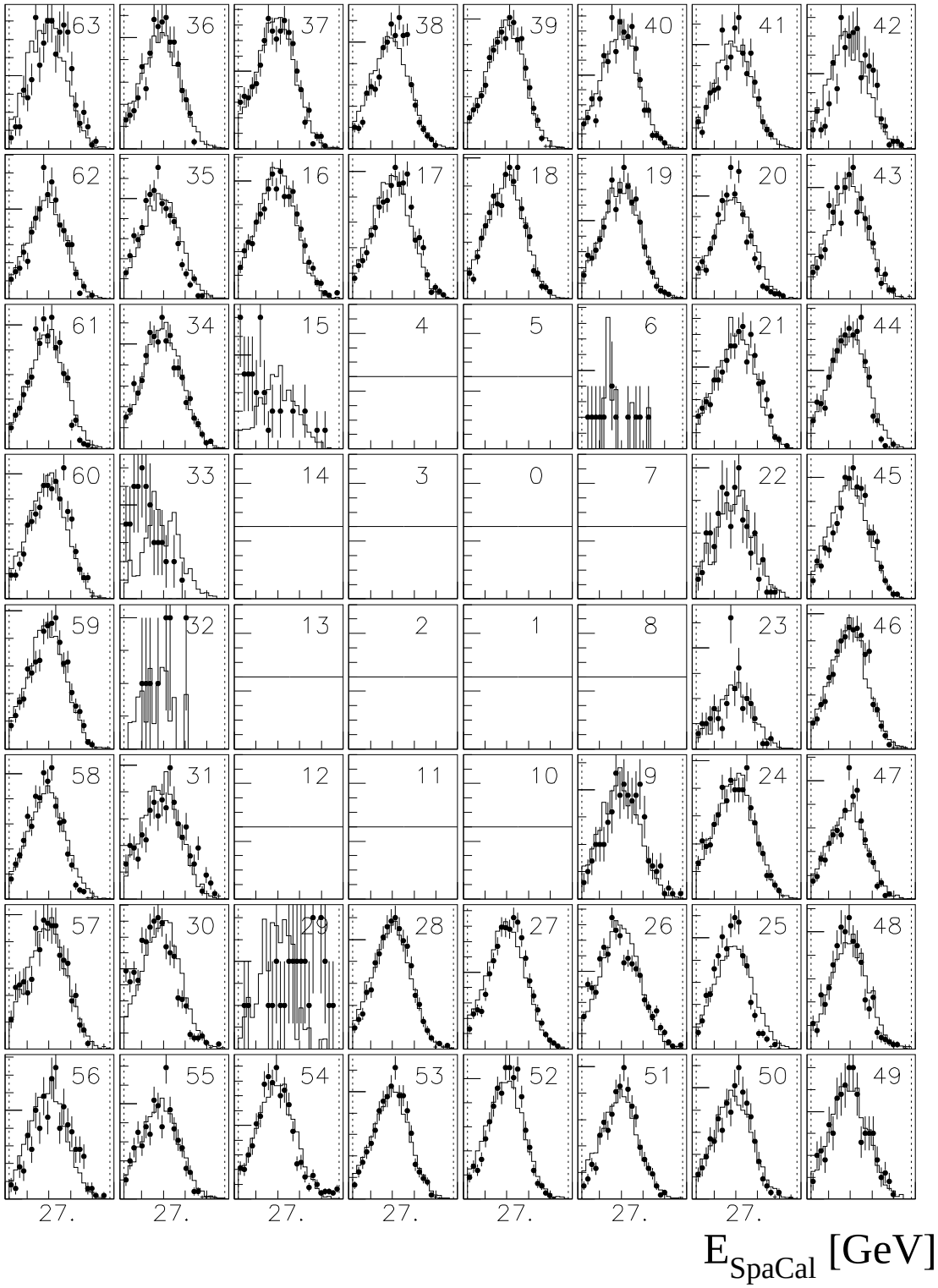

Figure 4.11: Calibrated energy distributions of the inner cells of the SpaCal calorimeter for the hottest cell calibration selection. Full points represent the data of the shifted vertex period, while the histogram illustrates the MC DJANGOH.

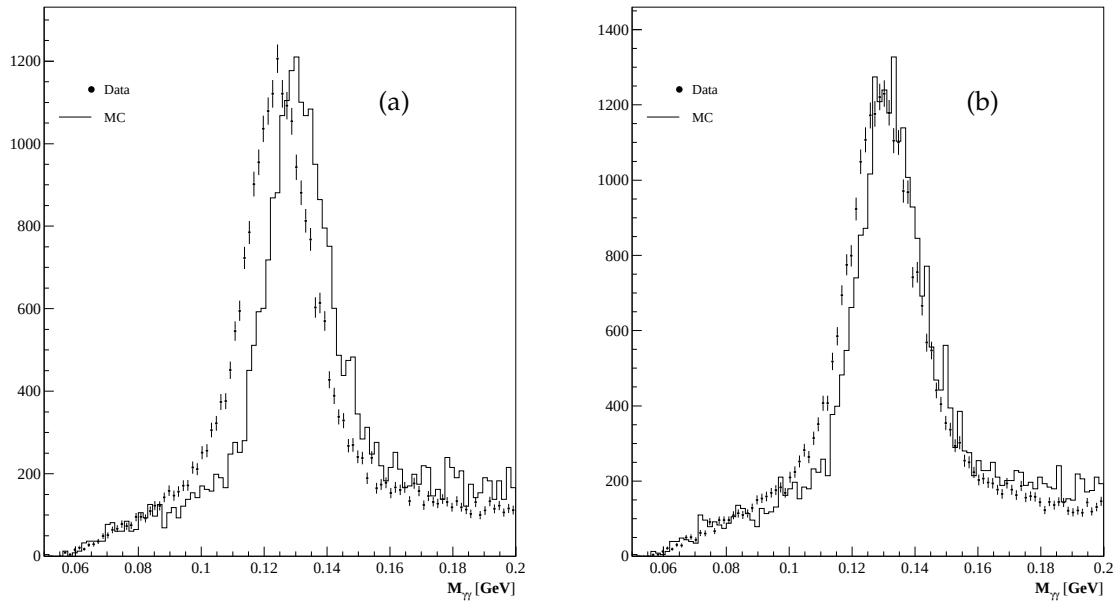

Figure 4.12: Invariant mass of π^0 invariant mass for energy clusters measured by SpaCal before (a) and (b) after applying the DA calibration.

selection allows us to identify which cells have to be rejected from the analysis due to their bad shape distribution. This correspond to the insert cells denoted by the numbers $15, 6, 9, 12$ and the cells 31 and 29.

4.5 Energy measurement at low Energies

As was shown in the previous sections, the DA calibration is performed with electron clusters where the energy lies in the kinematical peak region. A comparison between the data and the MC simulation shows that the energy measurement has a scale uncertainty of 0.2% in kinematic peak. If the DA calibration derived in the last sections is also valid for lower energies, then it is necessary to known what is its uncertainty.

One method used to study the scale of the energy measurement of the SpaCal calorimeter towards lower energies, uses the reconstruction of the invariant mass of $\pi^0 \to \gamma\gamma$ decays. The invariant mass is calculated according to:

$$m_{\pi^0} = \sqrt{2E_{\gamma 1}E_{\gamma 2}(1 - \cos\theta_{\gamma\gamma})} \tag{4.6}$$

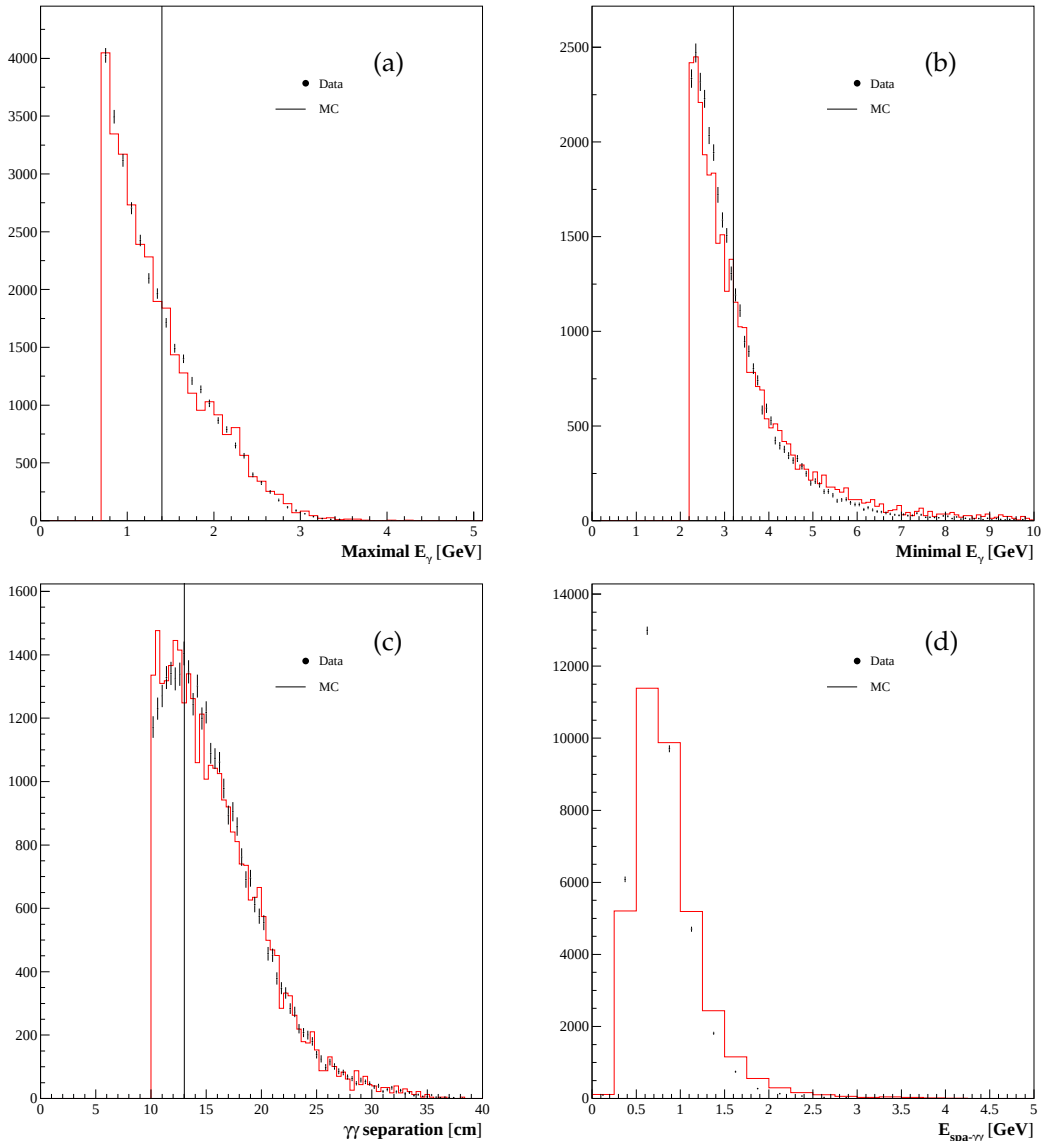

Figure 4.13: Control distributions of the π^0 invariant mass sample. The (a) maximal (b) minimal energy of the photons measured by the SpaCal calorimeter. (c) The separation between the cluster on the SpaCal plane (d) the energy sum of the two photon cluster.

where $E_{\gamma 1}$ and $E_{\gamma 2}$ are the energies of the photons, which can be measured by the SpaCal calorimeter, and $\theta_{\gamma\gamma}$ is the opening angle between the two photons. In order to suppress background from random coincidences in the π^0 mass reconstruction sample, the following selection cuts were applied:

- Events having only two clusters in the SpaCal calorimeter and triggered by S9 are used (see section 6.2). Since the threshold of S9 is 2 GeV, the clusters must have a minimum

energy of 2 GeV (see section 6.2).

- In order to measure a precise separation angle, only events having a well reconstructed vertex around 30 cm of the expected position at $z = 70$ cm are used.
- A cut of a minimum distance of 10 cm between the clusters is required to avoid overlap between the selected clusters

In Fig. 4.12 the reconstructed mass of the π^0 decays is shown for data and DJANGOH MC before and after the DA calibration is applied. The introduction of the DA SpaCal calibration, decreases the observed shift of the mass reconstructed distribution by almost 0.5%. However a shift between the data and the MC simulation is still observed. The value of this displacement determines the scale of the energy measurement at the π^0 mass. The shift is studied using the Kolmogorov-Smirnov (KS-test). The invariant mass distribution of the π^0 of the MC is shifted until the KS-test between the shifted-MC invariant mass and the data shows the maximum probability.

In order to study the dependence of the scale on the different variables used to reconstruct the invariant mass, the entire π^0 sample is divided into sub-samples with approximately equal statistic. Fig. 4.13(a) and (b) shows the comparison between data and MC of the maximal, minimal energy of the photon clusters, while in Fig 4.13(c) the separation distance between the two cluster on the SpaCal plane is shown. The lines represent the imposed cut used to define the subsamples. For each subsample, the shift between data and MC of the invariant mass using the KS-test is studied.

In Fig. 4.14(a) is shown the result of the KS-test for the invariant-mass subsamples, a shift of 2.5% is necessary to fit the MC with the data. Correcting the MC for the scale value of 2.5%, the agreement between the two invariant mass distributions considerably improves (see Fig 4.14(b)).

In order to determine the error of the scale, several checks to the π^0 invariant mass selection are performed. Fig. 4.13(d) shows the sum of the energy of the two photon clusters of the π^0 candidate. One observes that the data distribution is not completely described by the MC, therefore the energy distribution of the data of Fig. 4.13(d) was used to weight the MC. The weighted distributions of the MC were used to derive again the energy scale. The resulting scale have values which does not exceed 1% of the ones shown in Fig. 4.14(a). The error of the scale is thus quoted to be 1%.

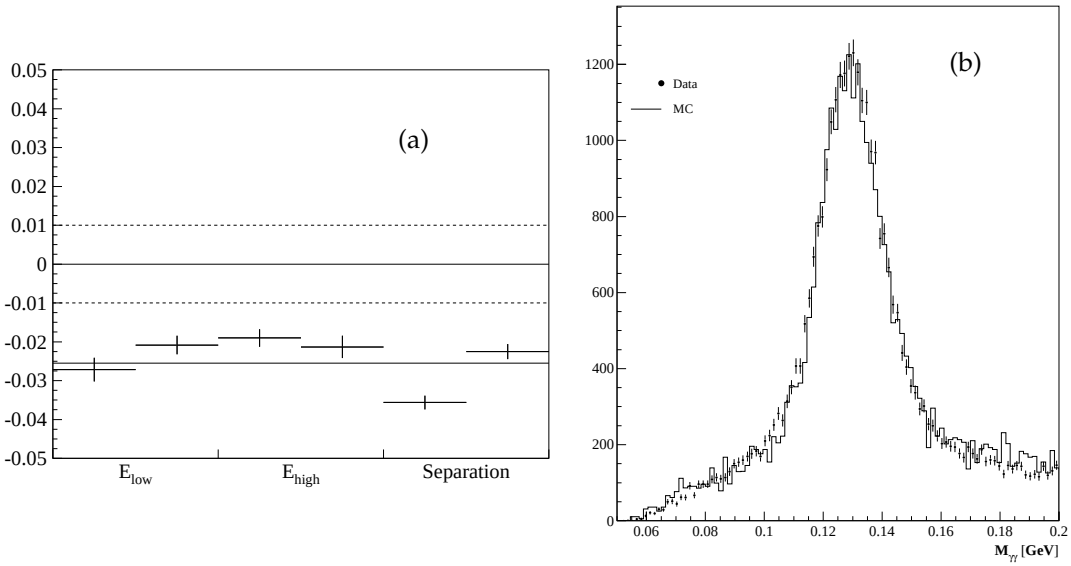

Figure 4.14: (a) Scale of the energy measurement using the π^0 sample. (b) Reconstruction of the $\pi^0 \rightarrow \gamma\gamma$ invariant mass for energy clusters measured with the SpaCal calorimeter after applying the DA calibration and correcting the scale.

4.6 Energy measurement Uncertainty

The differences of the energy scale at low energies $E \approx 2\,\text{GeV}$ and at kinematic peak $E \approx 27.5\,\text{GeV}$ correspond to the non linearity behaviour of the SpaCal energy response, previously studied in [102]. The energy measurement of the data will be corrected assuming that the energy scale is linear. The scale at kinematic peak and at π^0 mass ($E \approx 2\,\text{GeV}$) are used to derive the linear correction. QED Compton events were used in [106, 102] to check the calorimeter energy scale in the range $4 - 24\,\text{GeV}$, the linear energy correction derived in this analysis is in agreement with those results performed for different data sample periods.

The correction and the uncertainty of the scale of the SpaCal energy measurement is given by:

- $0\% \pm 0.2\%$ for E$= 27.5\,\text{GeV}$
- $2.5\% \pm 1\%$ for π^0 Energy (E$= 2\,\text{GeV}$)

The uncertainty of the energy measurement will be used to derive the systematic uncertainty of the F_2 measurement.

Chapter 5

Hadronic Final State

The calibration of the LAr calorimeter and the understanding of the hadronic final state (HFS) requires special attention for the $x \geq 10^{-4}$ region, where the electron method begins to be less accurate and the kinematical variables can be better reconstructed with the Σ method. Thus, for values of $x \approx 10^{-4}$, the measurement of the inclusive DIS cross section depends not only on the reconstruction of the scattered electron but also depends on the reconstruction of the HFS.

In order to reconstruct as good as possible the kinematical variables x and Q^2 with the Σ method, detailed studies on the energy flow of the HFS have to be performed. This studies essentially involve the calibration of the main calorimeters of the H1 detector. The calibration is performed using the longitudinal and the transverse momentum of the particles which form the initial and the final state. Measuring with a perfect detector, energy and momentum conservation requires that the total $(E - p_z)_{tot}$ and $p_{t,tot}$ of the scattered electron and of the HFS be equal to:

$$(E - p_z)_{tot} = 2E_{inc} \approx 55\,GeV \qquad \vec{p}_{t,tot} = \vec{p}_t^{\,el} + \vec{p}_t^{\,had} = 0 \tag{5.1}$$

However, real experiments suffer from acceptance losses and resolution effects which lead to deviations of the expected values. In this chapter the HFS is studied in detail using the global quantities written in Eq. 5.1 and those already discussed in section 3.3.2 and 3.3.3.

In section 5.1 the response of the SpaCal calorimeter to hadrons is studied using the longitudinal energy conservation $(E - p_z)_{tot} \approx 55\,\text{GeV}$. The reconstruction of the HFS is explained in section 5.2. The calibration of the LAr calorimeter is described in section 5.3, where the transverse momentum of the electron is used as the energy scale reference. Part of the energy measured in the LAr calorimeter is influenced by noise signals originating either from the elec-

SpaCal Calibration factor for hadrons		
Reference	Electromagnetic section	Hadronic section
[87]	1.1	1.3
[89, 88]	1.5	1.5
[88]	1.07	1.07

Table 5.1: Calibration constants for the hadronic response of the SpaCal calorimeter.

tronics of the LAr calorimeter readout or it is beam induced. Additional noise due to secondary scattering of final state particles which deposit its energy into the calorimeter can influence the energy measurement. The influence of the noise on the kinematic reconstruction is explained in section 5.4. At the end of the chapter the uncertainties assigned to the description of the HFS are summarized.

5.1 Hadronic SpaCal

The hadronic section of the SpaCal calorimeter is non-compensating, thus its response is different for hadronic and electromagnetic showers. The combined response of the SpaCal calorimeter for hadrons was investigated in [86] using data taken at the CERN proton Synchroton. Two parts of the electromagnetic and hadronic sections of the SpaCal where installed at the CERN PS T9 beam line, where electrons and π^- having incident energies between 1 and 7 GeV were used to investigate the hadronic response and the e/π separation.

The combined response of the SpaCal to hadrons was studied using π^-, the energy measurement in the electromagnetic and hadronic section were added in case the π^- interacted at least in one of the two sections of the SpaCal. An optimal constant scale factor 1.94 was found for the electromagnetic section while for the hadronic section the calibration factor varies from 1.29 at 3 GeV to 1.46 at 7 GeV [86].

The hadronic energy corrections for the SpaCal calorimeter were also estimated in a Monte Carlo study obtaining values of 1.1 for the electromagnetic part and 1.3 for the hadronic part [87]. These corrections were applied for both data and MC for all cells which do not belong to the electron cluster.

Using *ep* collisions the longitudinal energy conservation was used in several analyses in order to study the response to hadrons using the SpaCal. Such investigations exploited the combined energy measurement in the electromagnetic and hadronic section of the SpaCal, obtaining calibration factors which are summarized in table 5.1. The product of the correction factors repre-

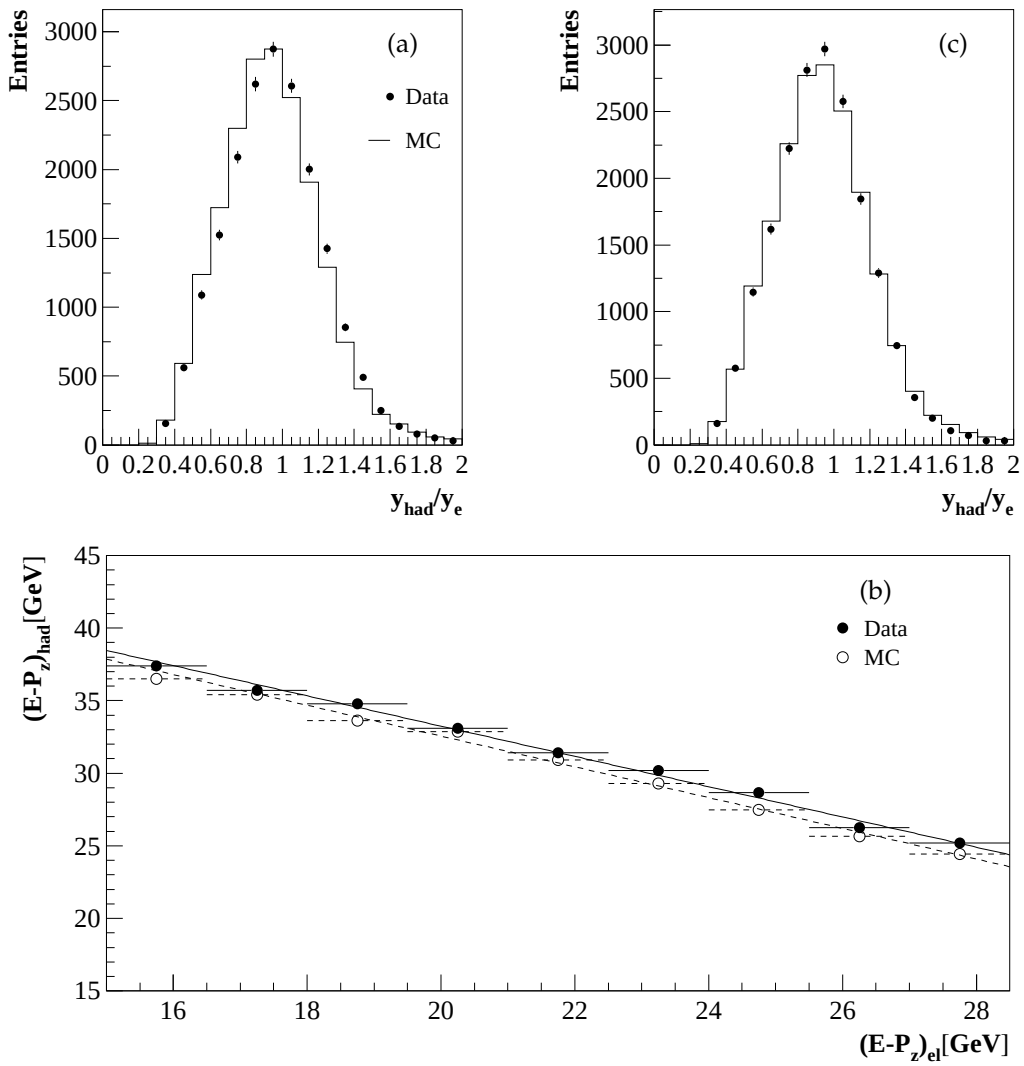

Figure 5.1: Comparison between y_{had}/y_e for events with $y_e > 0.5$ and $(E - p_z)_{tot} > 35\,\text{GeV}$ using the initial hadronic scale. (b) Mean value of $(E - p_z)_{had}$ of the hadrons with the $(E - p_z)_{el}$ of the electron for events having $y_e > 0.5$ and $(E - p_z)_{tot} > 35\,\text{GeV}$. (c) Comparison between y_{had}/y_e with the same selection of Fig.(a) but correcting the $(E - p_z)_{had}$ of the hadrons in the MC by 3% (see text).

sent the starting scale of the SpaCal hadronic energy in the data sample which is investigated here.

The energy scale of the hadronic section of the SpaCal can be studied with DIS events [90]. For high values of y, the hadronic final state is scattered mainly in the backward region of the H1 detector, thus the measurement of the HFS for high values of y is mainly performed by the SpaCal calorimeter. Therefore in that region, the energy of the scattered electron can be used as

the reference scale to study the hadronic energy scale. The inelasticity variable y reconstructed with the electron y_e (see equation 3.1) and the hadron y_{had} (see equation 3.6) method are the variables used to study the scale.

Since for high values of $y > 0.5$ the photoproduction background contributes strongly (see Fig. 3.9(d)),hence only events having a $(E - p_z)_{tot} > 35\,\text{GeV}$ are selected to study the hadronic energy scale of the SpaCal calorimeter. In Fig 5.1(a) the ratio y_{had}/y_e is shown for events where $y_e > 0.5$ and $(E - p_z)_{tot} > 35\,\text{GeV}$. A clear shift between the data and the MC is observed.

The energy shift is studied analyzing the behaviour of the measured $(E - p_z)_{had}$ from the hadrons taking as reference the $(E - p_z)_{el}$ of the scattered electron. Due to longitudinal energy conservation the total $(E - p_z)_{tot}$ has to be conserved and equal to 55 GeV. Thus in average the $(E - p_z)_{had}$ with the $(E - p_z)_{el}$ of the electron should be directly correlated. In Fig. 5.1(b) is shown the dependence of the $(E - p_z)_{had}$ with $(E - p_z)_{el}$ for data and MC. The deviation between data and MC reflect the shift observed in the y_{had}/y_e distribution. The shift can be obtained using the ratio or the difference between the data and the MC points shown in Fig. 5.1(b).

The $(E - p_z)_{had}$ of the hadrons in the MC had to be corrected with a factor 0.97 (3%). This correction correspond to a shift of 700 MeV. In Fig. 5.1(c) is shown the y_{had}/y_e distribution after applying the correction leading to a good agreement. The uncertainty of the hadronic SpaCal is quoted as half of the needed correction which is 350 MeV.

5.2 Reconstruction of the Hadronic final State

In contrast to the identification of the scattered electron, the identification of the hadronic final state (HFS) is even more complex, since the HFS can have different topologies inside the H1 detector depending on which values of Q^2 and x the DIS event occur. This involves several energy depositions which can be measured using the subdetector components of the H1 detector. The aim of the reconstruction of the HFS is to provide a four vector which contains all measured energy depositions.

The reconstruction of the particles belonging to the HFS rely basically on the momentum measurement of the central tracking devices, the energy deposition in the LAr calorimeter cells and the energy deposition in the cells belonging to the hadronic activity in the SpaCal calorimeter. The HFS is reconstructed with the elaborated algorithm FSCOMB [92, 94, 95], which combines the measurements of the subdector components previously mentioned.

In order to improve the kinematic reconstruction, the FSCOMB algorithm optimizes the momentum measurement according to the resolution of the subdetector components. For example for low energetic particles the central tracking devices are used, since their resolution is propotional to the energy E of the particle, whereas the calorimeter resolution is $50\%/\sqrt{E}$ leading to better performance at high energies.

Using the measured hits in the tracking devices, the curvature κ and the spacial position of the track is determined. The information of each track is used to determine the vertex position of the event. Thus, using the vertex and the track parameters a four momentum P^{Track} of all measured tracks by the tracker devices is constructed. In the same way, the four momentum P^{LAr} and P^{HadSpa} is constructed using the vertex position and the spacial coordinates of the cells where energy was deposited.

FSCOMB combines the calorimeter and the track information in the following way. Tracks with momenta less than 2 GeV are selected and extrapolated to the LAr surface where they are linked to clusters. The extrapolated track with the calorimeter cluster is linked, under the assumption that the particle yielding the track is a pion [92, 93]. All clusters inside a cylinder with a radius of 20 cm in the electromagnetic section and 40 cm in the hadronic section of the LAr are considered. A track is also used if its extrapolation does not reach the LAr surface. In order to avoid double counting of the measured four momentum, those calorimeter cells, where the energy deposition is replaced by the track measurement, are masked and are not used to build the LAr four momentum P^{LAr}. In general the four momentum of the hadronic final state can be expressed as the following vectorial sum:

$$\vec{P}^{had} = \vec{P}^{Track} + \vec{P}^{LAr} + \vec{P}^{HadSpa} \tag{5.2}$$

The combination of the track with the calorimeter measurement uses primary vertex constrained tracks. In the course of this analysis it was found that the vertex position determined by the central tracking devices and the BST differ considerably in case the tracks reconstructed by forward trackers are used to determine the vertex position. Thus, the link of tracks and calorimeter four momentum is performed using the primary vertex only in case reconstructed tracks by the CJC are found. In case no tracks are in the CJC found, then the default vertex position $z = 70$ cm is used. At analysis level the four momentum is again calculated using the vertex position of the BST.

The contribution of the four momentum of the SpaCal P^{HadSpa} contains the energy deposited in the electromagnetic section, which does not belong to the electron cluster and the energy which is deposited in the hadronic section.

For low values of y, the determination of $(E - p_z)_{had}$ is affected by extra activity in the calorimeter. The scattered electron can be rescattered off the detector material behind the central tracker with secondary particles. These particles can be wrongly identified as taking part of the HFS originating from the primary interaction. This extra activity is reduced by substracting 10% of the $(E - p_z)_{el}$ of the electron from the total hadronic contribution measured in the SpaCal, if the result is negative a zero contribution for the SpaCal is taken [89].

5.2.1 Noise identification using FSCOMB

During the reconstruction of the four momentum in the LAr, the FSCOMB algorithm also identifies noise. This is neccesary, since during the ep collision, the energy measured by the LAr calorimeter is overlayed with noise signals produced by example from the electronics of the LAr cells which allow to measure the energy depositions in the LAr [96]. Thus, not all measured energy in the LAr calorimeter belongs to the energy of the HFS of the ep collision. Therefore it is necessary to investigate the noise.

The strategy is to look for isolated energy depositions in the cells of the LAr, thus all cells which have an energy deposition are investigated. Two different energy thresholds depending on the angular position of the cell are considered.

The angular position of the cell θ_{cell} is measured with respect the origin of coordinate system of the H1 detector. In case a cell is localised at $\theta_{cell} < 15^\circ$ and its energy energy is below 800 MeV, the energy of the neighbouring cells localised in a transversal cone of 40 cm is summed. In case the summed energy of all neighbouring cells is also below 800 MeV, all those cells are masked as "noise-cells". Similarly a energy threshold of 400 MeV is used if the cell is localised at $\theta_{cell} > 15^\circ$, but the transversal extension of the neightbouring cells is only 20 cm. For $\theta_{cell} < 15^\circ$ the cell is located in the IF1, IF2 wheels (see Fig. 2.9).

Following this procedure, the four momentum measured by the LAr can be expressed as the sum of the identified Noise and the Signal:

$$\vec{P}^{LAr} = \vec{P}^{LAr}_{Signal} + \vec{P}^{LAr}_{Noise} \tag{5.3}$$

where P^{LAr}_{Noise} is constructed with the cells masked as noise-cells.

5.3 Calibration of the LAr calorimeter

In contrast to the electromagnetic SpaCal calibration the energy flow in LAr does usually not consist of a single cluster, but it is distributed over collimated jets or it is just dispersed into the H1 detector. Therefore it is very difficult to select single hadrons and use them to calibrate.

Since in neutral current DIS events, the transverse momentum of the electron p_t^{el} and of the hadronic final state $p_{t,had}$ have to be balanced, it is possible to use the well measured transverse momentum of the electron to achieve the calibration of the LAr calorimeter.

The trasversal balance of the event $p_{t,bal}$ defined as

$$p_{t,bal} = \frac{p_{t,had}}{p_t^{el}} \tag{5.4}$$

is the most used variable to derive the calibration of the LAr calorimeter. The transverse momentum of the total HFS $p_{t,had}$ is calculated using:

$$p_{t,had} = \sqrt{(\sum_h p_{x,h})^2 + (\sum_h p_{y,h})^2}$$

where the contributions of the LAr signal, tracks and hadrons measured in the SpaCal are considered in the vectorial sum of $p_{x,h}$ and $p_{y,h}$:

$$p_{x,h} = p_{x,Signal}^{LAr} + p_x^{Track} + p_x^{HadSpa}$$
$$p_{y,h} = p_{y,Signal}^{LAr} + p_y^{Track} + p_y^{HadSpa}$$

5.3.1 Calibration procedure

In this analysis the Lagrangian method introduced in [90] is used to derive the calibration constants of the LAr calorimeter. The Lagrangian method minimizes the difference between the transverse momenta of the scattered electron and of the hadronic final state particles. The

function used has the form:

$$L = \sum_{i=1}^{N_{events}} \frac{1}{\sigma_i^2} \left(p_{t,i}^{el} - \left[p_{t,i}^{Track} + p_{t,i}^{HadSpa} + p_{t,i,LAr}^{Noise} \right] - \sum_{j=1}^{M=120} \alpha_j p_{t,i,LAr}^{j} \right)^2 \tag{5.5}$$

where p_t^{el} is the transverse momentum of the electron, measured in the electromagnetic section of the SpaCal calorimeter. The variable σ_i is the weight of each event, which is taken as 1 in the following calculation.

p_t^{Track} and p_t^{HadSpa} are the transverse momenta of the hadrons measured with the central tracking devices and with the SpaCal calorimeter, respectively.

The contribution of the LAr is considered by the last term in Eq.5.5, where the index j corresponds to a continues number asigned to the different wheels and octants of the LAr calorimeter. Since the LAr calorimeter is build of 8 wheels subdivided in 8 octants and 7 wheels have one electromagnetic and one hadronic section, in total $M = 7 * 8 * 2 + 8 = 120$ contributions of the transverse impulse of the LAr $p_{t,LAr}$ are considered. The variable α_j are the calibration constants to be determined by minimizing the function L.

The term p_t^{Noise} in Eq. 5.5 represents the transverse momentum of the cells which are identified by the FSCOMB algorithm as noise. This noise can be substracted globally from the LAr contribution or for each module.

The mimimization procedure is performed such that the transverse momentum of the hadrons is projected onto the electron direction, in such way only the p_t component parallel (or antiparallel) to the p_t^{el} is considered. The minimization requirement

$$\frac{\partial L}{\partial \alpha_j} = 0 \tag{5.6}$$

defines a system of M equations corresponding to the M considered modules and octants:

$$\sum_{i=1}^{N_{events}} p_{t,LAr}^{i,k} \cdot \left(p_t^{el} - \left[p_t^{Track} + p_t^{HadSpa} - p_{t,LAr}^{Noise} \right] - \alpha_K \sum_{j=1}^{M} p_{t,LAr}^{i,j} \right) = 0 \tag{5.7}$$

The results of the minimization determine the energy scale factors α_k for the $M = 120$ modules and octants of the LAr calorimeter. The solution of Eq. 5.7 is obtained using numerical matrix techniques.

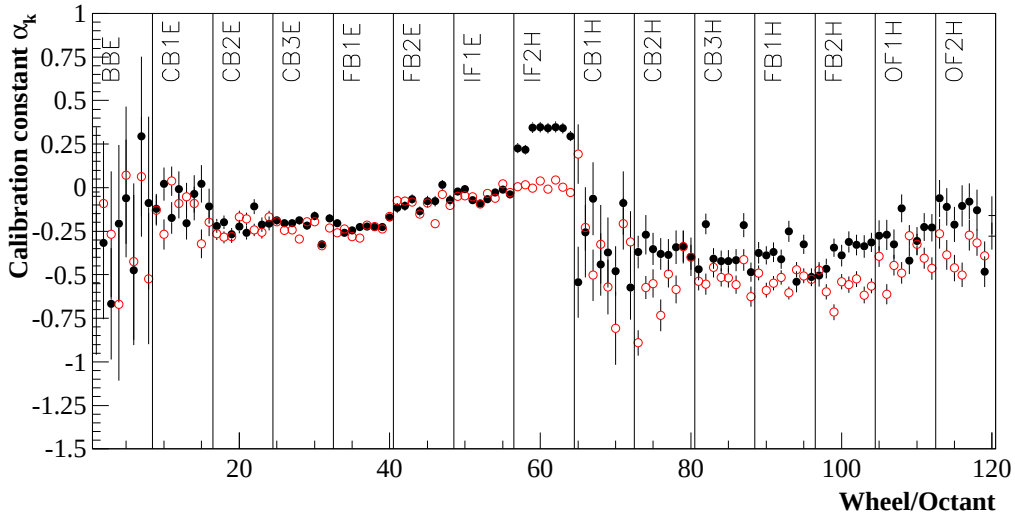

Figure 5.2: Calibration constants for the LAr calorimeter for data of the Shifted vertex period (closed points) and DJANGOH MC (open points). Each wheel is labelled according its position with respect the nominal interaction point (central (CB), forward (IF,OF), Backward (B) see also Fig. 2.9). The lines indicate the octants of the corresponding wheels of the LAr calorimeter.

Since the Lagrangian method relies on the balance of the transverse momentum of the electron and the hadrons to derive the calibration constants of the LAr calorimeter modules, it is important to consider a **calibration sample** almost free of background events.

A precise determination of p_t^{el} is ensured by requiring a BST track validation of the electron candidate cluster. Photoproduction background is considerably reduced by requiring the energy of the scattered electron to be $E_e > 20\,\text{GeV}$ (see Fig. 3.9(b)).

In addition, the calibration sample uses events where the hadronic angle lies in the LAr acceptance. In order to suppress events where the hadronic final state escapes undetected through the beam pipe, the angular coverage is restricted to $15^\circ \leq \gamma_h \leq 150^\circ$. Furthermore the transverse momentum of the hadrons $p_{t,had}$ has to have at least 30% of the electron momentum. This cut also reduces the losses in the forward direction where $p_{t,had}$ tends to be zero.

In Fig. 5.2 are shown the calibration constants of the LAr calorimeter for data of the shifted vertex period and the signal MC DJANGOH. The calorimeter response is well described by the MC simulation only for the electromagnetic part, but differences are observed in the hadronic modules, specially for the forward module IF2.

The $p_{t,bal}$ distribution for the **calibration sample**, before and after the calibration constants are applied is shown in Fig. 5.3 (a) and (b), respectively. A good description between the data and

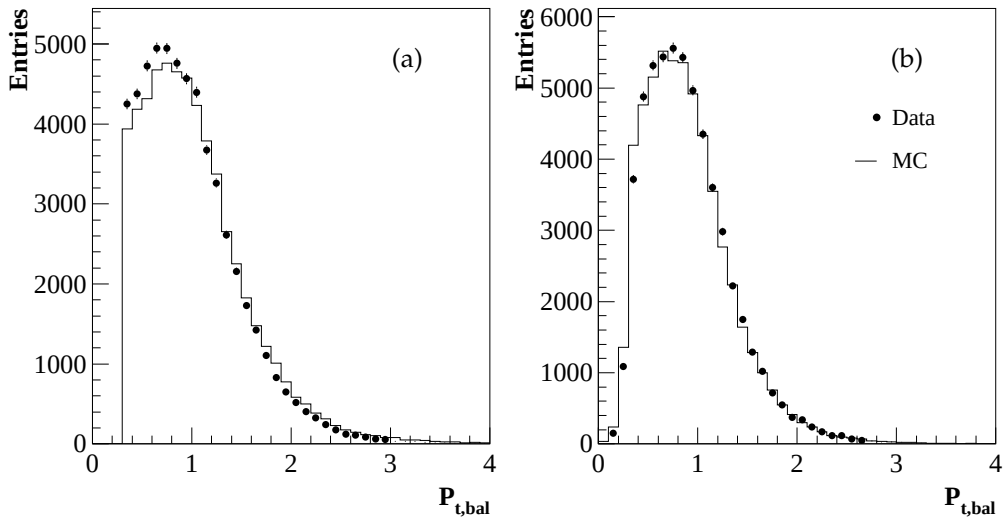

Figure 5.3: Distribution of $p_{t,bal}$ for the calibration sample before (a) and after (b) the calibration constants presented in Fig. 5.2 are applied.

the MC simulation is found after applying the calibration constants. Nevertheless, the mean of the distribution is not located at the expected value $p_{t,bal} = 1$. The values of $p_{t,bal}$ vary according to the phase space in which the event occur. Therefore the dependence of the $p_{t,bal}$ distribution on the angle of the hadrons and on the kinematic variables has to be studied in more detail for the final DIS analysis sample (for a detailed description of the DIS sample see table 6.1). This studies are presented in the next section.

5.3.2 Description of the HFS in the DIS analysis sample

As already mentioned at the beginnig of this chapter the HFS is a complex system. The $p_{t,bal}$ and the $(E - p_z)_{tot}$ distributions of the DIS sample are the unique quantities used to study the total energy flow of the HFS. On the one hand, the p_t of the hadrons should be balanced with the p_t^{el} of the electron, but on the other hand the event sample should also conserve its longitudinal energy.

In Fig. 5.4(a) and (c) are shown the $p_{t,bal}$ distributions for the whole DIS event selection before and after applying the calibration constants. An improvement of the description between the data and the MC is observed for the whole DIS sample. Apart from the normalization problem which will be discussed in the next chapter, a slight imbalance of the order of 3% is observed for values of $p_{t,bal} < 0.6$ (see Fig. 5.4(c)). The deviation between the data and the MC simulation is quantified by its ratio, which is shown in Fig. 5.4 (b) and (d).

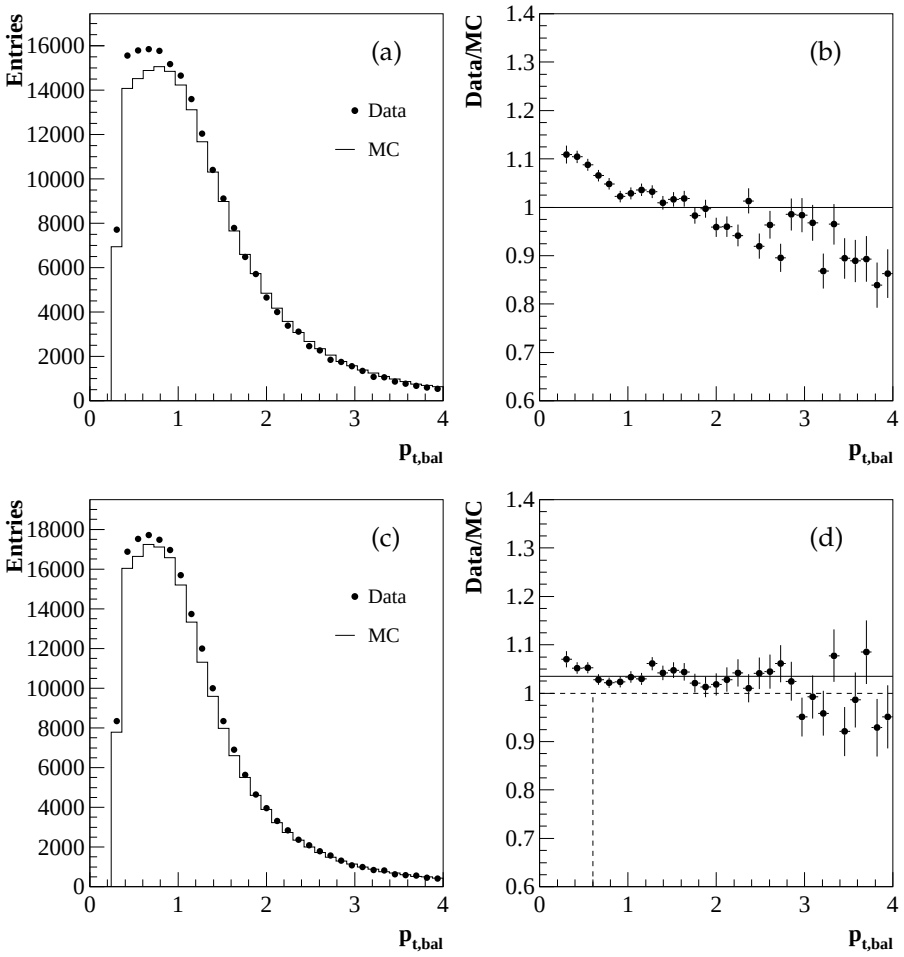

Figure 5.4: (a) Distribution of $p_{t,bal}$ for the whole DIS selection before applying the LAr calibration constants, (b) the ratio of data over MC for the uncalibrated $p_{t,bal}$ distribution. (c) Calibrated $p_{t,bal}$ distribution (d) ratio of data over MC for the calibrated $p_{t,bal}$ distribution.

As in the **calibration sample**, the $p_{t,bal}$ distribution is good described by the MC simulation, but it does not peak at the expected value 1. In order to investigate how the balance of the transverse momentum is distributed over the accessed kinematical region, the dependence of $p_{t,bal}$ on the angle of the hadrons and on the kinematic variables is studied.

Using the transversal and longitudinal momentum of the HFS, the polar angle of the hadrons θ_{had} can be calculated (see Eq. 3.8). The polar angular dependence of the $p_{t,bal}$ distribution is shown in Fig. 5.5(a). The mean value of the $p_{t,bal}$ distribution deviates from 1 depending on which hadronic angle θ_{had} is accessed. For low and high values of θ_{had} the ratio deviates from 1 by 5%. This behaviour leads to a distribution of $p_{t,bal}$ with a mean value of 0.85. The deviation between the data and the MC is shown in Fig. 5.5(b), which does not exceed 2% for $\theta_{had} > 20^{\circ}$.

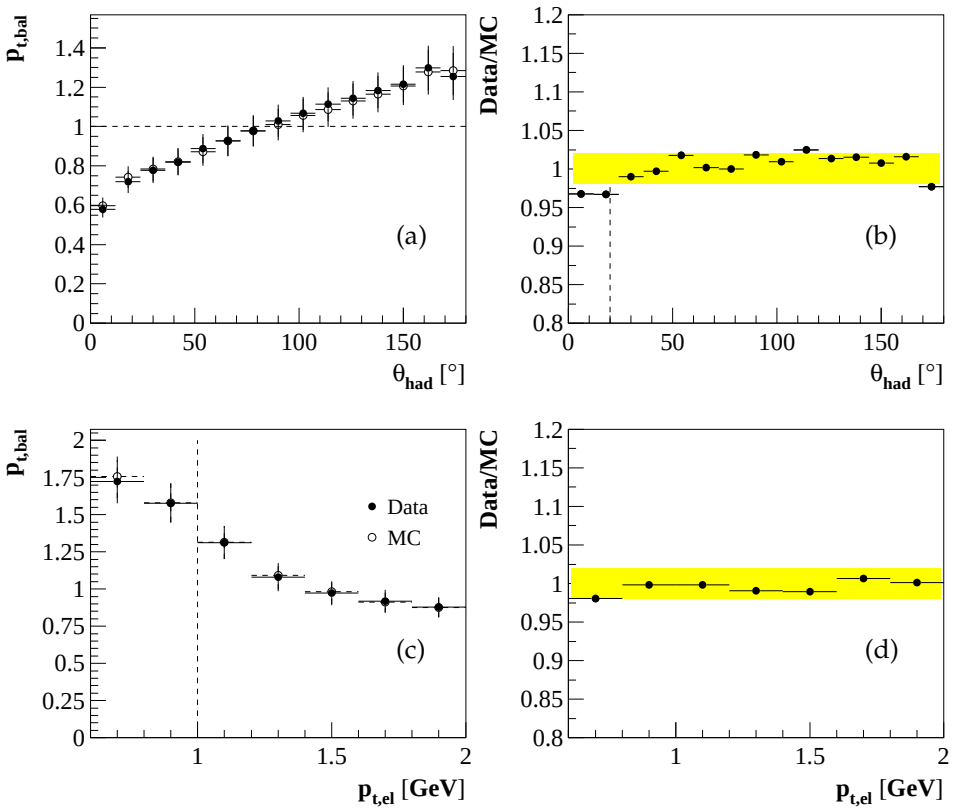

Figure 5.5: Comparison between data and MC for the $p_{t,bal}$ distribution as function of (a) the hadronic angle θ_{had}, (c) the transverse momentum of the electron $p_{t,el}$. The ratio of data over MC of Fig (a) and (c) are shown in Fig. (b) and (d). The ratio of data and MC has a drawn band corresponding to a deviation of 2%.

The dependence of $p_{t,bal}$ on the transversal momentum p_t^{el} of the electron is shown in Fig. 5.5(c). In this case, the difference between data and MC is concentrated at low values of p_t^{el}. The MC can describe the behaviour of the data even at low values of p_t^{el}. For values of $p_t^{el} > 1\,\text{GeV}$, the mean value of p_{tbal} approximates to 1. Hence the quality of the $p_{t,bal}$ reconstruction varies with the kinematical regions characterized by θ_{had} and p_t^{el}.

In order to investigate how the transverse energy flow is related with the longitudinal energy flow, the dependence of the $p_{t,bal}$ distribution for different values of y is analysed. In such way a "measure" of the transverse and longitudinal energy flow can be determined.

The kinematical variable y characterizes the fraction of the longitudinal energy that the HFS takes after the ep collision. For high values of y the HFS is located mainly in the backward region of the H1 detector, while for low values of y the HFS is scattered in the forward region of the H1 detector. Using this naive characteristic of y, one can understand that depending

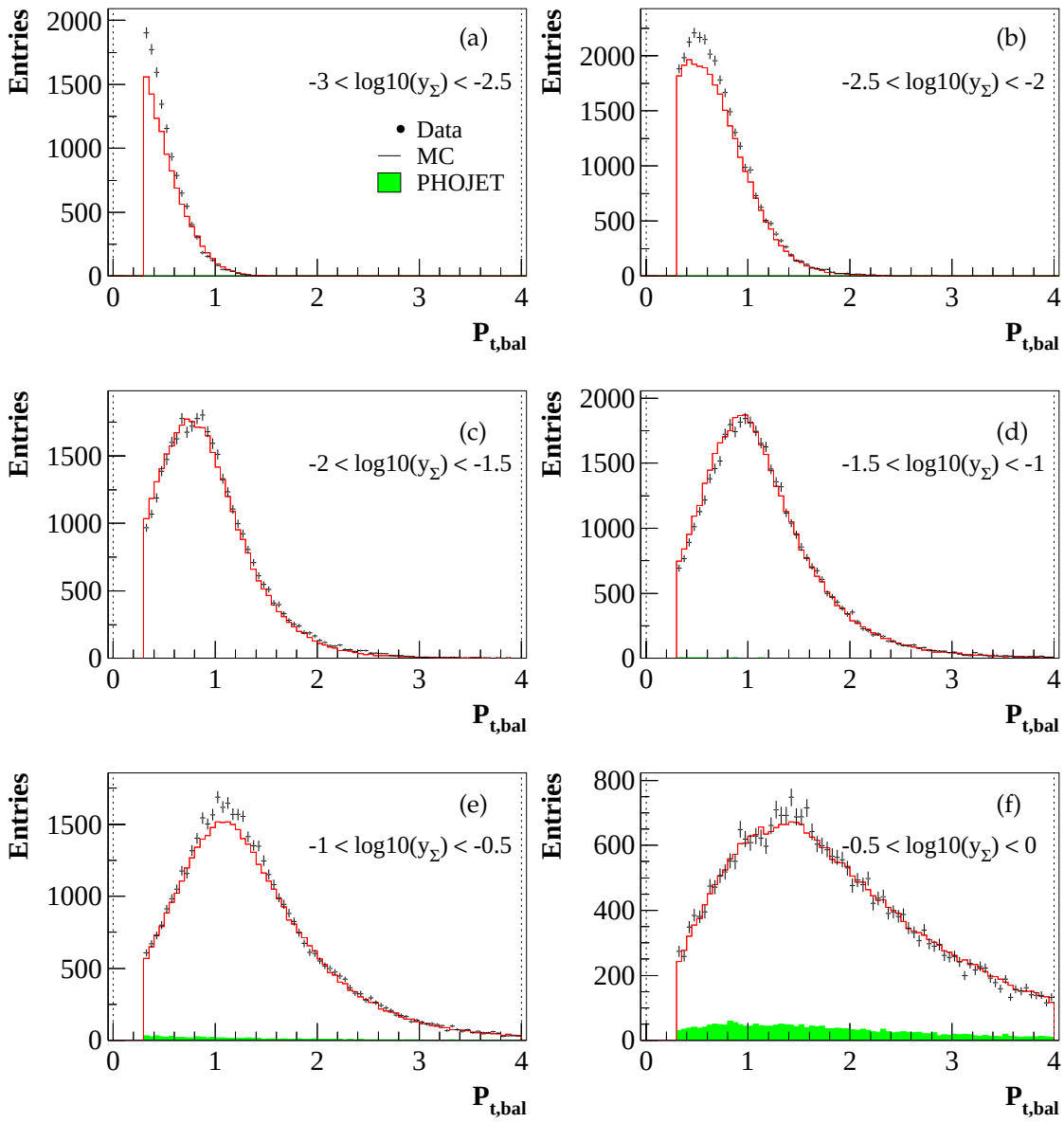

Figure 5.6: $p_{t,bal}$ distributions for different values of the inelasticity y_Σ. Closed points are data, while the histogram correspond to the sum of the DJANGOH and PHOJET MC. The γp background contribution is illustrated by the full area.

on which kinematical region the event occurs, the different subdetector components of the H1 detector play a relevant role.

For low values of y the transverse momentum of the hadrons tends to be reconstructed to lower values than the transverse momentum of the electron p_t^{el}. This can be seen in Fig. 5.6 where the $p_{t,bal}$ distribution is shown for different intervals of the inelasticity y_Σ. From Fig. 5.6(a) and

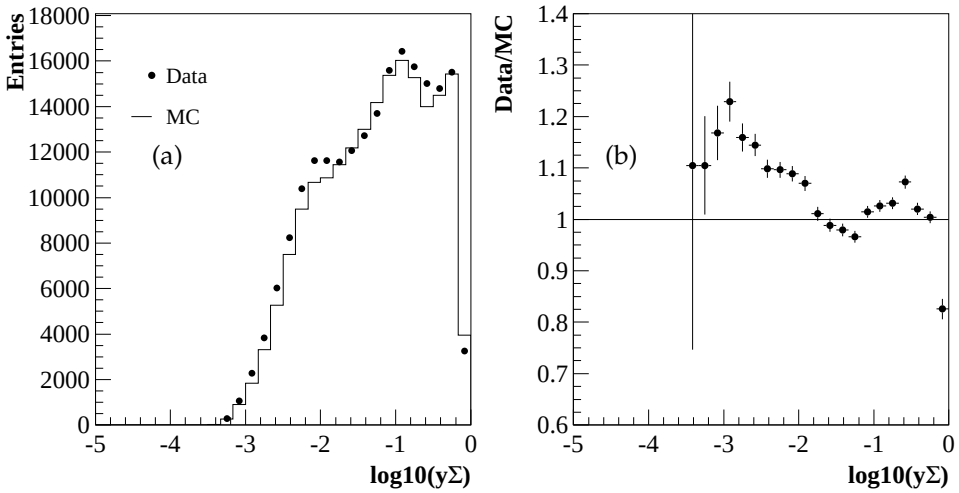

Figure 5.7: (a) The inelasticity variable y_Σ for the whole DIS sample,(b) the ratio of data over MC of y_Σ.

(b) follows that for low values of $y_\Sigma < 10^{-2}$, the $p_{t,bal}$ is lower than 1. The opposite behaviour is observed at $y > 10^{-1}$ where $p_{t,had}$ is reconstructed to higher values of p_t^{el} (see Fig. 5.6 (e) and (f)). Nevertheless for values of $y_\Sigma > 10^{-2}$ the balance between the electron and the hadrons is well described by the MC simulation, the difference between data and MC do not exceed 2% for this y_Σ region.

The $p_{t,bal}$ distribution is used to investigate the energy flow of the HFS in the transverse direction, and it is observed that for values of $y_\Sigma \geq 10^{-2}$ is good described by the MC simulation (see Figures 5.6(c) to 5.6(d)). However the kinematic variable y_Σ is not well described in the whole sample as can be seen from Fig. 5.7. The MC simulation can not reproduce the behaviour of the data for low values of y_Σ, spefically an excess is observed around $y_\Sigma \approx 10^{-2}$. Since y_Σ is one of the most important kinematical variables used to measure F_2, and $p_{t,bal}$ is used as a reference for the hadronic energy scale, the disagreement between data and MC for low values of y had to be investigated in more detail. The reason of the discrepancy might be related to an incomplete description of the physics which is implemented in the MC simulation. That would mean that the discrepancy comes from the proton structure function assumptions, or it might be that the discrepancy is a detector effect. In the following paragraphs this last option is investigated in detail.

The reconstruction of y with the hadron method allows to identify which subdetector component has the main impact in a specific kinematical region. The contribution of a subdetector component $i - had$ to the kinematical variable y_{had} is calculated through the fraction of the $(E - p_z)_{i-had}$ measured by the subdetector component $i - had$ to the total $(E - p_z)_{had}$ of the

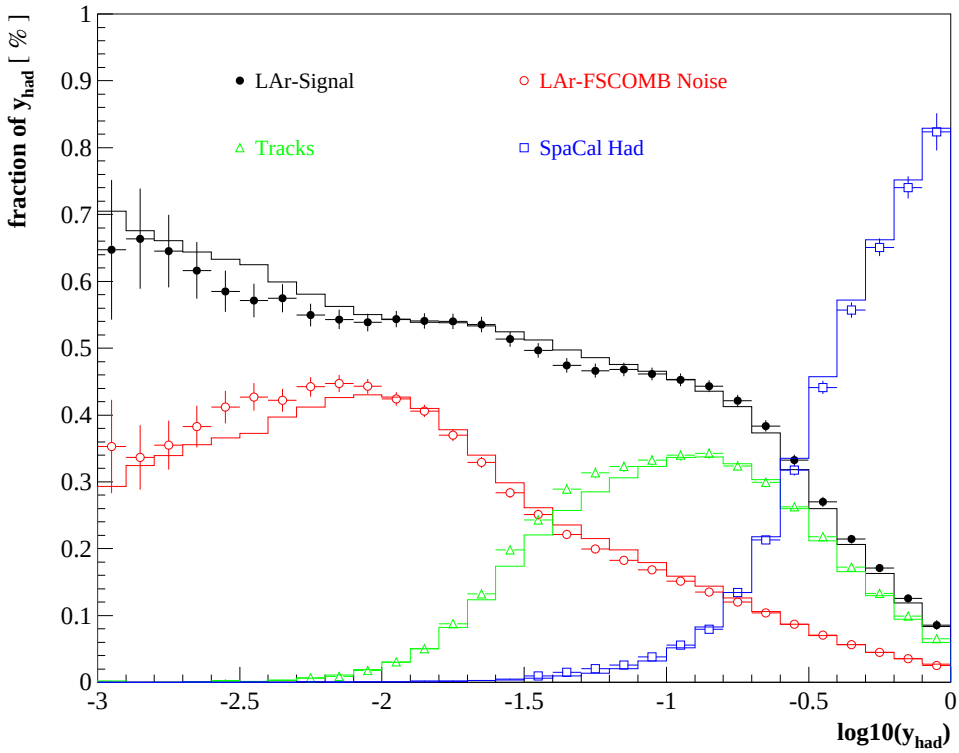

Figure 5.8: Contributions to y_{had} from the different detector components. The closed points represent the data while the histogram correspond to the MC simulation.

hadrons. For example, in order to calculate the fraction of y coming from the track measurement, each event is weighted with

$$f_y^{Track} = \frac{y_{Track}}{y_{had}} = \frac{(E - p_z)^{Track}}{(E - p_z)_{had}} \tag{5.8}$$

where

$$(E - p_z)_{had} = (E - p_z)_{LAr} + (E - p_z)_{Track} + (E - p_z)_{HadSpa} \tag{5.9}$$

$(E - p_z)_{had}$ considers the contributions from the LAr, tracks and the hadrons measured with the SpaCal calorimeter. The decomposition of y_{had} is shown in Fig. 5.8, where the whole measured energy is taken into account. At high y_{had} the contribution of the SpaCal calorimeter dominates, while the tracks contribute mainly at medium values of y_{had}. The LAr calorimeter contributes over the whole kinematic region, and the identified LAr-FSCOMB noise plays a ma-

jor role in the low y_{had} region. From Fig. 5.8 it is clear that in the region $y \approx 10^{-2}$, where the "$y_\Sigma-$bump" occurs (see Fig. 5.7(a)), the identified LAr-FSCOMB noise has a large influence on the reconstruction of the kinematics from the HFS.

In addition to the noise identification performed by the FSCOMB algorithm there are several noise suppression mechanisms implemented in the reconstruction of the energy measured by the LAr calorimeter. The first noise rejection is performed during the recording of raw data. Further noise suppression are done by the algorithms which merge the energy deposition into clusters [97, 98].

In order to study the influence of the noise in the DIS selection, different MC simulations were performed varying the noise input. The procedure used to include the noise in the MC simulation of the H1 calorimeter and how the noise is treated during the reconstruction is explained in the next section.

5.4 LAr Noise

5.4.1 Noise in the MC simulation

The energy deposited in the LAr calorimeter is overlayed with noise signals. Basically, two contributions not originating from the genuine *ep* DIS event are present during the energy measurement. One noise source is related to the capacitance of the LAr cells and of the amplifiers which process the signals, while another noise source is beam induced [96, 100]. This two noise sources are indistingible from the real LAr signal during the data taking phase.

In contrast to the data, the energy depositions obtained over the whole detector with the MC simulation arise exclusively from the *ep* collision. Thus, in order to compare the energy measured in the LAr with the MC simulation, the noise present in the data also has to be considered. Two strategies can be followed, one can either try to simulate the noise or one can add the noise to the MC extracted from real data. The noise simulation is difficult, since it changes with the run period and the beam conditions and its shape is not a simple gaussian distribution which could be added to the signal of the calorimeter cells. Therefore in H1 the LAr noise is added simply to the MC simulation using its sprectra recorded with real data.

The noise is readout in special runs known as *"noise files"*. The aim of the *noise-file* is to record the sprectrum of the noise of each LAr cell. The *noise-file* is taken with random triggers. The task of the random trigger is to get empty events without any physics signal originating from *ep* event. Thus, in the ideal case pure noise should be collected. The *noise-files* are runs qualified

as poor and usually are taken with *ep* collisions and contains typically only 1000 events. The noise file recorded for the shifted vertex period will be in the following section called *"default noise-file"*.

Each event of the MC simulation, will contain in addition to the energy depositions of the *ep* collision the energy deposited of one event of the *noise-file*. This means that each $N-$th events [1], the same noise pattern is fed into the MC simulation. After the noise from the *noise file* is incorporated in the MC simulation, the noise suppresion algorithms will be performed in the same way as applied to the data.

For events coming from the normal data taking, the signal of the LAr cells is readout only in case, its deposited charge is greater than the noise cut σ. The value of σ depends on the position of the module, having a value which varies between 10 MeV and 30 MeV [40, 91]. This noise suppression is applied online for all data. However, this cut is *not* applied if a *noise-file* is taken, since the aim of the *noise-file* is to readout the whole noise spectrum. Thus, the first noise suppression which is performed in the MC, is the application of the online σ cut.

The noise suppression is performed to all LAr calorimeter cells, and it can occur that the investigated cell has a energy which is below the σ or pedestrial value. In order not to overestimate the signal, the cells which have negative energy below the σ value will not be excluded. Thus, the noise substraction is performed using the absolute value of the energy threshold $n \cdot \sigma$ (the value of n depend on the octant in which the cell is located).

During the reconstruction of the energy measurement a so called "topological noise suppresion" is also performed. One cell will be considered in the cluster algorithm if its energy or the energy of its neighbor is higher than 4σ [98]. The noise suppression mechanism explained in the previous paragraphs together with the cluster algorithm is done in the same way for data and MC.

5.4.2 Investigation of the noise in the MC

In order to investigate the influence of the *noise file* and the noise which is identified by the FSCOMB algorithm, different MC simulations were produced varying the input *noise-file*. In order not to change the physics coming from the *ep* DIS event the MC simulations must have the same generated files as the ones disccussed in section 3.2.

The following MC samples were produced:

[1] where N is the length of the noise file

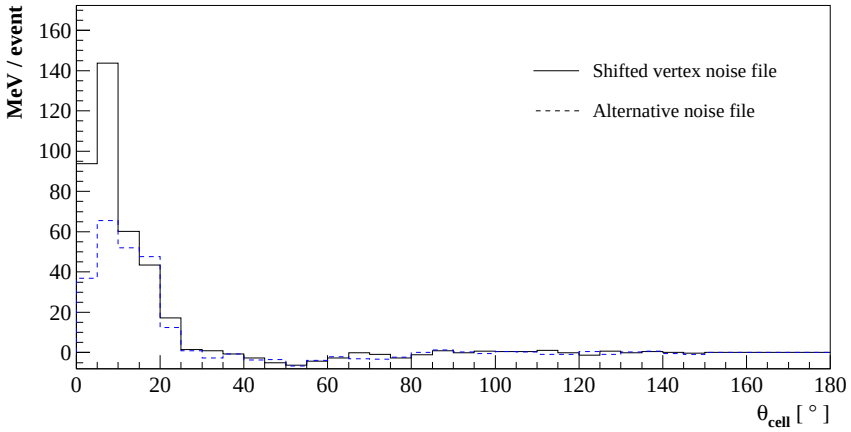

Figure 5.9: Comparison of the angular energy deposition in the *noise-files* (plot from [100]).

1. **Half-Noise MC sample.**
   As already mentioned the noise-files posess only 1000 events, thus its statistic could create a bias in the final measured distributions, since each 1000 event the same pattern of noise is used. To study the influence of this possible bias a MC with half of the statistics of the used noise-file was produced.

2. **Alternative noise file MC sample.**
   In order to investigate how the final measured distribution are influenced by the added noise, an alternative *noise-file* was used to produce the MC simulation. The *noise-file* used until now, were recorded one day after the shifted vertex run period. The alternative *noise-file* was recorded three month before the shifted vertex period [2].

   The amount of added energy on the *default* and *alternative noise file* after applying the online cut as function of θ_{cell} is shown in Fig. 5.9. One can see that the *default noise-file* of the shifted vertex data has in average more deposited energy than the *alternative* one. How much this additional noise changes the hadronic distributions will be discussed in the next section.

3. **No-Added noise MC sample**
   A MC where only the energy deposition in the LAr comes from the real ep scattering is obtained by dropping the contribution derived from the *noise-file*. In order to compare with the data the pedestal or σ cut value is performed. This MC can be used to derive an upper limit of the error due to a "wrong" identification of the noise.

[2]The *noise-file* for the shifted vertex data was taken at 21.08.00 in the lumi fill 2601 while the alternative *noise-file* was taken in the lumi fill 2462 the 11.06.00

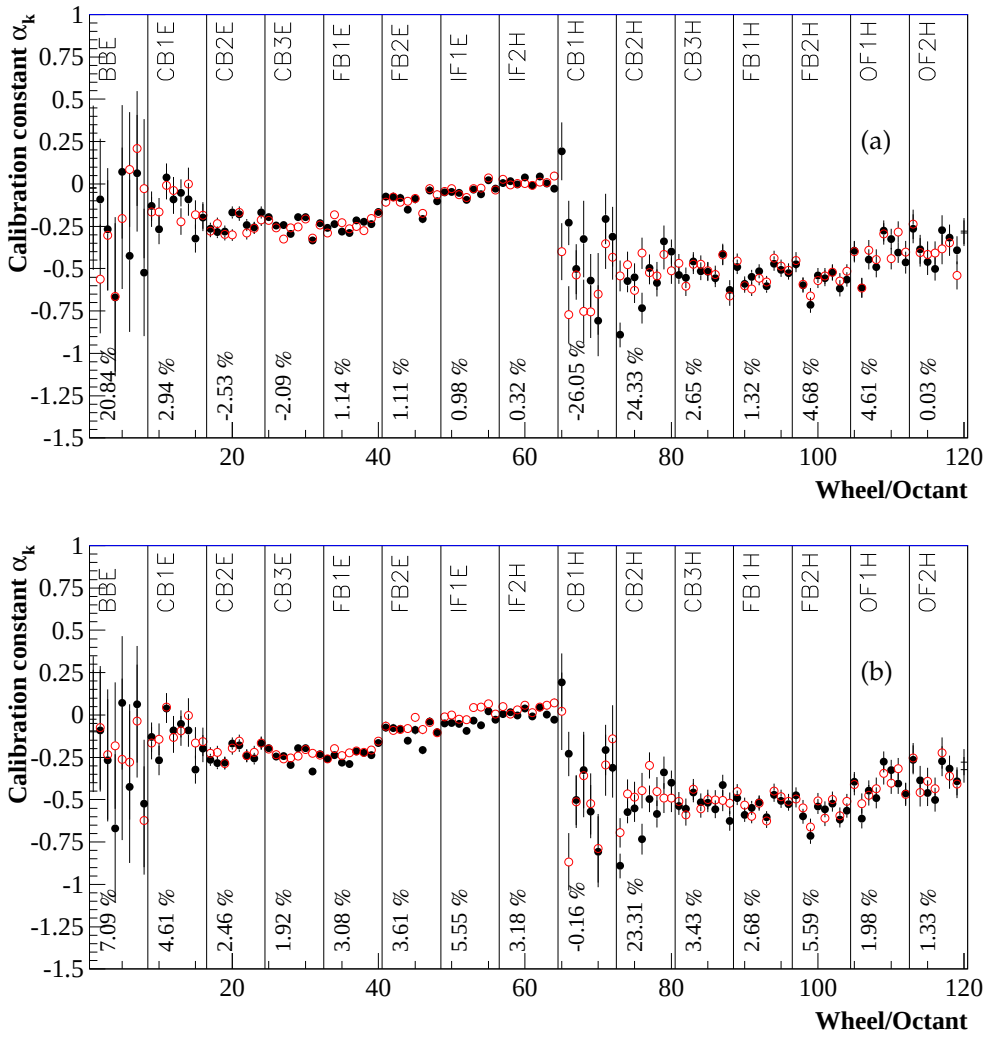

Figure 5.10: Comparison of the calibration constants for the LAr calorimeter for DJANGOH MC, open points represent the default simulation, closed circles correspond to the MC simulation with (a) a *noise-file* recorded before Shifted vertex period and (b) no electronic noise applied to the simulation. The percent values correspond to the deviation of the constants from the default simulation

In the following subsections, the HFS distributions for each of the special MC simulations together with the default MC simulation are presented. The data sample of the three special MC simulations were calibrated with the Lagrangian method explained in section 5.3.

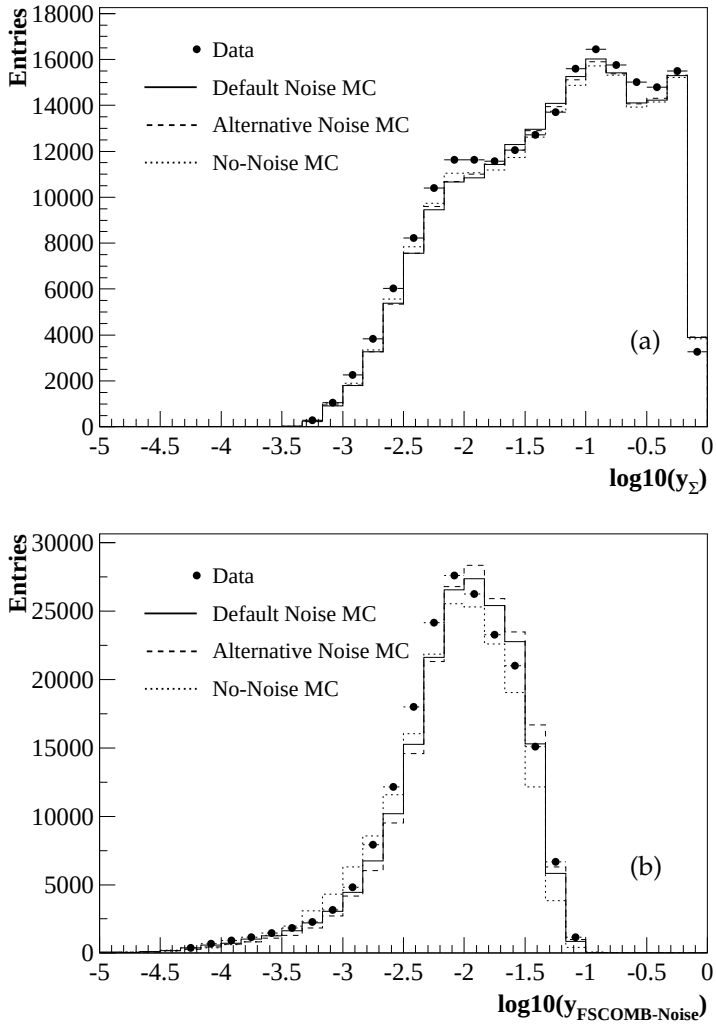

Figure 5.11: (a) Comparison between data and the different MC simulations of the y_Σ distributions of the DIS sample. (b) Comparison between data and MC for the mean value in y of the noise identified by the FSCOMB algorithm.

Half-Noise MC

The calibration constants with half of the statistic of the default *noise-file* do not considerably change from the calibration constants compared to the whole statistic. The main distributions as $p_{t,bal}$ and y_Σ show the same behaviour as the distributions presented in section 5.3.2. Therefore this result does confirm that the statistics of the *noise-file* does not affect the measured final distributions.

Alternative-Noise and No-Added-Noise MC

Variations of the calibration constants are observed in the simulation when the *alternative noise-file* is used and when no-noise is added. In Fig. 5.10 is shown the comparison of the calibration constants between the default MC simulation (closed points) and the alternative *noise-file* (a) and the simulation without addition of noise (b). The calibration constants for the *alternative-noise* MC differ in average by 2% from the calibration constants of the default *noise-file*. In case the noise is not added in the MC simulation, the calibration constants differ 3% and 6% from the default MC, as follows from Fig. 5.10 (b). The calibration constants of the CBH1 modules vary strongly due to the limited statistic.

The comparisons between the data and the different MC simulations for the y_Σ distributions are shown in Fig. 5.11(a). The excess of data over MC at $y_\Sigma \approx 10^{-2}$ is always present and seems to be independent of the choice of the *noise-file*.

Fig. 5.11(b) shows the mean value in y_{had} of the noise identified by the FSCOMB algorithm (see 5.2.1). The noise identified by the FSCOMB algorithm is localised in average at the same values of y_{had} for each MC simulation. In fact, also the simulation where **no noise** was added, shows the same behaviour. For the no-noise MC the average value of y_{had} is found towards lower values than the simulations where the noise was explicity added using the *noise-files* (see Fig.5.11(b)). This is expected since, no additional noise is explicitly added. Comparing the distributions of the position in y_{had} of the noise in Fig. 5.11(b), it is clear that the FSCOMB algorithm identifies more noise than acctually is added. The isolated clusters which the FSCOMB algorithm identifies as noise do not always correspond to the noise added with the *noise-file* in the MC simulation. **Part** of those isolated cluster can be real signals coming from the ep scattering.

The isolated clusters which are identified by FSCOMB as noise, are located mainly in the forward region and are isotropically distributed in azimuth. However, the substraction of the FSCOMB noise is necessary since its incorporation into the reconstruction of the kinematical variables conduces to a huge disagreement between the data and the MC simulation of more than 10%. Fig. 5.12 show the distributions of y_Σ in case the FSCOMB noise is not substracted. The y_Σ distribution is better described if the FSCOMB noise is substracted (compare Fig. 5.7(a) with Fig. 5.12(a).)

Another source of noise can influence the measurement of the $(E - p_z)_{had}$ of the HFS. These energy depositions are coming from back scattered particles in the forward region. This rescattering contribution is included already in the MC simulation.

From this results one concludes that:

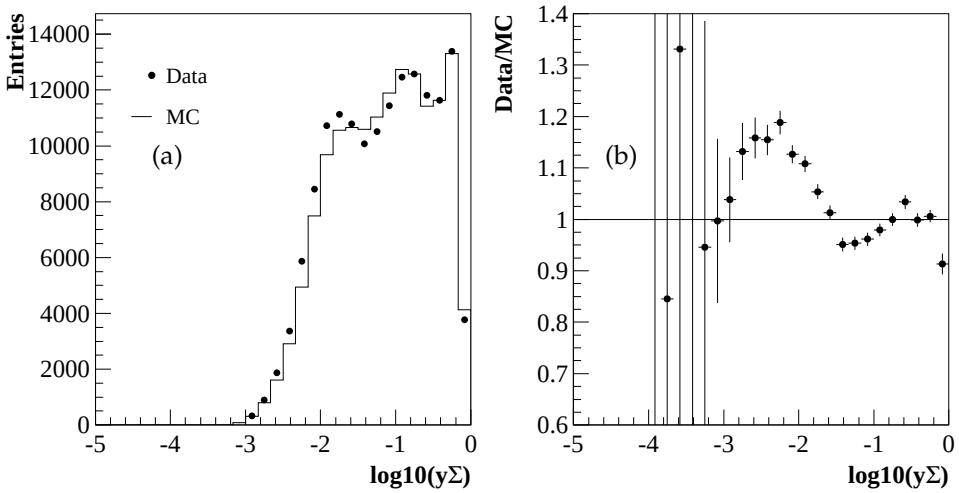

Figure 5.12: The inelasticity variable y_Σ not substracting the FSCOMB noise.

- The addition of the *noise-files* does not considerably change the measured distributions relevant for the F_2 measurement.

  The relative contribution of the LAr calorimeter differ from the *official* and the *alternative noise file* by less than 2%. Fig. 5.13(a) shows the y_{had} decomposition of the data and the comparison between the MC simulations using different noise files. The drawn band in Fig. 5.13(a) represent the variations of the hadronic response using the default MC and the MC with the *alternative noise-file*. The width of the band is less than 2% over all accessed values of y_{had}

- The noise identified by the FSCOMB algorithm has the biggest influence on the reconstruction of y_{had} and y_Σ for values of $O(10^{-2})$.

The excess of the data in comparison with the MC remains. Nevertheless the uncertainty of the noise identification performed by FSCOMB has to be taken into account. The uncertainty will be calculated using the variation between data and MC of the FSCOMB noise over the whole y_{had} range. Since the MC without *noise-file* is not able to describe the data, the uncertainty is derived using the MC with the *default noise-file*. In Fig. 5.13(b) is shown the y_{had} decomposition distribution for the no noise MC simulation. For this MC simulation, the LAr contribution and of course the LAr-noise contribution completely disagree with the measured data.

The uncertainty due to the noise substraction procedure is taken to be 10%. In Fig. 5.14(a) the y_{had} decomposition distribution is shown again. The band corresponds to the variation of the LAr and the FSCOMB noise, in case the FSCOMB noise is varied by 10%. In Fig. 5.14(b) is shown the ratio of the noise fraction between data and MC taken from the default MC. From this

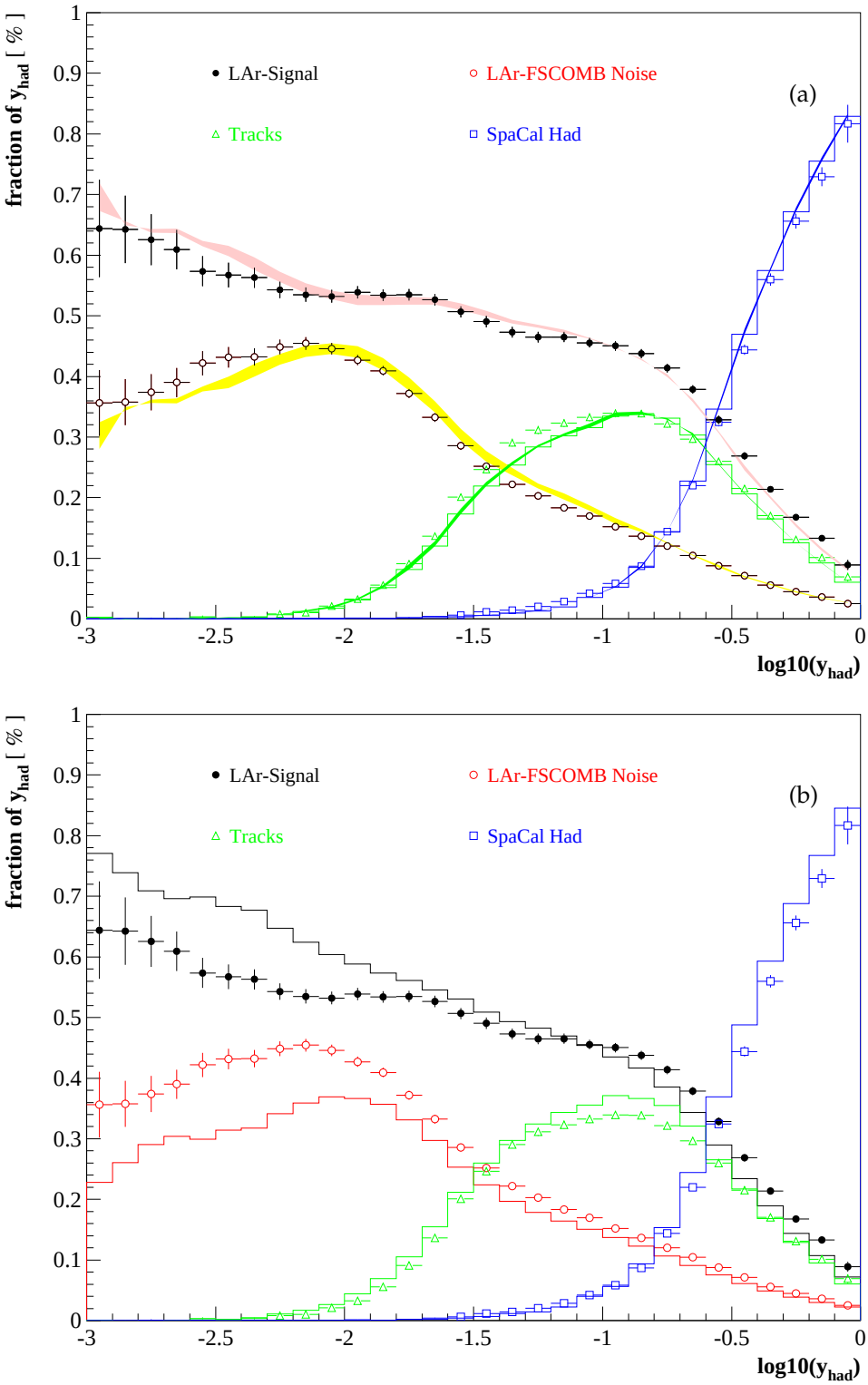

Figure 5.13: Contribution to y_{had} from the different subdetector components for data (closed points) and MC (a) using the *official* and *alternative* noise file. The bands represent the variation between the two MC simulation, their width does not exceed 2%. (b) Contribution to y_{had} of data (closed points) and the No-noise MC simulation (histogram).

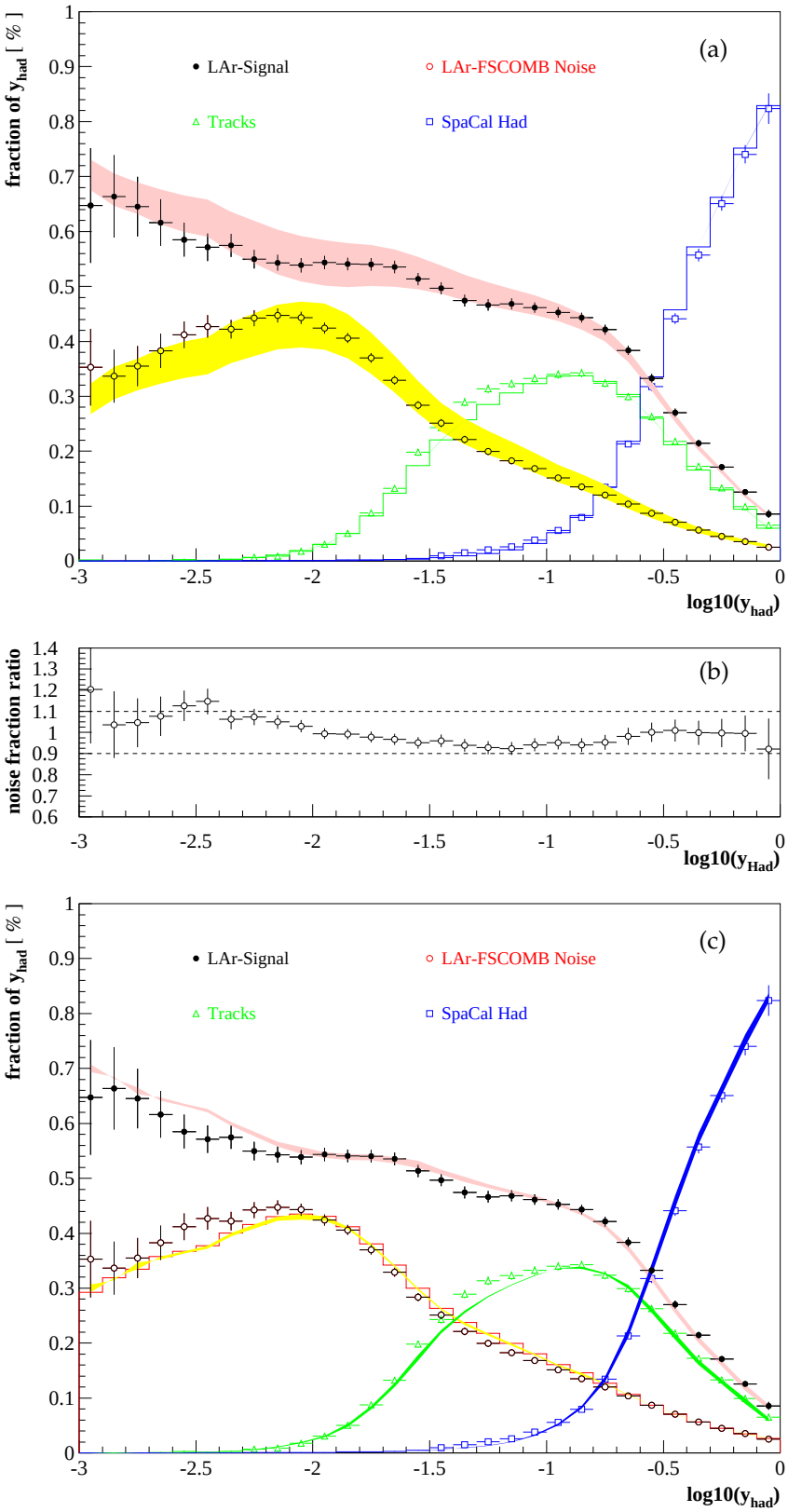

Figure 5.14: (a)Contributions to y_{had} from different detector components in case the FSCOMB noise is varied by 10%. (b) The ratio of data and the *official* MC of the FSCOMB noise fraction. (c) Contributions to y_{had} from different detector components in case the LAr signal is varied linearly by 10% at $y = 10^{-3}$ and 2% at $y = 10^{-2}$.

distribution follows that the assigned 10% uncertainty is conservative over the whole measured phase space.

Since at $y = 10^{-3}$ the noise is significant, the uncertainty of the *LAr signal* is taken to be 10% at $y = 10^{-3}$ and is extrapolated linearly to 2% at $y = 10^{-2}$. Fig. 5.14(c) shows the decomposition of y_{had} for data and the default MC in case the LAr signal is varied by its uncertainty (10% − 2%). The drawn band correspond to the asigned uncertainty of the *LAr signal*.

The uncertainties of the *LAr signal* and *Noise* will be taken into account for the determination of the systematic errors of the F_2 measurement.

One additional remark concerning the official *noise-file* used for the shifter vertex data period is necessary: it was recorded one day after the shifted vertex period ended. Thus, it was not clear if the noise conditions of the *noise-file* are appropiate for the shifted vertex data sample. One possibility to verify it is using so called "random-events". These data are recorded always during the data taking with a constant rate. The main difference between the random-events and the noise-files is, that the random-runs posess the online noise suppression cut of 2σ [3]. Therefore not all cells are read out and recorded. While, the *noise-files* contains the whole noise spectrum for all cells. However, this random events can be used to check the noise behaviour of the data period by comparing the noise contribution above the online noise σ cut. The comparison of the *noise-file* used for the shifted vertex MC with the random runs was performed in [100]. Good agreeement was found between the official *noise-file* and the random events of the shifted vertex period. Thus, the official *noise-file* is well suited to be used for the MC of the shifted vertex period.

5.5 Diffractive Events

As was already pointed in section 5.3.2, the DJANGOH MC can reasonably describe the behaviour of the inclusive data. Nevertheless, in previous analysis it was already observed that DJANGOH is not appropiate to study exclusive processes like DVCS[101] and QEDC [102].

One possible explanation of the y_Σ discrepancy between data and MC could come from the diffractive component of the cross section. Diffractive events constitute 6% of the inclusive DIS cross section [103]. The DJANGOH MC used in this analysis, includes diffractive events through the model of soft color interactions. In order to investigate if this component has an influence on the y_Σ distribution and the energy flow, a MC sample using the same version of DJANGOH without the soft color interaction model was produced.

[3] The online noise suppresion cut is different for each module of the LAr.

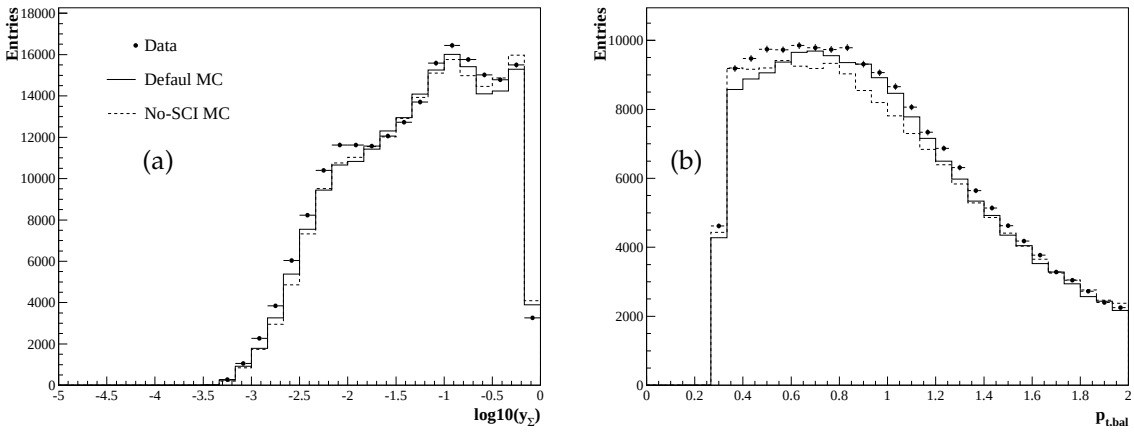

Figure 5.15: (a) y_Σ and (b) $p_{t,bal}$ distributions for the MC simulation where no diffractive events were generated.

In Fig. 5.15 the y_Σ and the $p_{t,bal}$ distributions are shown. The data are compared to the MC simulation where no diffractive events were generated. The diffractive contribution of the DJANGOH simulation is not localized in low y region. In addition the exclusion of the diffractive events creates an imbalance of the transversal energy as follows from Fig. 5.15(b). Therefore the diffractive component can not explain the differences observed between the data and the MC simulation in the low y region.

5.6 Hadronic energy scale uncertainty

In this chapter, the HFS was studied using the $p_{t,bal}$ and $(E - p_z)_{tot}$ distributions. The deviations of the MC simulation to the data were used to derive the systematic uncertainties which are listed in table 5.2.

Source	Uncertainty	reference
Noise identification	10%	Fig5.14(b)
Hadronic energy	10% for $y = 10^{-3}$	Fig 5.14(c)
	2% for $y = 10^{-2}$	
Hadronic SpaCal	350 MeV	Fig. 5.1(b)

Table 5.2: List of uncertainties on the hadronic measurement.

Chapter 6

Cross section Measurement

In this chapter the complete DIS selection is presented and the cross section measurement for the shifted vertex data is performed. The event selection used to identify the scattered electron with the SpaCal calorimeter and with the BST was already discussed in chapter 3. The efficiency of the electron identification was studied using a sample of ISR tagged events, since it has a minimal background contribution. Nevertheless, the DIS sample is influenced at low energies of the scattered electron by the photoproduction background. Also, the measured distributions have contribution from processes like elastic QED compton scattering, which are not included in the MC simulation and have to be rejected. Thus, it is also important to study the efficiency of the cuts which define the full DIS selection. In section 6.1 the complete DIS selection is introduced together with the efficiency for the most important cuts.

One important step in the measurement of the DIS cross section is the identification of the fiducial region, where all used detector components worked properly, therefore a summary of the trigger efficiency during the shifted vertex data studied in [100] and its influence on this analysis is discussed in section 6.2.

In section 6.3 the $z-$vertex distribution of the event selection as reconstructed by the BST is studied and in section 6.4 the comparison between the data and the MC simulation for the most important variables is presented.

The method used to measure the cross section is explained in section 6.5. The migration of the selected events between the measured bins is studied in section 6.5.1 and the contribution to the cross section from non-tagged radiative events is discussed in section 6.5.2.

The cross section measurement and the extraction of the proton structure function F_2 are the subject of section 6.5. As already mentioned in section 3.1, this analysis uses the BST as the

main detector to reconstruct the angle of the scattered electron, nevertheless there is another possibility to reconstruct the angle of the scattered electron by using the BDC and the CTD. In this thesis only the BST results are described, the measurement of the BDC as well as the comparison of the cross section measurement determined in this thesis with the BDC is presented in [100].

In chapter 4 and 5 it was explained in detail how the calibration of the SpaCal and the LAr calorimeters were performed for the shifted vertex data. There, the scale of the energy measurement of the scattered electron was derived. Moreover, the deviations between data and MC of the transverse energy flow were used to determine the uncertainty of the hadronic energy measurement. These uncertainties together with the results of other analyses [100, 105] will be used to calculate the total error of the cross section measurement. These studies are presented in section 6.7.

6.1 DIS selection

Table 6.1 summarizes the cuts used to identify DIS events. The event selection is mainly performed by the SpaCal calorimeter and the BST, a minimal number of cuts depending on the hadronical final state are considered, this are the $p_{t,bal}$ and the $(E - p_z)_{tot}$ cuts (see Eq. 5.4 and Eq. 3.10 for the definition of both variables).

The efficiency of a cut is studied using the number of events that the particular cut has either accepted or rejected. Nevertheless some background contributions are only present in the data. For example, events coming from an empty pilot bunch are rejected from the data, but its efficiency can not be studied with the MC since such events are not simulated. Similarly, the MC does not simulate events due to the satellite part of the $z-$vertex distribution, therefore the $z-$vertex cut can not be excluded. In general, cuts which are applied to reduce effects which are not considered in the MC simulation can not be excluded to study the losses due to cut application. These cuts are marked as *fix* in Table 6.1 and will allways be applied.

The efficiency of the cut-i is defined as,

$$\epsilon(cut - i) = \frac{N_{all}}{N_{all} + N_{rej,cut-i}} \tag{6.1}$$

where N_{all} is the number of events accepted by the DIS selection and $N_{rej,cut-i}$ is the number of good events rejected by the $cut - i$. Since the data include a certain amount of background, the

DIS selection			
	Efficiency Study	Cut	Recontruction method
SpaCal:	fix	Fiducial volumen	e, Σ
	fix	$7\,\text{GeV} < E_e < 30\,\text{GeV}$	e, Σ
	+	$R_{clog} < 4\,\text{cm}$	e, Σ
	+	$E_{veto} < 1\,\text{GeV}$	e, Σ
	+	$f_{had} < 0.15$	e, Σ
BST:	+	$\Delta R = \lvert R_{bst} - R_{SpaCal} \rvert < 1.5\,\text{cm}$	e, Σ
	fix	$\lvert z_{BST} - 70 \rvert < 30\,\text{cm}$	e, Σ
	fix	$R_{bst} > 10\,\text{cm}$	e, Σ
	+	$N_{BST,hits} < 200$	e, Σ
Hadronical Final State:			
	+	$P_{t,bal} > 0.3$	e, Σ
	+	$R_{compton}$	e, Σ
	+	R_{veto}	e, Σ
	+	$(E - p_z) > 35\,\text{GeV}$	e

Table 6.1: DIS selection used to measure the inclusive cross section

PHOJET MC is used to estimate it. Thus,

$$N_{all} = N(data)_{acc} - N(PHOJET)_{acc} \qquad N_{rej,cut-i} = N(data)_{rej,cut-i} - N(PHOJET)_{rej,cut-i} \tag{6.2}$$

with $N(data)_{acc}$ and $N(PHOJET)_{acc}$ being the number of events accepted in the data and in the PHOJET MC using the whole DIS selection. The PHOJET contribution is normalized to the data using the normalization factor determined in section 3.6. In the following sections, the efficiency of the cuts cuts marked by a "plus" sign in Table 6.1 are studied and compared with the expectation of the signal MC DJANGOH.

6.1.1 R_{clog}

The transverse extension of the electron shower over the SpaCal plane R_{clog} is shown in Fig. 6.1. One can see that the MC does not describe the R_{clog} variable (see Eq. 3.17), in particular a shift between the data and the MC simulation is observed and the clusters with transverse extension greater than 4 cm are concentrated in the tail of the distribution. The shift of the R_{clog} variable is a known problem related to the fast shower simulation in MC [102].

The efficiency of the R_{clog} cut as function of the energy of the scattered electron E_e for the data and the DJANGOH MC is presented in Fig.6.2(a). The error band of the data corresponds to the uncertainty asigned to the background substraction 15% [106]. The limits of the band are obtained varying the phojet normalization 15%. The efficiency curve is not described by the MC simulation at lower energies.

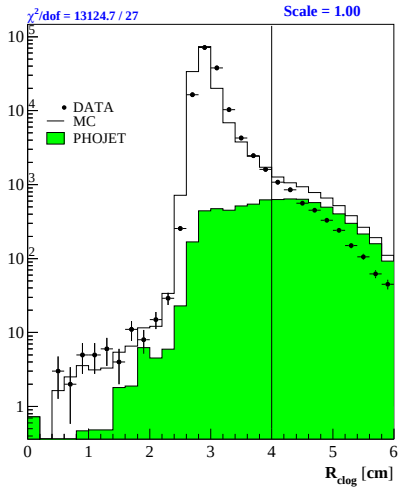

Figure 6.1: R_{clog} distribution of the scattered electron. Closed points represent data, while the histogram is the sum of DJANGOH and PHOJET MC. The background contribution derived from PHOJET is shown by the solid area. The line at 4 cm correspond to the analysis cut.

The exclusion of the R_{clog} cut leads to more background in the sample, and the PHOJET contribution for accepted and rejected events considerably changes. The efficiency was therefore studied using different PHOJET contributions for accepted and rejected events. Thus, the background contribution was determined as in section 3.6 but relaxing the R_{clog} cut. The normalization of the PHOJET MC to the data increases by almost 70%. In contrary to the accepted events, the energy distribution of the mis-identified scattered electron $\mathbf{E_e}$ is not described by the MC simulation for the *rejected* events.

The different normalization factors improve the description of the efficiency curve, as can be seen from Fig. 6.2(b). Nevertheless, discrepancies are still observed for the interval between 7 GeV and 9 GeV. This discrepancy is related to the non-description of the energy $\mathbf{E_e}$ of the rejected events by PHOJET and due to the non description of the R_{clog} variable itself (see the tail in Fig. 6.1). In section 3.5 it was shown that using a sample almost free of background events (the tagged ISR sample), the efficiency of the R_{clog} cut is in agreement with the DJANGOH MC simulation (see Fig. 3.7(a)).

6.1.2 f_{had}, ΔR, R_{veto}

In Fig.6.3(a) and (b) are shown the efficiency of the hadronic fraction $f_{had} < 0.15$ cut and of the SpaCal BST matching $\Delta R < 1.5$ cm cut, as function of the energy of the scattered electron E_e (see equations 3.18 and 3.19). The f_{had} cut is inefficient for low values of the energy of the scattered electron, but its behaviour is well described by the signal MC DJANGOH. For values

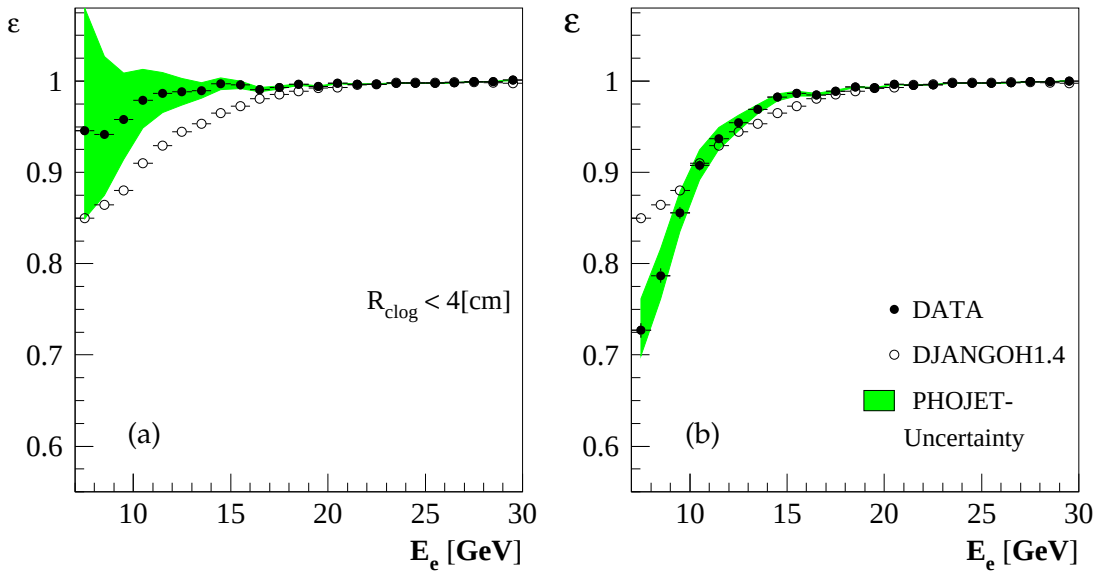

Figure 6.2: Efficiency of the $R_{clog} < 4\,\text{cm}$ cut as function of the energy of the scattered electron E_e. The open points shows the efficiency of the signal MC DJANGOH, while full points is data where the γp is substracted using the MC PHOJET. (a) The γp background is substracted from the data using the same normalization factor for $R_{clog} < 4\,\text{cm}$ and $R_{clog} > 4\,\text{cm}$. (b) Same as Fig. (a), but using different normalization factors for accepted and rejected events (see text). Thus, for Fig. (b) the γp background is substracted considering the relative contribution of γp to the data with $R_{clog} < 4\,\text{cm}$ and $R_{clog} > 4\,\text{cm}$.

of the scattered electron $E_e \approx 7\,\text{GeV}$, the efficiency of the ΔR cut goes to unphysical values. This is just a statistical fluctuation coming from the substraction of PHOJET. The difference between data and MC for both cuts do not exceed 2%.

The R_{veto} cut, rejects events with a wrongly recontructed vertex by the central tracking devices outside the $z-$vertex measured region $|z - 70| < 30\,\text{cm}$. From Fig. 6.3(d) follows that the R_{veto} cut is full efficient.

6.1.3 $R_{compton}$

In order to extract correctly the proton structure function from the measured cross section, it is necessary to correct for contributions coming from higher order radiative processes. The largest contributions to the corrections arise from QED processes in first order in α. In such processes a photon is radiated from the incoming electron or from the outgoing electron. Experimentally one distinguishes between different event classes in the detector, the QED Compton (QEDC) being one of those signatures.

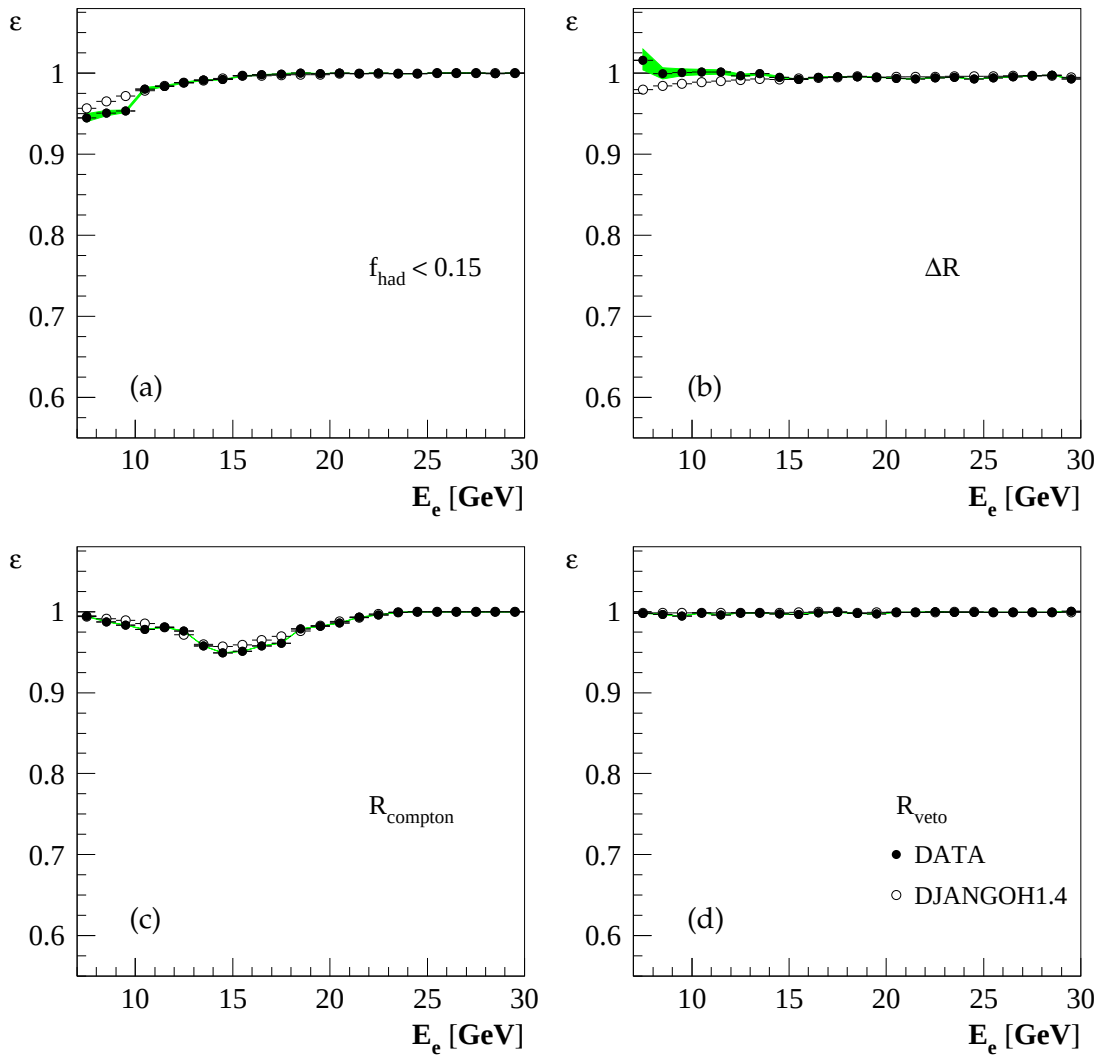

Figure 6.3: Efficiency of the selection cuts as function of the energy of the scattered electron E_e (a) the $f_{had} < 0.15$ cut (b) the SpaCal-BST matching $\Delta R < 1.5\,\text{cm}$ (c) the Compton rejection $R_{compton}$ cut and (d) the R_{veto} cut. The open points shows the efficiency of the signal MC DJANGOH, while full points is data where the γp is substracted using the MC PHOJET.

Since the DJANGOH1.4 MC includes only the inelastic component of the QEDC cross section and does not include the elastic contribution, a rejection of those events has to be performed. The QED Compton signature is characterised by two electromagnetic clusters in the backward region of the H1 detector, one corresponding to the scattered electron and the another to the radiated photon. The energy of both clusters can be measured with the SpaCal calorimeter. The electron and photon cluster should be in a "back to back" topology.

In elastic and most inelastic QEDC events, the detector is empty except for the electron and

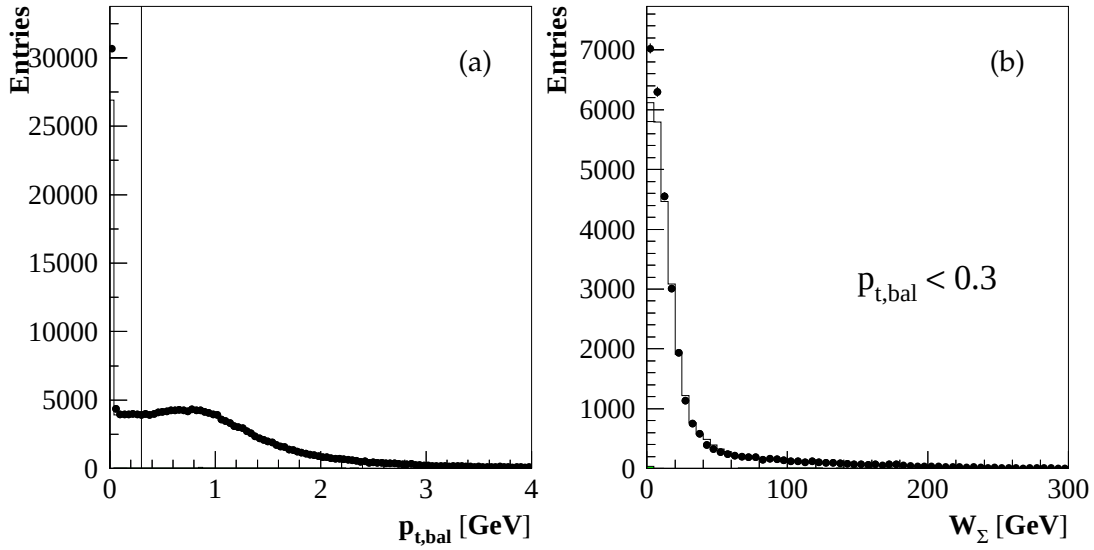

Figure 6.4: (a) $p_{t,bal}$ distribution for the DIS selection, the line represent the analysis cut. (b) W_Σ distribution for events which pass the DIS selection and have $p_{t,bal} < 0.3$.

the photon, so that no central tracks are reconstructed. Although the requirement of a vertex reconstructed with the CTD reduced the contribution of the QEDC events to the cross section, a small fraction can still remain if one reconstruct the vertex with the BST [90, 102].

The cuts used to reject the QED Compton events, follow the selection criteria developed in [102]. $R_{compton}$ considers the following selection to reject the compton events. The energies of the electron and photon clusters should be greater than 4 GeV and the sum of the energy of both clusters should be greater than 18 GeV. Also, the difference of the azimuthal angle between the electron and photon clusters should correspond approximately to $\phi \approx 180^\circ$. In case the event fulfil those requirement it will be rejected.

In Fig. 6.3(c) is shown the efficiency of the $R_{compton}$ cut as function of the energy of the scattered electron. The rejection due to the $R_{compton}$ cut is localized mainly between 15 GeV and 20 GeV. The differences of data and MC do not exceed 2%.

6.1.4 $p_{t,bal}$

As was already mentioned in the previous chapter, the acceptance of the backward and forward part of the detector is limited due to the beam pipe holes used to store the beams. The hadronic final state can be produced at small angles escaping the forward calorimeter acceptance; this

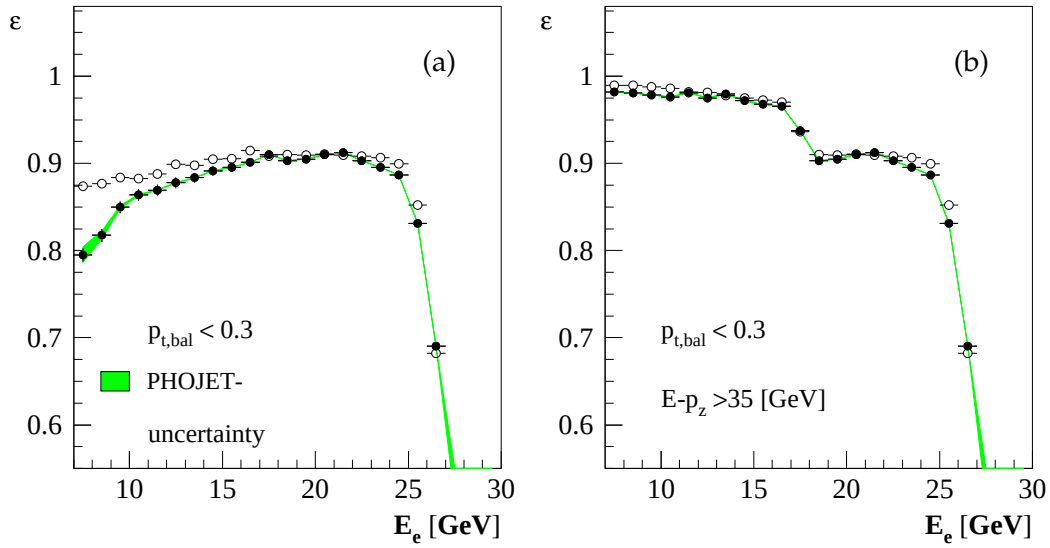

Figure 6.5: (a) Efficiency of the $p_{t,bal} < 0.3$ cut as function of the energy E_e of the scattered electron. (b) Efficiency of the $p_{t,bal} < 0.3$ cut having in addition a $E - p_z > 35\,\text{GeV}$ cut. The open points show the efficiency of the signal MC DJANGOH, while full points correspond to data where the γp is substracted using PHOJET

.

cut can create an imbalance of the transverse momenta of the hadrons with the electron. Such non-balanced events are concentrated mainly at very small $p_{t,bal}$ values, which is shown in Fig. 6.4(a).

The losses become especially pronounced for high values of x (low y). This region corresponds to the resonance region where W tends to be small. In Fig. 6.4(b) is shown the W_Σ distribution for events having $p_{t,bal} < 0.3$, it can be seen that those events are mainly concentrated in the interval $W_\Sigma < 50\,\text{GeV}$.

Fig.6.4(a) and (b) demonstrate that the $p_{t,bal}$ cut has to be performed in order to reduce the losses of low $p_{t,had}$ particles, since the MC simulation does not follow the behaviour of the data for values of $p_{t,bal} < 0.3$ and conservatively $W_\Sigma < 50\,\text{GeV}$.

The efficiency of the $p_{t,bal} < 0.3$ cut as function of the energy of the scattered electron is shown in Fig. 6.5(a). The efficiency is not completely described by the MC simulation for values of $E_e \leq 15\,\text{GeV}$. Excluding the $p_{t,bal} < 0.3$ cut, more non balanced events enters to the selection and much of them should be background. In order to minimize the background contribution, the efficiency for the $p_{t,bal} < 0.3$ cut is studied using in addition a $(E - p_z)_{tot} > 35\,\text{GeV}$ cut, which is used in the analysis for the region where the electron method is applied. The $(E - p_z)_{tot} > 35\,\text{GeV}$ cut, will guarantee that the longitudinal energy conservation is fulfilled. The efficiency

of the $p_{t,bal} > 0.3$ cut subsample is shown in Fig. 6.5(b), where a good description of the data by the MC DJANGOH simulation is observed.

However, the $(E - p_z)_{tot} > 35\,\text{GeV}$ cut is not performed in case the kinematic is reconstructed with the Σ method. On one hand, one sees that once the longitudinal energy conservation is fulfill, the $p_{t,bal}$ efficiency is good described, the discrepancy observed in Fig. 6.5(a) can be related to background contribution or to an incomplete implementation of the physics of the MC. The DJANGOH MC does not generate events in the region where both x and y are small, since $Q^2 \approx syx$, those events are mainly concentrated for low values of Q^2. Thus, the description of the $p_{t,bal}$ efficiency for $Q^2 > 2\,\text{GeV}^2$ should be better described even not applying the $(E - p_z)_{tot}$ cut. This efficiency is shown in Fig. 6.6, also a good agreement between data and MC is found.

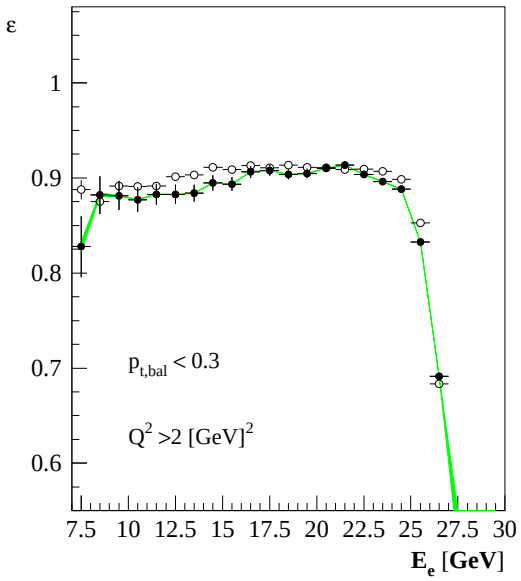

Figure 6.6: Efficiency of the $p_{t,bal} < 0.3$ cut using only events with $Q^2_\Sigma > 2\text{GeV}^2$. Open points show the efficiency of the signal MC DJANGOH, while full points is data where the γp is substracted using PHOJET.

6.1.5 $(E - p_z)_{tot}$

The $(E - p_z)_{tot} > 35\,\text{GeV}$ cut is applied only in case the kinematical variables will be reconstructed with the electron method. This cut is applied to reduce the contribution of photoproduction background and ISR events.

The efficiency of the $(E - p_z)_{tot} > 35\,\text{GeV}$ cut is shown in Fig. 6.7, one observes that DJANGOH MC describes the behaviour of the data. For energies of the scattered electron greater than 17.5 GeV, the $(E - p_z)_{tot}$ from the electron is sufficient to satisfy the cut $(E - p_z) > 35\,\text{GeV}$ cut, so the efficiency is 100%. For energies of the scattered electron lower than 17.5 GeV, the $(E - p_z)_{tot}$ of the electron is not sufficient to satisfy the $(E - p_z)_{tot} > 35\,\text{GeV}$ cut and therefore the $(E - p_z)_{tot}$ from the hadrons begin to become important. The drop of the efficiency curve can be explained to be due to particles escaping through the beampipe in the backward direction and therefore the measured $(E - p_z)_{tot}$ will be smaller than $2E_{inc}$ or the event is a ISR one.

The $(E - p_z)_{tot}$ cut is not applied in case the kinematical variables are reconstructed with the Σ

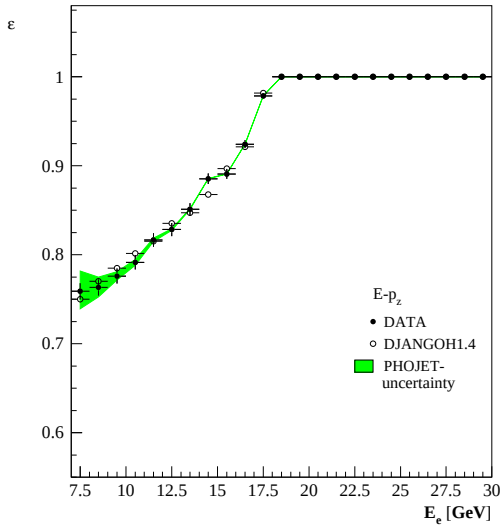

Figure 6.7: Efficiency of the $(E - p_z)_{tot} > 35\,\text{GeV}$ cut as function of the energy of the scattered electron E_e. Open points is the efficiency of DJANGOH MC while closed points are data where the γp background is substracted using PHOJET.

method. However, the kinematical variables are also correctly reconstructed since, contrary to the electron method, the centre of mass energy is corrected for the photon emission in this case (see section 3.3.3 for details).

6.2 Trigger efficiency and fiducial volumen

The relevant triggers used in the low Q^2 analysis are $S0$, $S3$ and $S9$. Table 6.2 summarises the configuration of $S0$, $S3$, $S9$ during the shifted vertex period.

The basic information comes from the deposited energy in the SpaCal calorimeter cells. This energy deposition defines the bits of the Inclusive Electron Trigger (IET), which is the basis of all trigger elements delivered by SpaCal. IET considers three different energy thresholds denoted

Subtrigger	L1	L2
S0	IET>1 || Cen−LIET > 2	R_{10}
S3	IET>2 || Cen−LIET > 3	
S9	IET>0	

Table 6.2: The trigger configuration for the shifted vertex run. The IET and Cen-IET regions are illustrated in Fig. 6.8.

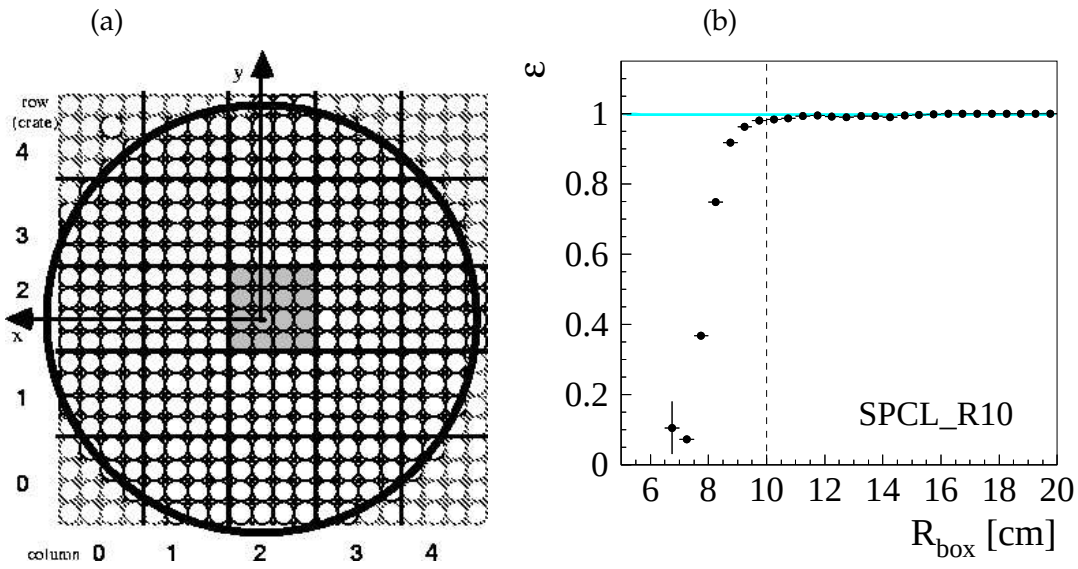

Figure 6.8: (a) The inclusive electron trigger structure (IET). The Central-IET (CIET) region is illustrated by the shadow area. (b) Trigger efficiency of S0 studied in [100]

as IET$>$ 1, 2, 3 and discriminates at L1 between different SpaCal regions. The thresholds of IET$>$ 1, 2, 3 during the shifted vertex period were set to 2, 5, 10 GeV, respectively. The central IET Cen$-$IET region cover mainly the inner region of the SpaCal surface. In Fig. 6.8 the coverage of IET and Cen$-$IET is shown. During the shifted vertex period, the thresholds of Cen$-$IET were also set to 2, 5, 10 GeV.

Due to the acceptance of the BST during the shifted vertex period, only S0 is used. The subtrigger *S*0 has a threshold of 5 GeV and a L2 condition R_{10}. The L2 condition means that only events are considered, which contain at least one impact outside a circle of 10 cm on the SpaCal surface.

The efficiency of *S*0 was studied in [100] and is calculated taking as reference a group of independent subtriggers which validate the event. The reference sample considers events where only one electron candidate was at L4 reconstructed. In order to minimise the influence of background events in the reference sample, an additional electron identification selection has to be applied. Also, the time of flight of the electron candidate should correspond to the time expected of an *ep* collision.

Fig 6.8(b) shows the efficiency of *S*0 as function $R_{box} = max(|x_{cl}|, |y_{cl}|)$ of the scattered electron measured by the SpaCal calorimeter. Using only S0, the fiducial volumen is restricted to a SpaCal surface with a box cut of 10 cm. This trigger region together with the cells which were excluded in chapter 3 constitute the fiducial volumen on the SpaCal plane used in the BST

analysis.

6.3 Event Weight

As was already mentioned in the previous section, the BST analysis is performed using only events accepted by the S0 trigger. Since during the shifted vertex period, S0 had a prescale different of one, each event had to be corrected with the corresponding prescale factor of the analysed run. In average the prescale of S0 was 1.15.

For MC there are two weights which are used, one is related to the vertex position of the simulated events, and the other corresponds to the structure function assumption of the MC. These two weights are briefly explained in the followings sections.

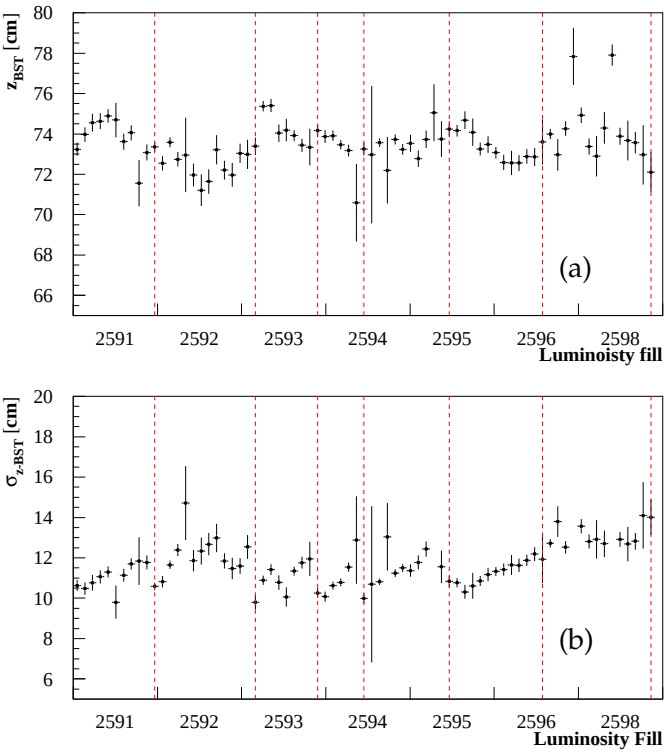

Figure 6.9: Position (a) and spread (b) of the interaction point of the ep scattering as measured by the BST during the analysed luminosity fills of the shifted vertex data period.

6.3.1 $z-$vertex Reweighting in the MC

The determination of the vertex position is important to correctly reconstruct the kinematic variables, since its precision directly influences the measurement of the angle of the scattered electron. In Fig 6.9 is shown the mean and width of the vertex position measured by the BST during the shifted vertex data period as function of the analysed run. The dashed lines indicates the luminosity fills. From Fig. 6.9(a) and (b) one can see that the mean position and the width of the vertex changes during the luminosity fill [99].

Contrary to the data, the vertex position of the MC is a gaussian distribution with a fixed mean position and width. Since the distribution of the vertex position of the data differs from the

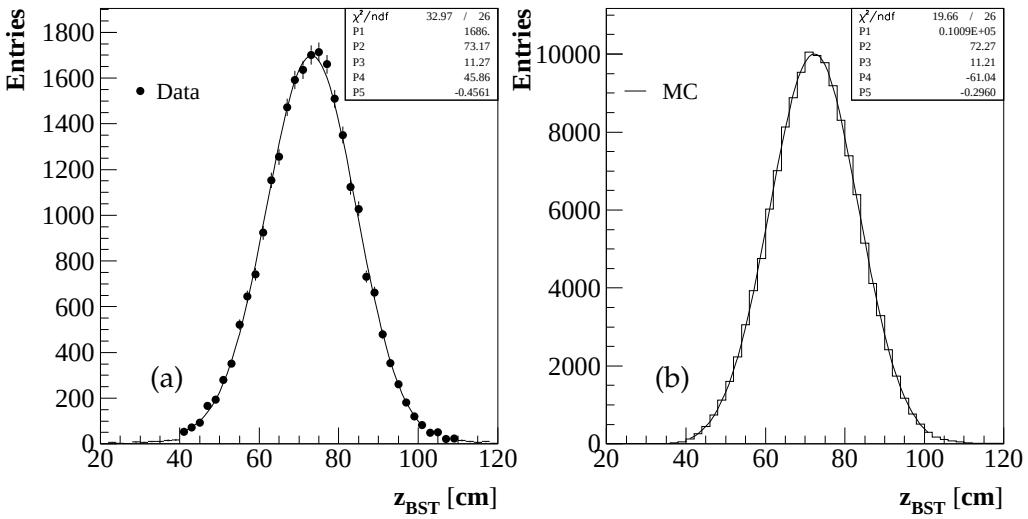

Figure 6.10: $z-$vertex distribution measured by the BST in a restricted θ range (see text) using (a) data und (b) MC. The line in (a) and (b) illustrates the fit of the data and MC distrubution to the sum of the Gaussian and the polynomial of first grad.

$z-$vertex simulated, the MC events are reweighted as a function of the $z-$vertex distribution. Such it is possible to match the $z-$vertex distribution of the MC simulation to the $z-$vertex distribution of the data.

The z-vertex reweighting procedure requires a sample which ideally is not influenced by additional systematic deviations and be inside the BST acceptance.

In order to get a $z-$vertex position in the BST acceptance, and to guarantee that all possible $z-$vertex values are considered, only events with electron candidates which are located in the interval $175^\circ < \theta < 176.5^\circ$ are accepted. This angular interval correspond to the best radial acceptance of the BST projecting on the SpaCal plane, which correspond to 12cm$< R_{SpaCal} <$ 22 cm. In addition, the Spacal selection of Table 6.1 is applied, *but* the energy of the scattered electron should be greater than 15 GeV in order to reduce the contribution of photoproduction events. The $z-$vertex distribution for data and MC for the previos selection is shown in Fig. 6.10. It can be seen, that the $z-$vertex distributions are slighlty asymmetric, thus a sum of a gaussian function and a polynomial of first order can describe satisfactorily the tails of the vertex distributions.

The weight to be used in the analysis is calculated as:

	data	MC
P0	1685.69	10088.98
P1	73.167	72.274
P2	11.272	11.211
P3	45.858	−60.937
P4	−0.456	−0.297

Table 6.3: Data and MC parameters of the fit performed to the vertex distribution using the function G

$$weight_{z-vertex} = \frac{G(z_v^{data}, P_i^{data})}{G(z_v^{MC}, P_i^{MC})} \tag{6.3}$$

$$\tag{6.4}$$

where $G(z_v^{data}, P_i^{data})$, $G(z_v^{MC}, P_i^{MC})$ are the sum of a gaussian function and a polynomial obtained from the fit of the $z-$vertex distributions of data and MC, respectively.

$$G(z_v^{data}, P_i^{data}) = P1 \exp((z_v^{data} - P2)^2/2P3^2) + P4 + P5\, z_v^{data}$$

The fit parameters are shown in Fig. 6.10(a) and (b), and listed in table 6.3.

6.3.2 MC reweight

At generator level, the DJANGOH1.4 simulations were performed using the parton distribution functions of the MRST(3,75) [104] group. These functions were selected due to their reasonable behaviour over most of the measured kinematic range. However the MRST functions are only applicable for $Q^2 \geq 1.25\,\mathrm{GeV}^2$, and are not expected to describe completely the data for lower values of Q^2. In previous analyses [105], it was shown that the data can be described using the fractal model [36] and the ALLM97 [33] fit, therefore during the analysis the events were re-weighted according to:

$$weigth_\sigma = \frac{\sigma_{red}^{Fit}(Q^2, x)}{\sigma_{red}^{Gen}(Q^2, x)} \tag{6.5}$$

where σ_{red}^{Gen} correspond to the originally generated cross section and σ_{red}^{Fit} is the cross section computed from the expectation of the fractal and the ALLM97 fit. Since the fractal fit only

describes the low x region, for events having a generated value of x lower than 0.01 the fractal fit while for the region $x > 0.01$ the ALLM97 fit is used.

6.4 Control Distributions of the DIS sample

In order to measure the cross section, it is necessary to verify if the MC simulation can reproduce the behaviour of the data. Therefore the distributions of the most important variables were compared with the MC simulation. The MC and the data have to contain all calibration constants and the weights introduced in the previous sections.

The final distributions of the main variables used to measure the cross section and to extract the proton structure function F_2 are shown in Fig 6.11 and in Fig 6.12. The MC is shown as the sum of the signal MC DJANGOH and the background MC PHOJET. The background contribution in each distribution is shown in addition as a shaded area. In all figures presented in Fig. 6.11 and Fig. 6.12 all cuts listed in 6.1 are applied.

The DJANGO MC is reweighted with the procedure explained in section 6.3.2 and normalized to the integrated luminosity of the data which is $450\,\mathrm{nb}^{-1}$. However the fractal fit used to reweight the MC was performed using previous H1 measurements with a wrong luminosity calculation. The difference between the luminosity used to perform the fractal fit and the value used in this analysis is 5%. The MC simulation is therefore 5% lower than the data. Nevertheless, the shape of the measured distributions are well described by the MC simulation.

In Fig 6.11(a),(b) are shown the energy and the angle of the scattered electron measured by the SpaCal calorimeter and by the BST. The vertex distribution is shown in Fig. 6.11(c). The kinematical variables x, Q^2 and y reconstructed with the electron method, are shown in Fig 6.11 (d),(e),(f). In general a good agreement between the data and the MC simulation is observed.

In Fig 6.12, the $E - p_z$ and $p_{t,had}$ distribution for the whole DIS selection is presented. The kinematical variables reconstructed with the $\Sigma-$method are shown in Fig. 6.12(c),(d) and (e). The y_Σ distribution is reasonably described having an excess in $y \approx 10^{-2}$, whose origin could not be completely explained due to the noise in the LAr.

Since most of the variables are well described, the cross section and the extraction of F_2 can be performed. In the next section the method used to measure the cross section will be discussed.

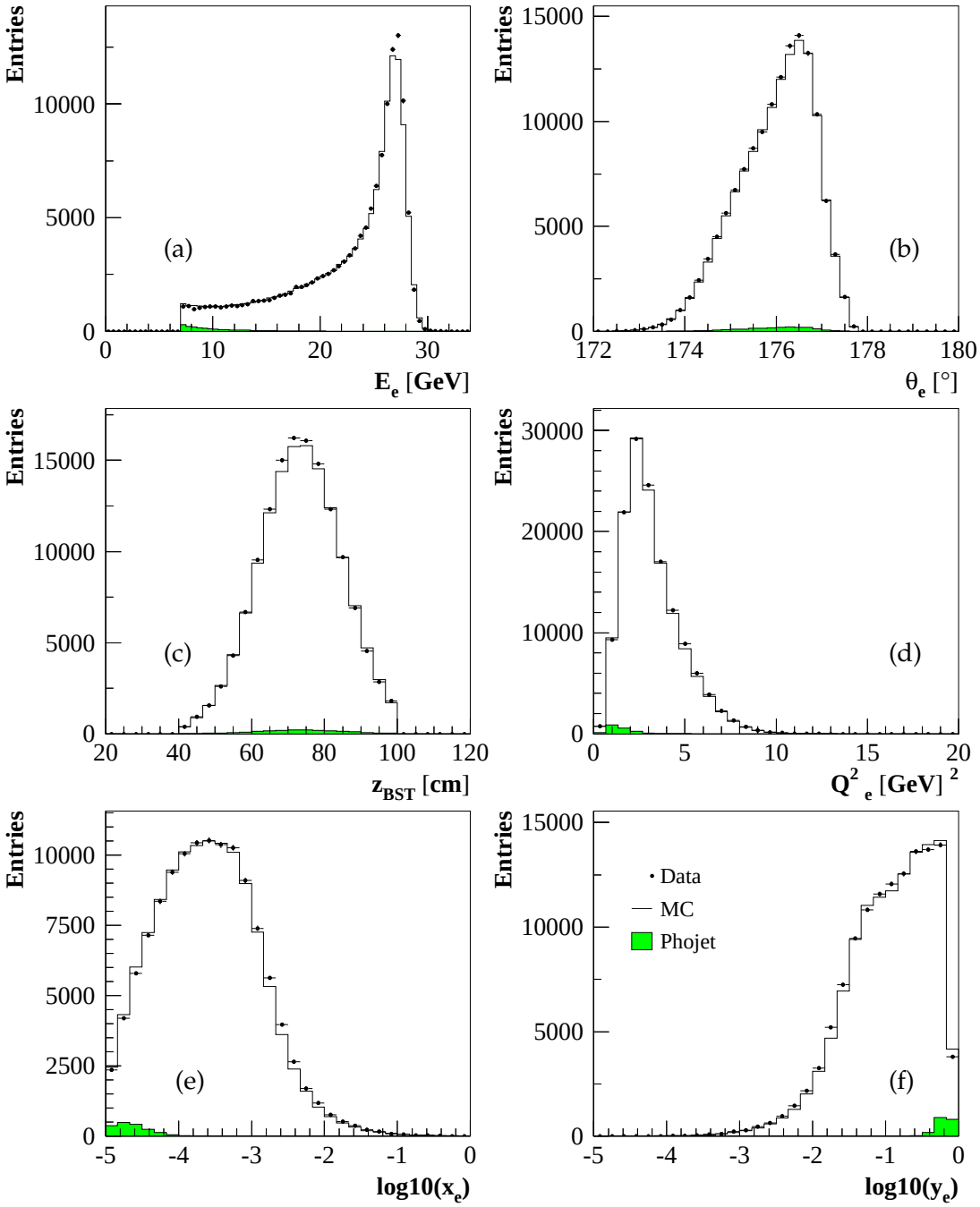

Figure 6.11: Control distributions of (a) energy (b) angle of the scattered electron (c) vertex position. (d) Q^2 (e) x (f) y reconstructed with the electron method. The MC is normalized to the luminosity of the data $+5\%$ (see text)

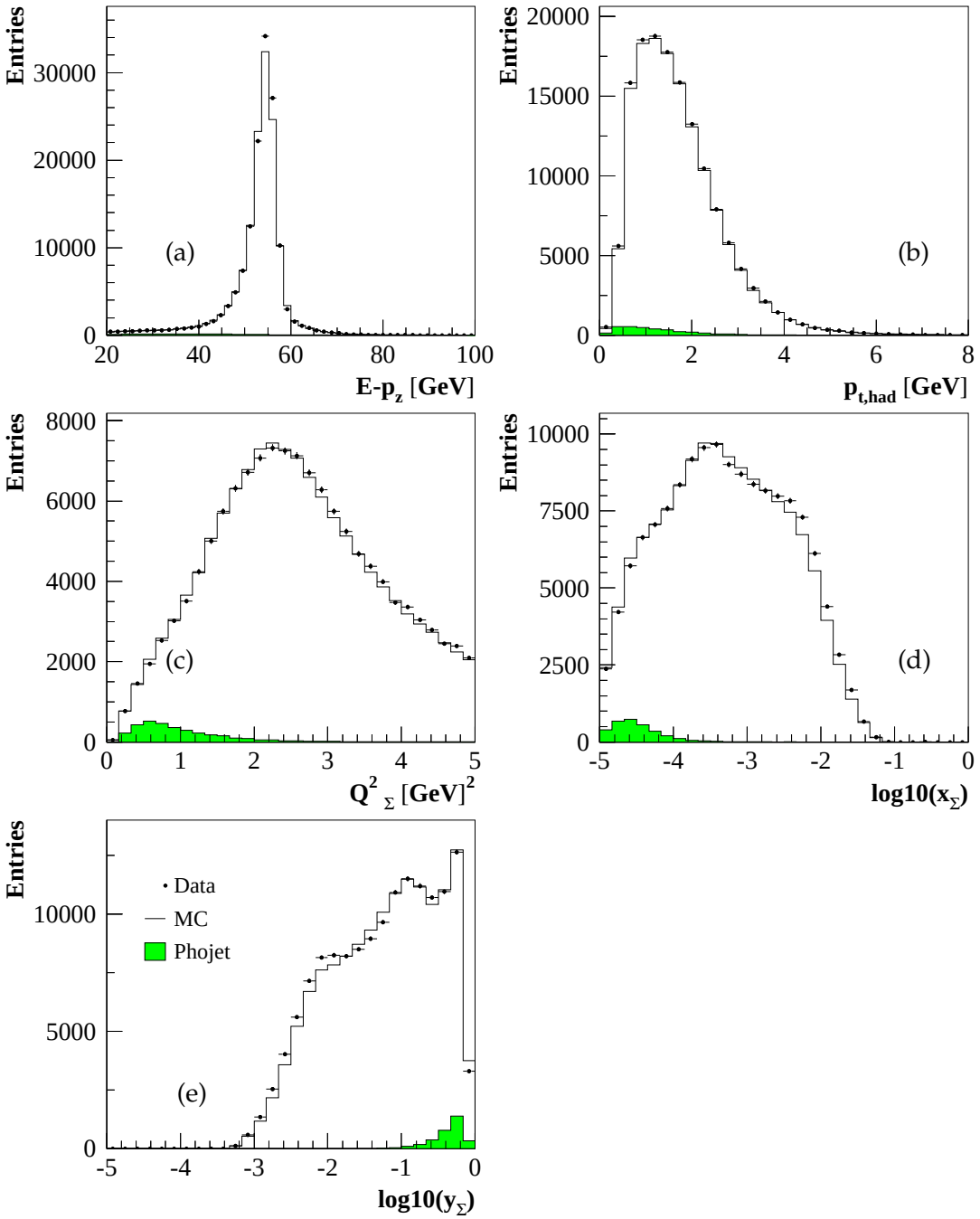

Figure 6.12: Control distributions of (a) $E - p_z$ (b) the transvers momentum of the hadrons $p_{t,had}$. The kinematical variables (c) Q^2 (d) x_Σ and (e) y_Σ reconstructed with the Σ method. The MC simulation is normalized to the luminosity of the data $+5\%$ (see text)

6.5 Cross section determination

The DIS cross section is measured by counting the number of events in a $x - Q^2$ grid. This number represent the integral of the double differential cross section over the kinematic interval. The cross section is given by:

$$\frac{d^2\sigma(x,Q^2)}{dxdQ^2} = \frac{N_{data} - N_{background}}{AL}\frac{1}{\epsilon}\frac{1}{1+\delta}\beta_{BC} \tag{6.6}$$

where:

- N_{data} is the number of total events selected in the $x - Q^2$ bin
- $N_{background}$ represent the background events
- A denotes the detector acceptance which is calculated with the MC, as:

  $$A = \frac{N_{rec}}{N_{gen}}$$

  being N_{rec} and N_{gen} the reconstructed and generated events in the particular bin.
- L is the integrated luminosity of the selected runs.
- ϵ are additional detector efficiency corrections obtained from data which were not included or not correctly described in the MC. In this particular case, this are the trigger efficiency of *S0* [100].
- δ represents the radiative corrections, calculated as,

  $$\delta = \frac{\sigma^{full}}{\sigma^{Born}} - 1$$

  where σ^{full} and σ^{Born} denotes the full and Born cross sections.
- β_{BC} are the bin center corrections which have to be applied in order to take the maximun variation of the cross section over the bin size and to obtain the cross section at the bin central value

  $$\beta_{BC} = \frac{d^2\sigma_{Born}}{dxdQ^2}\frac{1}{\sigma_{Born}}$$

The cross section measurement is significantly simplified if the MC already contains the radiative corrections. In such case $N_{gen} = \sigma_{full}L_{MC}$ and therefore the cross section formula given in

Eq. 6.6 can be written as:

$$\frac{d^2\sigma(x,Q^2)}{dxdQ^2} = \frac{N_{data} - N_{background}}{N_{rec}} \frac{L_{MC}}{L} \frac{d^2\sigma_{Born}}{dxdQ^2} \frac{1}{\epsilon} \tag{6.7}$$

since:

$$\begin{aligned} \frac{1}{A}\frac{1}{1+\delta}\beta_{BC} &= \left[\frac{N_{gen}}{N_{rec}}\right]\left[\frac{\sigma_{Born}}{\sigma_{full}}\right]\left[\frac{d^2\sigma_{Born}}{dxdQ^2}\frac{1}{\sigma_{Born}}\right] \\ &= \frac{L_{MC}}{N_{rec}}\frac{d^2\sigma_{Born}}{dxdQ^2} \end{aligned}$$

The Monte Carlo method is applicable just in case the MC already contains the radiative corrections and the relevant measured distributions are described by the MC. Thus, it is important to perform detailed studies on the description between the MC and the data for all measured quantities. This involves calibration, alignment and efficiency corrections. In chapter 4 and 5 it was in detail explained how the calibration of the H1 calorimeter were performed to the shifted vertex data. The alignment of the H1 detector was studied in [100], while the BST efficiency were studied in [106, 105].

6.5.1 Bin selection

The binning used in this analysis is the same that was defined to perform the DIS cross section measurement for the 1995 data. The binning is chosen as a non-equidistant grid, mainly in the $x-Q^2$ plane. Only in case the event has a value of y greater than 0.6 a $y-Q^2$ binning is chosen. This procedure is performed to profit from the statistic of the high y events.

high boundary	low boundary	bin center
0.85	0.75	0.8
0.75	0.6	0.675

Table 6.4: Boundary definition for the $y - Q^2$ binning

In Fig.6.13 is shown the Q^2-x plane together with the bin definition. A trapezoidal shape is observed for each Q^2 bin located in the lowest values of x. This trapezoidal bins are defined in a y-Q^2 grid, with the boundaries defined in Table 6.5.1. The rectangular grid in y, Q^2 is transformed to a trapezoid area in x and Q^2.

The statistics accumulated for each bin for the shifted vertex data is shown in Fig. 6.13, using

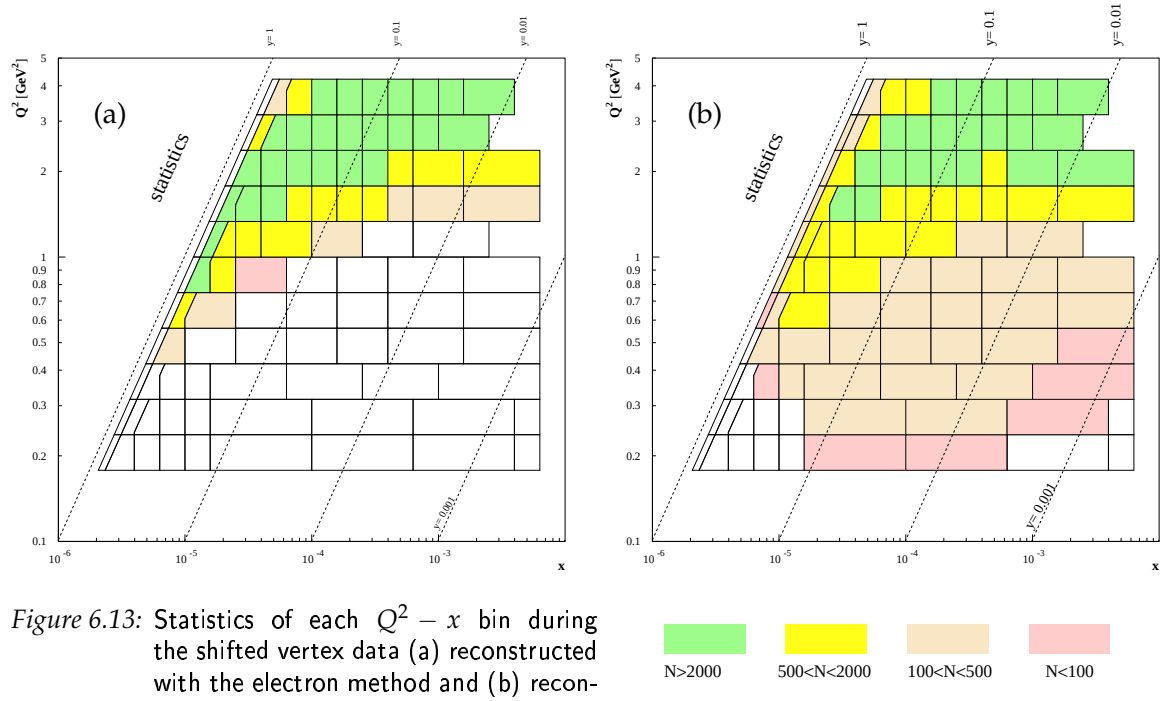

Figure 6.13: Statistics of each $Q^2 - x$ bin during the shifted vertex data (a) reconstructed with the electron method and (b) reconstructed with the Σ method

either the electron or the Σ method. From Fig. 6.13, it follows that the electron and the Σ method have comparable statistics for "high" Q^2 values and x around 10^{-5}. For higher values of x at low Q^2, no events are reconstructed with the electron method due the $E - p_z$ cut imposed to reduce the influence of radiative events, for which the electron method leads to a wrong reconstruction. The $E - p_z$ cut is not necessary for the Σ method, allowing therefore to access higher values of x for low values of Q^2.

Besides an equally distribution of the statistics, the aim of the binning is also to have a minimal migration of events between the bins. A bad adjustement of the bin size can cause migrations from bin to bin and therefore the cross section measurement can be influenced. In order to control the migration of the events between the bins, the *purity* and *stability* value for each bin is studied.

The purity and stability value are defined as:

$$Purity = \frac{N_{rec\&gen}}{N_{rec}} \qquad Stability = \frac{N_{rec\&gen}}{N_{gen}} \tag{6.8}$$

where N_{rec} and N_{gen} are the numbers of events reconstructed and generated in a particular bin. $N_{rec\&gen}$ represents the number of events which are reconstructed *and* generated in the same

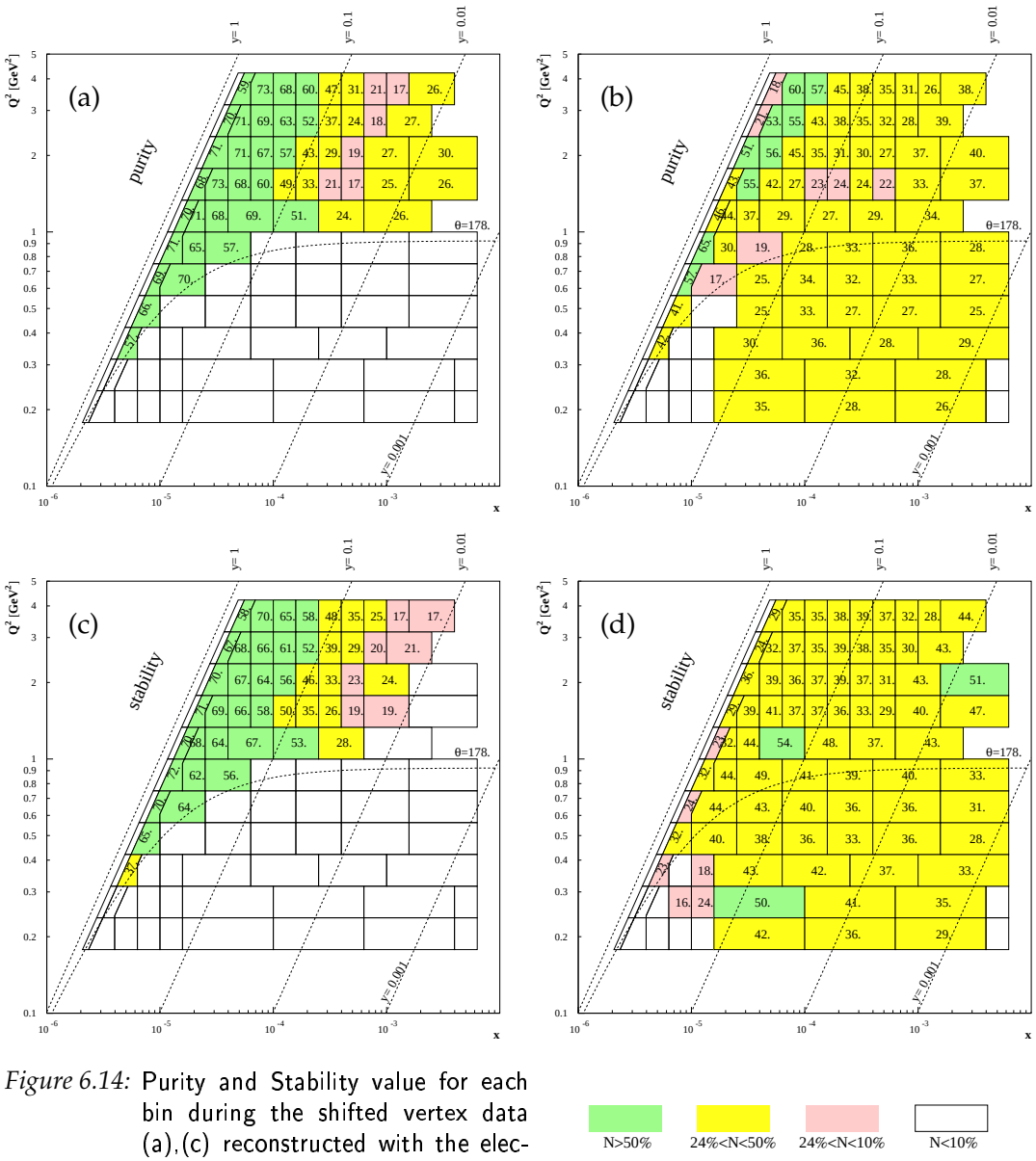

Figure 6.14: Purity and Stability value for each bin during the shifted vertex data (a),(c) reconstructed with the electron method and (b),(d) reconstructed with the Σ method

bin.

The purity is a measure for the migration of events coming from adjacent bins into the studied bin, while the stability controls the migration of events out of the bin. The values of both quantities are by definition restricted to the interval 0 to 1. In Fig. 6.14, the purity and stability values in per cent for each bin are presented. Fig. 6.14 (a) and (c) show the purity and stability obtained using the electron method, while in Fig. 6.14 (b) and (d) the purity and stability

values obtained with the Σ method are presented. From this plots, one can see that the electron method has values of purity and stability between 40% and 70%. The Σ method, in contrary has lower values, between 25% and 50%.

The differential cross section is measured in each bin only in case the values of the purity and stability are greater than 25%. In the kinematical region where the electron and the Σ method overlap, the method having higher values of stability and purity is chosen.

Although the value of purity and stability for the Σ method are lower than the values of the electron method, the Σ method extends the measurement to higher values of x and lower values of Q^2. In Fig. 6.14, is also shown the acceptance of the BST when the angle of the scattered electron has its maximal value ($\theta \approx 178^\circ$). One can see, that there are events which are localized below the acceptance line, those events are ISR events. The purity and stability values of the ISR events are greater than 25%, therefore the measurement of the cross section should be possible. Thus before to present the cross section measurement, the reconstruction of the incoming energy for the radiative events is in the next section in detail studied.

6.5.2 Non-tagged ISR analysis

For the electron method the ISR events are efficiently removed using the $(E - p_z)_{tot} > 35\,\text{GeV}$ cut. Nevertheless, the $(E - p_z) > 35\,\text{GeV}$ cut is not performed in case the kinematical variables are reconstructed with the Σ method. In this case the ISR event are used to enlarge the accesible phase space.

In this analysis the radiated photon is *not directly detected* in the photon detector of the luminosity system. The identification of the initial state radiation relies mainly on the recontruction of the $(E - p_z)_{tot}$. One important check to be performed is the reconstruction of the incoming energy E_{inc}.

As was already mentioned in Chapter 3, the Σ-method uses the longitudinal momentum conservation to define the event kinematic, therefore the

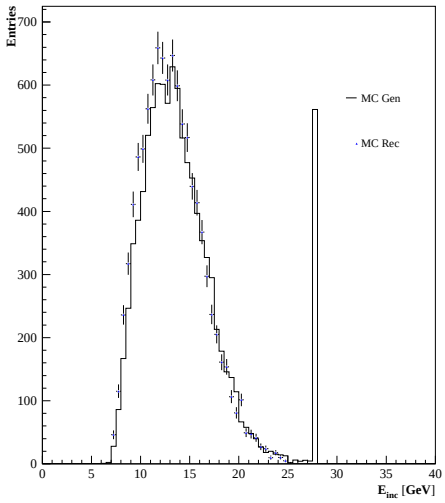

Figure 6.15: Comparison between generated and reconstructed incoming energy for ISR events having $Q^2 < 1.2\,\text{GeV}^2$.

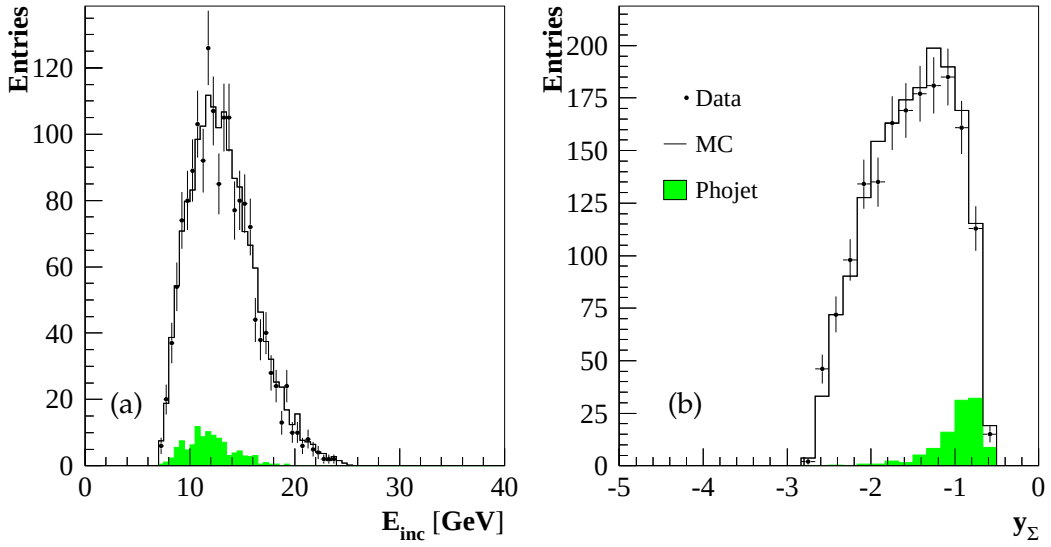

Figure 6.16: Control distributions for ISR events having $Q^2 < 1.2\,\mathrm{GeV}^2$. (a) The energy of the incoming electron. (b) The kinematical variable y_Σ

incoming energy can be reconstruced as:

$$E_{inc} = \frac{(E - p_z)_{had} + (E - p_z)_{el}}{2} \tag{6.9}$$

For MC one can verify, if the reconstructed energy of the ISR events agree with the generated one. In Fig. 6.15 the distribution of the reconstructed and the generated energy of the incoming electron are compared. The reconstructed incoming energy E_{inc} is calculated with Eq. 6.9 and is illustrated with the poins in Fig. 6.15, while in solid line is shown the incoming energy from the generator level. Only events with $Q^2 < 0.85\,\mathrm{GeV}^2$ and having values of x in the interval $5 \cdot 10^{-5} < x < 10^{-3}$ are shown. The selected events are located in bins where the values of purity and stability are higher than 25%. In such way the contribution from ISR events is high. On generator level the energy of the radiated photon is substracted from the energy of the incoming electron in case the event was explicitly generated as a ISR event. A good agreement between the generated and reconstructed energy of the incoming electron for the main kinematic region is observed.

A pronounced peak is observed in the incoming energy E_{inc} distribution presented in Fig. 6.15, those events are 5.5% of the whole statistic and are non ISR events reconstructed with small $(E - p_z)_{had}$. However, most of the events are good described by the MC simulation. The contribution of such non-radiative events becomes higher for values of $x < 10^{-5}$ and $Q^2 < 0.5\mathrm{GeV}^2$,

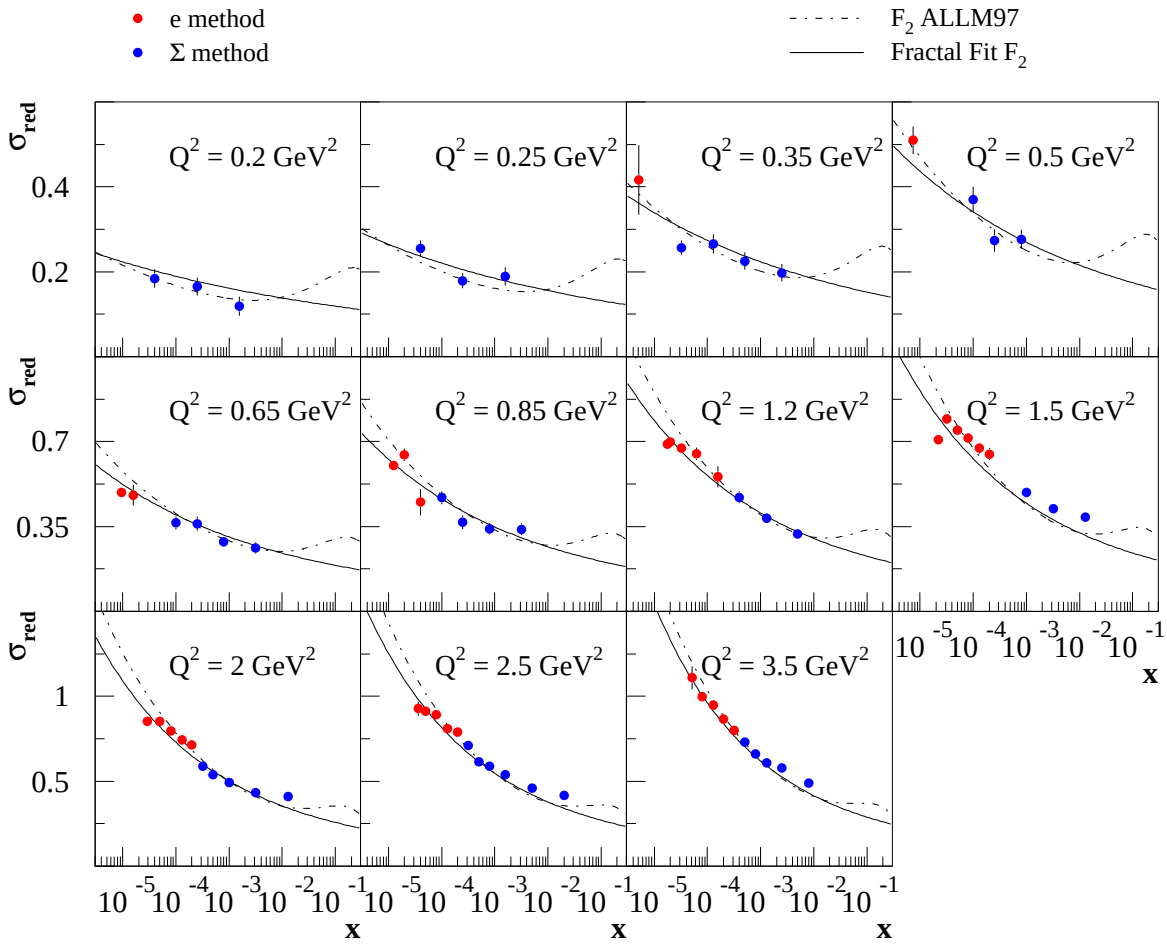

Figure 6.17: Cross section measurement as function of x for different Q^2 values. Red points were reconstructed by the electron method, blue poins with the Σ method. Only statistical errors are shown

leading to lower values of stability and purity (see Fig. 6.14 (b) and (d)).

In Fig. 6.16 (a) and (b) are shown the energy of the incoming electron and the kinematical variable y_Σ for data and MC for events with $Q^2_\Sigma < 1.2\,\mathrm{GeV}^2$. The MC simulation is in good agreement with the data.

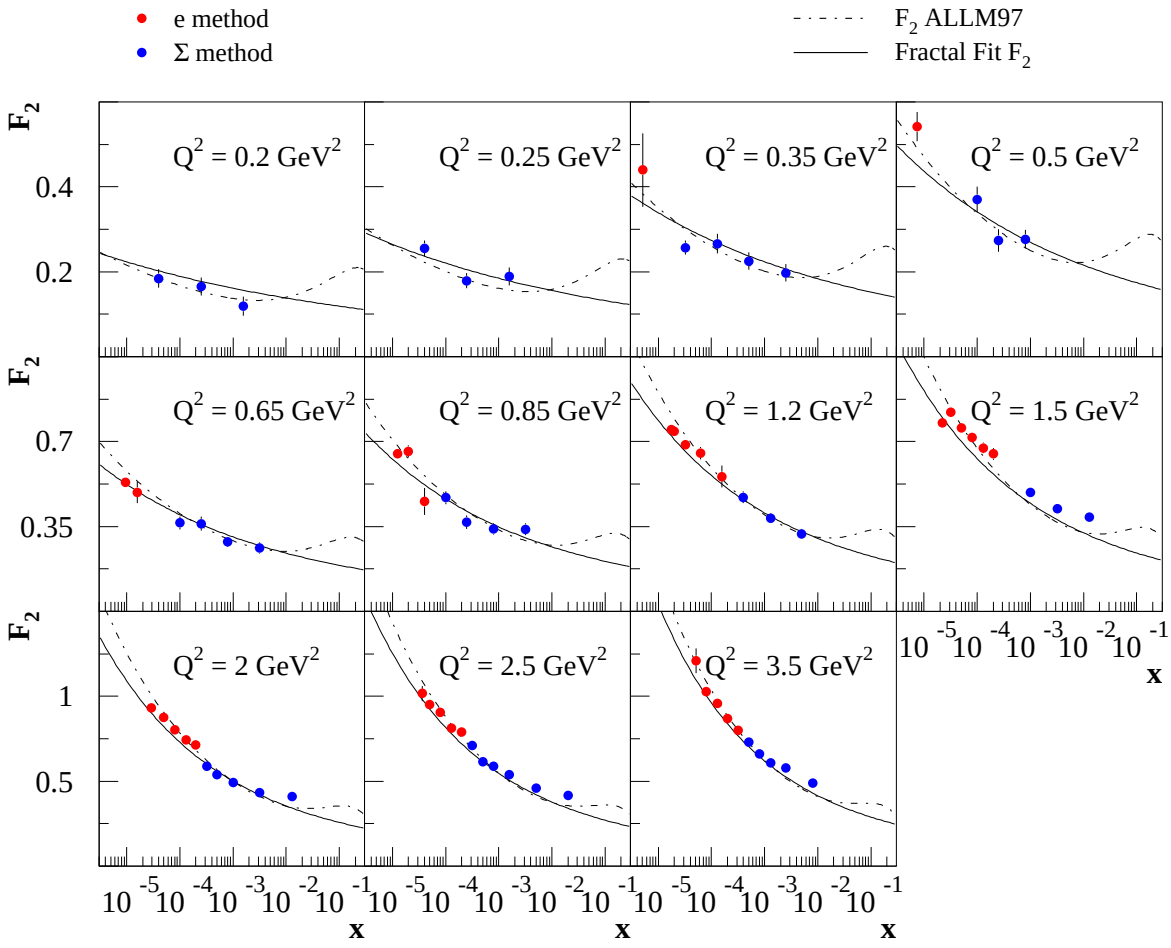

Figure 6.18: The proton structure function F_2 as function of x for different Q^2 values. The dashed line correspond to the ALLM97 fit [33], while the full line is the expectation from the Fractal fit [36]

6.6 Cross Section Measurement and Extraction of F_2

The cross section is measured following Eq.6.7. The *full* cross section from the MC uses the proton structure functions F_2 from the fractal fit [36] and from the ALLM97 [33] parametrizations, while the F_L contribution is taken from the dipole model [34]. A similar Eq. to 6.7 is obtained for the reduced cross section (see Eq. 1.7).

In Fig. 6.17 is shown the reduced cross section as a function of x in different Q^2 bins. The points

determined by the electron method are presented in red, while the points measured using the Σ method are marked in blue. The electron method is used up to values of $x \approx 10^{-4}$, while the Σ method cover the measurement up to values of $x \approx 10^{-2}$.

The errors presented in Fig. 6.17 are only statistical errors. The radiative points have statistical errors which vary between $10\% - 5\%$ for the lowest Q^2 bins and $2\% - 3\%$ for the high $Q^2 > 2\,\mathrm{GeV}^2$ region. The systematics errors are presented in the next section.

The proton structure function F_2 is extracted from the measured cross section and the prediction of F_L from the dipole model.

$$F_2 = \sigma_{red} + \frac{y^2}{Y_+} F_L \tag{6.10}$$

The measurement of F_2 is shown in Fig. 6.18, where also only stastistical errors are presented.

6.7 Systematic Errors

The measured cross section and the extraction of F_2 is influenced by systematic effects, some of which were derived in chapter 4 and 5. There are two types of systematic uncertainties, known as uncorrelated and correlated uncertainties.

The correlated uncertainties are global normalization uncertainties which affect as a whole the measurement. This are for example uncertainties of the luminosity, the trigger efficiency and radiative corrections. The uncorrelated uncertainties result from the implemented mechanism used to reconstruct the kinematical variables, this involves for example energy scale uncertainties, noise substraction procedures and angular measurements.

Uncorrelated errors influence the measured values independent of each other. Many systematic errors are partly correlated and partly uncorrelated. In the following the global normalization uncertainties will be treated as correlated, while all other will be treated as fully uncorrelated. In Table 6.5 are summarized all the uncorrelated and correlated sources which will be used to determine the total systematic error.

In order to estimate the influence of the uncorrelated and correlated uncertainties on the measurement, the values of all relevant quantities were varied within their uncertainties in positive and negative direction. After varying the relevant quantities, the kinematical variables are recalculated and the measurement of the cross section or F_2 extraction is performed again. The

Uncorrelated error		
Source	value	Reference
Luminosity	2.2%	[61]
Trigger Efficiency	0.5%	[100]
Radiative corrections	0.5%	[106]
BST efficiency	2%	[105, 106]
Correlated error		
Source	value	Reference
angle θ_e	0.2mrad	[106]
Electron Energy	0.02% at 27.5 GeV 1% at 2.5GeV	see chapter 4
Hadronic energy	10% at $y = 10^{-3}$ 2% at $y = 0.01$	see chapter 5
LAr noise	10%	see chapter 5
Hadronical SpaCal	350 MeV	see chapter 5
γp Background	15%	[105, 106]

Table 6.5: Systematic uncertainties of the DIS cross section measurement

deviation of the "varied" measurement from the original value is treated as the systematic uncertainty caused by the particular error source δ. The total error δ_{tot} will be computed as the quadratic summation over all error sources listed in Table 6.5 and the statistical error.

$$\delta_{tot} = \sqrt{\delta^2_{stat} + \delta^2_{corr} + \delta^2_{uncorr}} \tag{6.11}$$

where $\delta_{stat}, \delta_{corr}$ and δ_{uncorr} are the statistical, correlated and uncorrelated errors respectively. Following the table 6.5 δ_{corr} and δ_{uncorr} are calculated as:

$$\delta_{corr} = \sqrt{\delta^2_{ee} + \delta^2_{\theta} + \delta^2_{LAr} + \delta^2_{Noise} + \delta^2_{HadSpaCal} + \delta^2_{\gamma p}}$$

$$\delta_{uncorr} = \sqrt{\delta^2_{trigger} + \delta^2_{Luminosity} + \delta^2_{BST} + \delta^2_{rad-corr}}$$

Fig. 6.19(a) shows an example of the variations of F_2 in case the energy of the scattered electron E_e is changed according its uncertainty to the positive and negative direction:

$$E^{\pm}_e = E_e(1 + \Delta^{\pm})$$

where $\Delta^{\pm}$ is defined as:

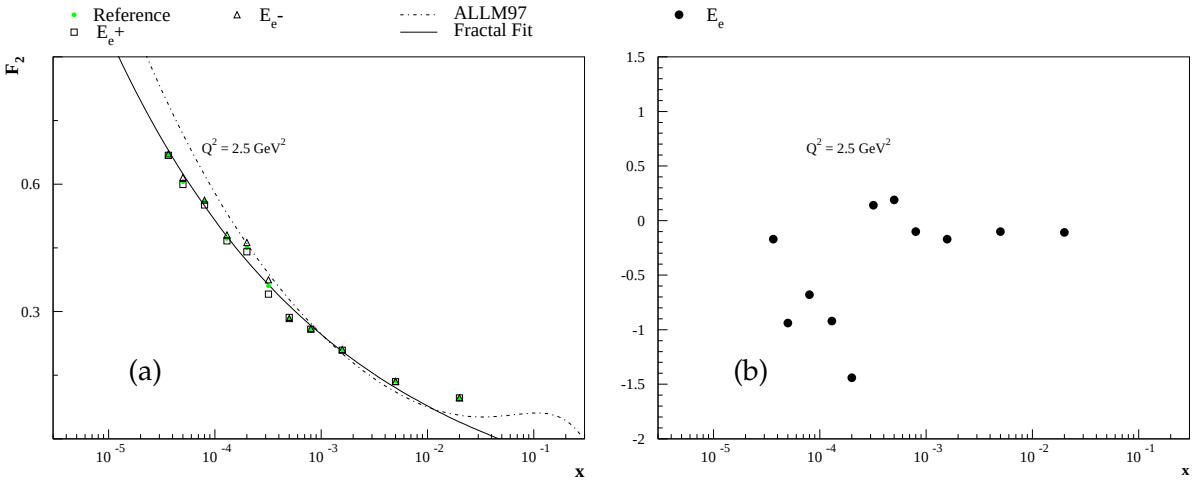

Figure 6.19: (a) Variation of the F_2 points for $Q^2 = 2.5\,\text{GeV}^2$ in case the energy of the scattered electron is moved according its uncertainty. (b) Systematic error due to the energy uncertainty for $Q^2 = 2.5\,\text{GeV}^2$.

$$\Delta^{\pm} = \left[(\Delta E_{kin})^{\pm} + \frac{(\Delta E_{kin})^{\pm} - (\Delta E_{\pi^0})^{\pm}}{E_{kin} - E_{\pi^0}} (E_e - E_{kin}) \right]$$

$\Delta E_{kin} = 0.02\%$ and $\Delta E_{\pi^0} = 1\%$ are the uncertainties of the energy measurement at kinematic peak and at π^0 energy, respectively. The systematic error for this particular $Q^2 = 2.5\,\text{GeV}^2$ bin due to the energy measurement uncertainty varies between 0.2% and 1.5% (see Fig. 6.19(b)).

In Fig. 6.20 is shown the proton structure function F_2 as function of x for different Q^2 bins with the total systematic error. For $Q^2 < 1.5\,\text{GeV}^2$ the measurement has a total error which varies between $5\% - 15\%$. For $Q^2 > 1.5\,\text{GeV}^2$ the total error vary between $2\% - 4\%$. The values of the cross section, F_2 and the error sources are summarized in Appendix A.

The comparison of the measurement performed in this analysis with the previous analysis is shown in Fig. 6.21. One can see that the measurements agree in shape in the overlap bins. The present analysis extend the phase space to lower values of $Q^2 = 0.2$ and $0.25\,\text{GeV}^2$. The present measurement is 5% higher than the presented in [105]. This discrepancy can be traced back to a wrong luminosity value used in [105].

In Fig. 6.22 is shown the comparison of the measured points of this analysis with the published data of H1 performed with shifted vertex data taken in the year 1995. Good agreement in normalization is found between the analysis here presented and the published measurement. The systematical errors of this analysis, for values of $Q^2 > 2\,\text{GeV}^2$ are reduced by a factor of

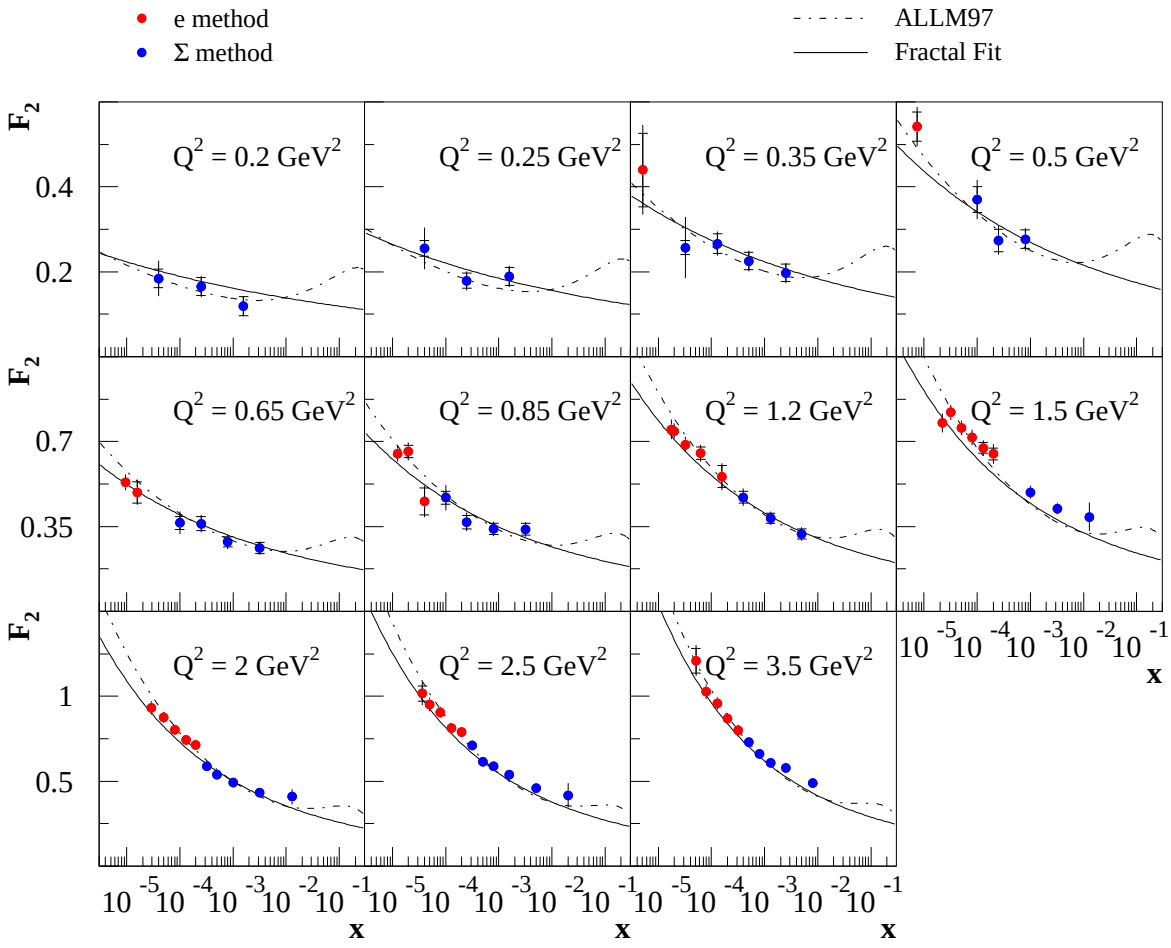

Figure 6.20: The proton structure function F_2 as function of x for different Q^2 values.The inner error bars correspond to the statistical uncertainty while the outer error bars show the total error obtaining by adding statistical and systematical uncertainties in quadrature. The dashed line correspond to the ALLM97 fit, while the full line is the expectation from the Fractal fit.

two, in comparison with the previous shifted vertex data. The measurement for $Q^2 < 2\,\mathrm{GeV}^2$ have total errors comparable to the 1995 shifted vertex measurement.

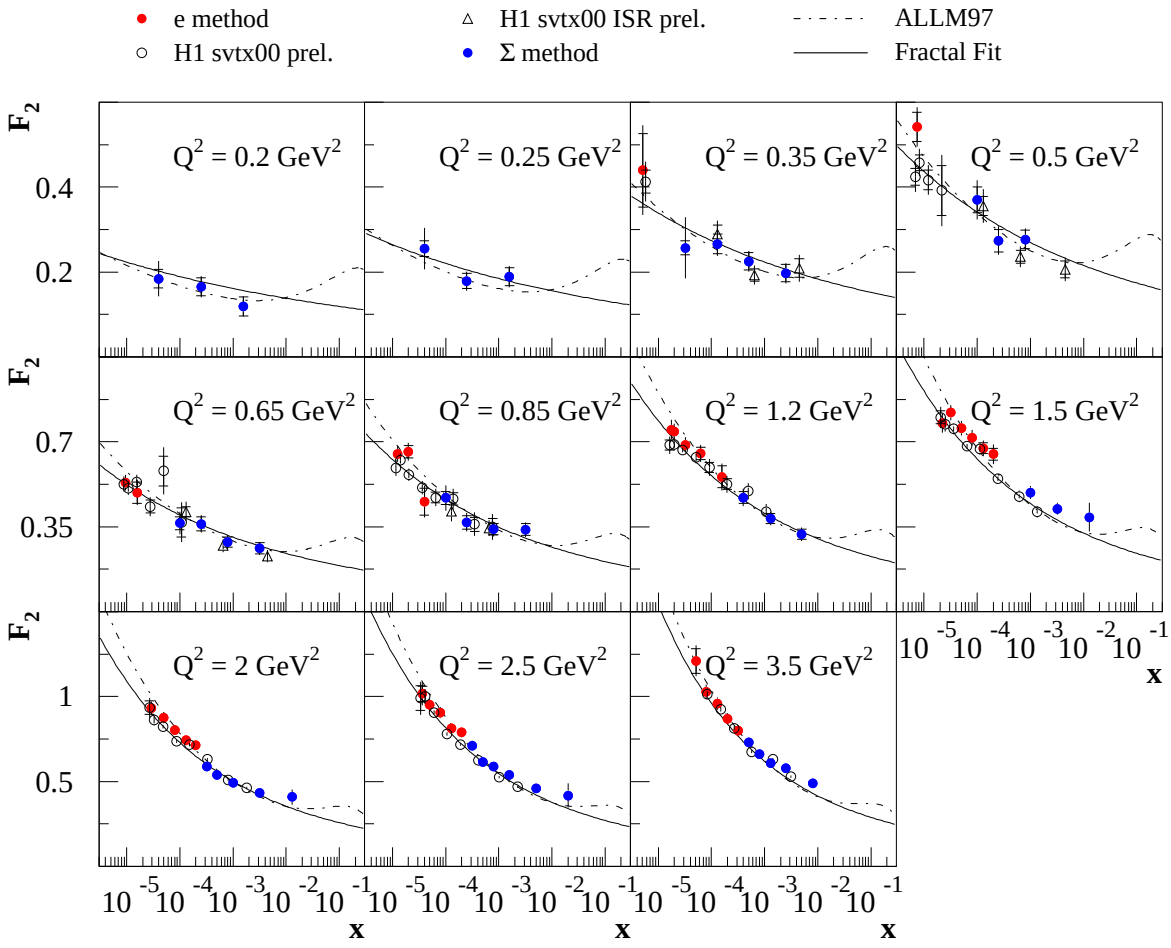

Figure 6.21: Comparison between the measurement of the proton structure function F_2 of the present analysis and the preliminary performed in [105] (open points). The dashed line correspond to the ALLM97 fit, while the full line is the expectation from the Fractal fit.

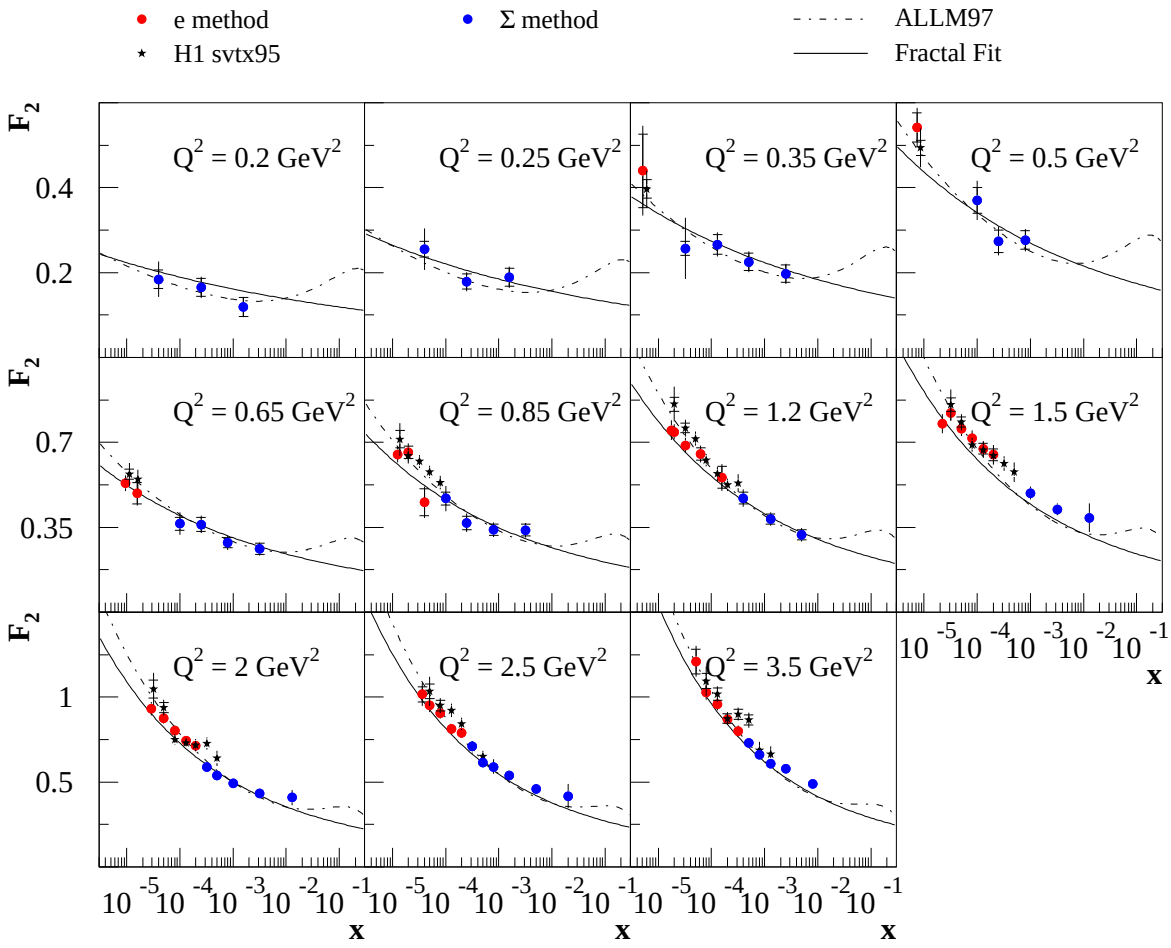

Figure 6.22: Comparison between the measurement of the proton structure function F_2 of the present analysis and the measurement of H1 performed with shifted vertex data in the year 1995. The dashed line correspond to the ALLM97 fit, while the full line is the expectation from the Fractal fit.

Summary

The measurement of the inclusive DIS cross section and the extraction of the proton structure function F_2 in the kinematical region of $0.2 < Q^2 < 3.5\,\mathrm{GeV}^2$ for low values of $9.5 \times 10^{-6} < x < 8.0 \times 10^{-3}$ have been performed. The data sample analysed correspond to a special data taking period where the interaction point of the ep scattering was moved from its nominal position in order to access low values of Q^2.

In order to minimize the total error of the measurement over the accessed phase space, usually two kinematical reconstruction methods are employed, the electron and the Σ method. The electron method is used in this analysis up to values of $x < 10^{-4}$, while the Σ method is used for the interval $10^{-4} \leq x \leq 8.0 \times 10^{-3}$. Both methods are influenced by several systematic errors which were studied in detail to determine the total error of the F_2 measurement. The present analysis concentrated on the understanding of the uncertainty of the energy measurement of the scattered electron and of the energy flow of the hadronical final state.

Since for ep collision at low values of Q^2, the electron is scattered into the backward region of the H1 detector, a precise calibration of the electromagnetic part of the SpaCal was performed. The uncertainty of the energy measurement is found to be 0.02% for energies of the scattered electron close to the incoming electron energy $E^0_{inc} \approx 27.5\,\mathrm{GeV}$, while 1% is obtained for small energies around $E \approx 2\,\mathrm{GeV}$. Using a linear interpolation of the uncertainty of the energy measurement, the resulting systematic error of the F_2 measurement varies between 0.5% and 4%.

Using the energy measurement of the scattered electron as the reference scale, the energy flow of the hadronic final state was studied in terms of its transverse and longitudinal momentum. Since the Σ method uses the reconstruction of all particles building the final state, detailed studies of the calorimeter noise and its influence on the reconstruction of the kinematical variables were performed. The noise originating from the beams and the electronics circuits of the LAr calorimeter was found to have a negligible influence on the kinematical reconstruction. The noise substraction algorithm was found to have an influence of 10% over the accessed phase space. The uncertainty of the energy flow identified as coming from the real ep collision was assigned to 10% at $y = 10^{-3}$ and to 2% at $y = 10^{-2}$. The correlated systematic error of the F_2

measurement due to the uncertainty of the hadronic energy measurement accounts to values between 0.5% and 4%.

The cross section measurement in the same kinematical region and using the same data sample was performed in [100], but the CTD and the BDC were used instead of the BST in order to reconstruct the angle of the scattered electron coming from the ep collision. The cross section measurement and the proton structure function performed in [100] and the one derived in this thesis are in good agreement.

The measurement of the proton structure function here presented agrees with the previous measurement of H1 using shifted vertex data taken in the year 1995. The total error of the measurement presented here have a higher precision than the previous shifted vertex data for values of $Q^2 > 1.5\,\mathrm{GeV}^2$. The total error of the F_2 measurement achieves the same precision as the low Q^2 analysis of H1 using data of 1996 and 1997, having a total error which varies between $3\% - 4\%$ for values of $Q^2 > 2\,\mathrm{GeV}^2$ and $8\% - 15\%$ for $Q^2 < 2\,\mathrm{GeV}^2$.

Appendix A

Tables

Q^2 [GeV]^2	x	y	σ_{red}	R	F_2	δ_{tot}%	δ_{stat}%	δ_{unc}%	δ_{cor}%	δ_{ee}%	δ_{θ}%	δ_{LAr}%	δ_{Noise}%	δ_{HadSpa}%	$\delta_{\gamma p}$%
0.2	3.98E-05	4.96E-02	1.83E-01	0.16288	0.18257	22.55	11.95	10.36	16.07	4.29	0.48	-0.2	-0.17	-9.76	-12.02
0.2	2.51E-04	7.86E-03	1.64E-01	0.24344	0.16382	15.17	12.8	6.49	4.91	2.26	0.42	-0.39	-3.42	-2.14	-1.56
0.2	1.58E-03	1.25E-03	1.18E-01	0	0.11784	20.51	18.57	7.58	4.28	0.22	-2.58	0.14	0.33	-3.38	-0.14
0.25	3.98E-05	6.20E-02	2.53E-01	0.14903	0.25297	19.21	7.2	6.87	16.43	3.01	-1.17	-6.28	-1.3	-6.67	-13.19
0.25	2.51E-04	9.82E-03	1.77E-01	0.13273	0.17745	12.53	9.81	5.14	5.86	-1.47	-0.09	0.61	-4.77	-2.73	-1.26
0.25	1.58E-03	1.56E-03	1.87E-01	0	0.18726	13.22	11.11	5.69	4.37	0.43	1.28	-1.51	-3.3	-2	-0.29
0.35	5.12E-06	6.74E-01	4.13E-01	0.14863	0.43622	24.09	19.61	12.99	5.22	4.43	-0.37	1.11	0	0.55	-2.44
0.35	3.20E-05	1.08E-01	2.54E-01	0.23396	0.25472	28.01	6.39	7.96	26.08	2.24	0.22	-7.11	-0.75	-10.13	-22.84
0.35	1.30E-04	2.66E-02	2.64E-01	0.18607	0.2639	10.78	8.51	4.9	4.45	-0.06	-1.62	-1.85	-1.18	-2.7	-2.24
0.35	5.00E-04	6.90E-03	2.23E-01	0.2289	0.22333	10.66	8.91	4.69	3.5	-0.83	-0.58	-0.69	-2.84	-1.55	-0.48
0.35	2.51E-03	1.38E-03	1.96E-01	0	0.19581	12.1	10.31	5.04	3.8	-1.48	0.63	0.06	-3.25	-1.16	-0.04
0.5	7.32E-06	6.74E-01	5.05E-01	0.1704	0.5375	8.57	6.34	4.84	3.14	0.36	-0.23	1.04	-0.29	1.72	-2.35
0.5	1.00E-04	4.93E-02	3.67E-01	0.19643	0.36701	12.63	8.19	5.27	8.04	-0.54	1.2	-2.21	0.21	-6.66	-3.68
0.5	2.51E-04	1.96E-02	2.72E-01	0.22946	0.27174	12.23	9.67	4.85	5.71	0.05	-0.51	1.17	-4.39	-3.28	-1
0.5	8.00E-04	6.16E-03	2.74E-01	0.23073	0.27438	9.6	7.83	4.36	3.45	-0.24	-0.84	0.18	-3.28	-0.53	-0.17
0.65	9.52E-06	6.74E-01	4.87E-01	0.2271	0.52703	6.09	3.36	3.56	3.62	-0.18	0.35	1.1	-0.23	1.45	-3.1
0.65	1.58E-05	4.06E-01	4.75E-01	0.23473	0.48658	10.6	9.05	5.24	1.68	-0.45	-1.43	0.3	-0.06	0.41	-0.55
0.65	1.00E-04	6.41E-02	3.61E-01	0.26321	0.36136	12.71	7.29	5.08	9.09	-0.38	-1.09	-3.35	-0.01	-6.88	-4.76
0.65	2.51E-04	2.55E-02	3.59E-01	0.22431	0.35871	10.12	8.28	4.51	3.69	-0.08	-1.76	-1.72	-0.35	-2.65	-0.65
0.65	8.00E-04	8.01E-03	2.84E-01	0.28236	0.28432	10.68	7.6	4.18	6.22	-1.38	0.45	1.13	-5.92	-0.52	-0.17
0.65	3.20E-03	2.00E-03	2.59E-01	0	0.25861	10.22	8.91	4.6	2.01	-1.54	0.11	-0.46	1.16	-0.3	-0.06
0.85	1.24E-05	6.74E-01	5.96E-01	0.22734	0.64483	5.1	2.17	3.26	3.27	-0.26	-0.29	1.3	-0.11	1.25	-2.7
0.85	2.00E-05	4.19E-01	6.39E-01	0.20887	0.65385	5.52	3.97	3.62	1.29	-1.04	0.04	0.5	-0.12	0.37	-0.45
0.85	3.98E-05	2.11E-01	4.46E-01	0.30102	0.44897	14.29	12.13	6.27	4.23	-1.58	-3.88	0.55	-0.14	0	-0.11
0.85	1.00E-04	8.38E-02	4.65E-01	0.24776	0.46521	11.13	5.66	4.15	8.63	-2.11	0.05	-2.4	0.75	-7.43	-2.91
0.85	2.51E-04	3.34E-02	3.65E-01	0.28685	0.36554	10.08	7.52	4.28	5.17	0.46	-0.62	-1.46	-0.39	-4.79	-0.97
0.85	8.00E-04	1.05E-02	3.37E-01	0.272	0.33654	8.75	6.61	4	4.1	0.09	-1.01	1.07	-3.63	-1.19	-0.25
0.85	3.20E-03	2.62E-03	3.35E-01	0	0.33488	8.73	7.2	4.33	2.36	0.17	-0.81	1.95	-1.04	-0.14	-0.04
1.2	1.76E-05	6.74E-01	6.83E-01	0.25172	0.74433	5.32	2.18	3.25	3.61	-1.03	-0.11	1.3	-0.22	1.2	-2.96

continue in next page

Q^2 [GeV]^2	x	y	σ_{red}	R	F_2	δ_{tot}%	δ_{stat}%	δ_{unc}%	δ_{cor}%	δ_{ee}%	δ_{θ}%	δ_{LAr}%	δ_{Noise}%	δ_{HadSpa}%	$\delta_{\gamma p}$%
1.2	2.00E-05	5.92E-01	6.93E-01	0.24945	0.73704	4.27	2.46	3.25	1.26	-0.71	-0.28	0.4	-0.08	0.5	-0.76
1.2	3.20E-05	3.70E-01	6.68E-01	0.25398	0.68193	4.49	2.83	3.3	1.11	-1.02	0.19	0.17	-0.15	0.14	-0.28
1.2	6.31E-05	1.88E-01	6.44E-01	0.24106	0.64682	5.34	3.89	3.56	0.82	-0.67	-0.32	0.31	0.13	0	-0.03
1.2	1.58E-04	7.49E-02	5.50E-01	0.24986	0.55077	9.92	8.06	4.91	3.04	-2.78	1.17	0.38	0.19	0	0
1.2	3.98E-04	2.97E-02	4.66E-01	0.26121	0.46622	7.56	5.31	3.8	3.81	-2.23	-0.23	-0.58	-0.64	-2.96	-0.15
1.2	1.30E-03	9.10E-03	3.80E-01	0.33834	0.38049	7.12	5.19	3.74	3.12	-2.27	-0.48	0.95	-1.69	-0.79	-0.02
1.2	5.00E-03	2.37E-03	3.16E-01	0	0.31597	8.47	6.67	4.11	3.24	-1.72	-1.18	1.23	2.13	-0.34	-0.02
1.5	2.20E-05	6.74E-01	7.02E-01	0.28284	0.77167	5.02	2.2	3.22	3.16	-0.02	-0.97	1.21	-0.21	1.04	-2.54
1.5	3.20E-05	4.62E-01	7.87E-01	0.24687	0.81361	3.75	1.71	3.14	1.11	-0.67	-0.5	0.37	-0.11	0.31	-0.53
1.5	5.00E-05	2.96E-01	7.41E-01	0.25173	0.74996	3.84	1.96	3.17	0.93	-0.88	-0.1	0.25	-0.07	0.01	-0.09
1.5	8.00E-05	1.85E-01	7.08E-01	0.2463	0.71086	4.38	2.63	3.26	1.26	-1.19	-0.2	0.34	0	0	-0.02
1.5	1.30E-04	1.14E-01	6.67E-01	0.24269	0.66768	4.91	3.27	3.38	1.41	-1.33	-0.22	0.4	-0.15	0	-0.02
1.5	2.00E-04	7.40E-02	6.43E-01	0.23368	0.64332	6.11	3.67	3.48	3.42	-3.36	-0.41	0.43	-0.25	0	0
1.5	1.00E-03	1.48E-02	4.86E-01	0.22669	0.48637	5.38	3.05	3.34	2.92	-1.85	-0.82	0.7	-1.93	-0.45	0
1.5	3.20E-03	4.62E-03	4.20E-01	0.27881	0.42009	5.63	2.76	3.3	3.62	-1.34	-0.87	2.27	-2.32	-0.25	0
1.5	1.30E-02	1.14E-03	3.86E-01	0	0.38615	15.24	4.56	3.69	14.06	-1.36	-0.7	1.72	13.87	-0.22	0
2	2.93E-05	6.74E-01	8.44E-01	0.26956	0.92455	4.29	1.98	3.16	2.12	-0.45	-0.92	0.82	-0.11	0.78	-1.47
2	5.00E-05	3.95E-01	8.46E-01	0.26253	0.86644	3.68	1.6	3.12	1.12	-0.62	-0.81	0.26	-0.16	0.11	-0.29
2	8.00E-05	2.47E-01	7.88E-01	0.26582	0.79468	3.66	1.64	3.12	1	-0.88	-0.38	0.26	-0.15	0	-0.05
2	1.30E-04	1.52E-01	7.35E-01	0.26372	0.7375	3.91	1.83	3.14	1.46	-1.41	0	0.36	-0.13	0	-0.01
2	2.00E-04	9.86E-02	7.07E-01	0.25392	0.70742	4.16	1.98	3.16	1.85	-1.75	-0.37	0.43	-0.1	0	-0.01
2	3.20E-04	6.16E-02	5.81E-01	0.29536	0.58156	4.56	2.16	3.17	2.48	-0.92	-0.68	-0.95	0.07	-1.98	-0.03
2	5.00E-04	3.95E-02	5.34E-01	0.3012	0.53368	4.4	2.43	3.19	1.82	-1.5	0.21	-0.52	-0.12	-0.86	-0.01
2	1.00E-03	1.97E-02	4.89E-01	0.29328	0.48871	4.26	1.88	3.14	2.18	-1.38	-0.14	0.58	-1.52	-0.41	-0.01
2	3.20E-03	6.16E-03	4.29E-01	0.32216	0.42862	5.17	1.65	3.13	3.78	-1.38	0.06	2.51	-2.47	-0.17	0
2	1.30E-02	1.52E-03	4.05E-01	0	0.40484	10.77	2.49	3.24	9.96	-1.26	-0.35	0.75	9.85	-0.16	0
2.5	3.66E-05	6.74E-01	9.20E-01	0.27271	1.00839	6.61	4.47	3.58	3.31	-0.17	-2.46	1.04	-0.18	0.99	-1.65
2.5	5.00E-05	4.93E-01	9.05E-01	0.27713	0.94423	4.07	2.17	3.17	1.36	-0.94	-0.62	0.34	-0.14	0.4	-0.54
2.5	8.00E-05	3.08E-01	8.85E-01	0.26673	0.89678	3.66	1.64	3.12	0.98	-0.68	-0.63	0.28	0.04	0.03	-0.13
2.5	1.30E-04	1.90E-01	8.02E-01	0.27407	0.80586	3.71	1.64	3.12	1.15	-0.92	-0.61	0.34	-0.05	0	-0.01

continue in next page

Q^2 [GeV]^2	x	y	σ_{red}	R	F_2	δ_{tot}%	δ_{stat}%	δ_{unc}%	δ_{cor}%	δ_{ee}%	δ_{θ}%	δ_{LAr}%	δ_{Noise}%	δ_{HadSpa}%	$\delta_{\gamma p}$%
2.5	2.00E-04	1.23E-01	7.82E-01	0.25789	0.78368	3.84	1.64	3.12	1.52	-1.44	-0.31	0.34	-0.15	0	-0.01
2.5	3.20E-04	7.71E-02	7.03E-01	0.26512	0.70393	4.13	1.75	3.13	2.04	0.14	-0.59	0.49	-1.16	-1.49	-0.01
2.5	5.00E-04	4.93E-02	6.09E-01	0.28826	0.60884	3.96	1.9	3.14	1.48	0.19	-0.94	-0.35	-0.73	-0.79	-0.01
2.5	8.00E-04	3.08E-02	5.83E-01	0.27136	0.58312	3.97	1.96	3.15	1.4	-0.1	-0.46	0.55	-1.14	-0.37	0
2.5	1.58E-03	1.56E-02	5.33E-01	0.27006	0.53251	4.46	1.45	3.11	2.84	-0.17	-0.5	1.2	-2.51	-0.17	0
2.5	5.00E-03	4.93E-03	4.55E-01	0.22286	0.45496	4.54	1.29	3.1	3.04	-0.1	-0.65	2.52	-1.57	-0.15	0
2.5	2.00E-02	1.23E-03	4.13E-01	0	0.41328	16.84	2.33	3.2	16.37	-0.11	-0.59	1.17	16.31	-0.13	0
3.5	5.12E-05	6.74E-01	1.10E+00	0.25508	1.20003	7.51	6.06	3.93	2.06	-0.72	-1.62	0.53	-0.04	0.47	-0.78
3.5	8.00E-05	4.32E-01	9.88E-01	0.282	1.01905	4.23	2.31	3.18	1.57	-0.8	-1.27	0.35	-0.11	0.15	-0.22
3.5	1.30E-04	2.66E-01	9.41E-01	0.27366	0.95075	3.83	1.8	3.14	1.26	-0.77	-0.93	0.35	-0.05	0	-0.05
3.5	2.00E-04	1.73E-01	8.56E-01	0.27998	0.85971	3.82	1.78	3.13	1.25	-1.04	-0.58	0.37	-0.11	0	-0.01
3.5	3.20E-04	1.08E-01	7.91E-01	0.27646	0.79226	4.02	1.8	3.14	1.76	-1.53	-0.75	0.4	-0.16	0	-0.01
3.5	5.00E-04	6.90E-02	7.23E-01	0.27794	0.72383	3.98	1.96	3.15	1.44	0.43	-0.68	-0.07	-0.88	-0.81	-0.01
3.5	8.00E-04	4.32E-02	6.56E-01	0.28134	0.65595	4.02	2.03	3.15	1.43	0.25	-0.6	0.33	-1.17	-0.41	0
3.5	1.30E-03	2.66E-02	6.03E-01	0.28191	0.60258	4.21	2.1	3.16	1.82	0.4	-0.86	0.43	-1.48	-0.22	0
3.5	2.51E-03	1.38E-02	5.74E-01	0.25054	0.57395	4.97	1.48	3.11	3.58	0.15	-0.51	1.81	-3.04	-0.14	0
3.5	8.00E-03	4.32E-03	4.84E-01	0	0.48361	4.24	1.39	3.11	2.53	0.3	-0.83	2.36	0.25	-0.11	0

Bibliography

[1] M. Gell-Mann, Phys. Lett. **8** (1964) 214.

[2] R. Feynmann, Phys Rev. Lett 23 (1969) 1415

[3] J. D. Bjørken, E. A. Paschos, Phys. Rev. **185** (1969) 1975.

[4] "Structure functions and small x Physics"
Lectures given at the XXI International Meeting on Fundamental Physics, Miraflores de la Sierra, Madrid, 9-15 May (1993)

[5] R. Devenish, A.Cooper-Sarkar, "Deep inelastic scattering", Oxford university press, (2004)

[6] J.I. Friedman and H.W. Kendall, Ann. Rev. Nucl. Science 22 (1972) 203

[7] J.G.H. de Groot et al, Z.Phys.C1:143,1979
D.J. Fox et al, Phys. Rev Lett 33 (1974) 1504

[8] P.C. Bosetti et al, Nucl. Phys. B142 (1978) 1

[9] Gargamelle Neutrino Collaboration, Nucl.Phys.B85:269,1975

[10] BBEC Collaboration, Nucl. Phys. B 203 (1982) 362

[11] D.J. Gross and F.Wilczek, Phys. Rev D8 (1973) 3633

[12] H.D. Politzer, Phys. Rev Lett 30 (1973) 1346

[13] G. Altarelli, G. Parisi, Nucl. Phys. B **126** (1977) 298

[14] V.N. Gribov and L.N. Lipatov Yad. Fiz 15(1972) 781 and 1218
Sov. J. Nucl. Phys 15 (1972) 438 and 675
Y.L Dokshitzer, Sov. Phys, JETP 46 (1977) 641 and 19

[15] C. G.Callan, D. J. Gross, Phys. Rev. Lett. **22** (1969) 156.

[16] E. Reya, Phys. Rep. **69** (1981) 196.

[17] M. Glück, E. Reya, A. Vogt, Eur. Phys. J. **C5** (1998) 461.

[18] A. D. Martin *et al.*, Eur. Phys. J. **C4** (1998) 463.

[19] H. L. Lai *at al.* [CTEQ Collaboration], Phys. Rev. **D55** (1997) 1280 [arXiv:hep-ph/9903282(1999)].

[20] P.D.Collins, "An introduction to Regge Theory and high energy physics", Cambridge Monographs on Mathematical Physics (Cambridge University press, 1977).

[21] C. Adloff *et al.* [H1 Collaboration], Eur. Phys. J. C **21** (2001) 33.

[22] C. Adloff *et al.* [H1 Collaboration], Eur. Phys. J. C **19** (2001) 269 [arXiv:hep-ex/0012052].

[23] C. Adloff *et al.* [H1 Collaboration], Eur. Phys. J. C **13** (2000) 609 [arXiv:hep-ex/9908059].

[24] J. Breitweg *et al.* [ZEUS Collaboration], Eur. Phys. J. C **12** (2000) 411 [arXiv:hep-ex/9907010].

[25] S. Chekanov *et al.* [ZEUS Collaboration], Eur. Phys. J. C **21** (2001) 443 [arXiv:hep-ex/0105090].

[26] A. C. Benvenuti *et al.* [BCDMS Collaboration], Phys. Let. B **223** (1989) 485.

[27] M. R. Adams *et al.* [E665 Collaboration], Phys. Rev. D **54** (1996) 3006.

[28] M. Arneodo *et al.* [New Muon Collaboration (NMC)], Nucl. Phys. B **483** (1997) 3.

[29] A. Donnachie and P.V. Landshoff, Phys. Lett. B **296** (1992) 227

[30] A. Donnachie and P.V. Landshoff, Z. Phys. C **61** (1993) 139

[31] H1 collaboration S. Aid et al, Z. Phys. C **69** (1995) 27

[32] H1 Collaboration, C. Adloff et al., Phys. Lett. B **520** (2001) 183 see also, J.Gayler Talk given at 32nd International symposium on multiparticle dynamics (ISMD) 2002, Alushta, Ukraine, 7-13 Sep 2002 [arXiv:hep-ex/0211051].

[33] Abramowicz, Levin, Levy and Maor, DESY-97 (1997) 251 [arXiv:hep-ph/9712415].

[34] K. Golec-Biernat and M.Wusthoff, Phys. Rev. D **59** (1999) 014017

[35] G.Cvetic, et al Eur. Phys. J C **20** (2001) 77

[36] T. Lastovic, Eur. Phys. J. C **24** (2002) 529
[arXiv:hep-ph/0203260].

[37] ZEUS Collaboration, J. Breitweg et al, Phys. Lett. B **487** (2000) 53

[38] Tomas Lastovicka for the H1 collaboration, "Measurement of the Deep Inelastic Scattering Cross Section at $Q^2 \approx 1\,\mathrm{GeV}^2$ with the H1 Experiment", International Europhysics Conference on High energy physics, EPS03, July 17-23, 2003, Aachen (Abstract 082)

[39] I. Abt *et al.* [H1 Collaboration], Nucl. Instrum. Meth. A **386** (1997) 310.

[40] I. Abt *et al.* [H1 Collaboration], Nucl. Instrum. Meth. A **386** (1997) 348.

[41] H1 Calorimeter Group, "The H1 liquid Argon calorimeter system"
Nucl. Instr. Meth. A **336** (1993) 460

[42] H. Henschel and R. Lahmann, Nucl. Instrum. Meth. A **453** (2000) 93.

[43] F. Sauli,CERN 77-03 sowie "Principles of MWPC and Dirft Chambers", in T. Ferbel, "Experimental Techniques in High Energy Physics".

[44] S. Eichenberger *et al.*, Nucl. Instrum. Meth. A **323** (1992) 532.

[45] R. D. Appuhn *et al.* [H1 SPACAL Group Collaboration], Nucl. Instrum. Meth. A **386** (1997) 397.

[46] T. Nicholls *et al.* [H1 SPACAL Group Collaboration], Nucl. Instrum. Meth. A **374** (1996) 149.

[47] Janoth et al, Nucl. Instr. Meth. A **350** (1994) 221
"Series Tests of Fine Mesh Photomultiplier tubes in Magnetic Fields of up to 1.2 Tesla"
DESY Report 97-70, Nucl. Instrum. Meth. A **404** (1998) 265

[48] H. Hutter, "Teststrahl-Untersuchungen an einem Sphaghetti-Kalorimeter für den H1-Detektor", http://www-h1.desy.de/psfiles/theses/h1th-049.ps Diplomarbeit, Universität Dortmund, (1995)

[49] D. Reyna, "Modifications to SpaCal for H1 High Luminosity Operation and the Effect on Acceptance", H1-11/98-555 (H1 interner Bericht).

[50] M. Domke, "Technische Zeichnungen des neuen Inserts",
http://e5pc51.physik.uni-dortmund.de/H1/Neues-Insert/neues_insert.html .

[51] B. Andrieu *et al.* [H1 Calorimeter Group Collaboration], Nucl. Instrum. Meth. A **336** (1993) 460.

[52] B.Schwab, "Das Rückwärtsdiftkammersystem des H1-Experiments", Dissartation, Universität Heidelberg, (1996). http://www-h1.desy.de/psfiles/theses/h1th-236.ps

[53] H.Beck et al, "Principles and operation of the z-vertex Trigger"
H1 Internal note, H1-05/96-479

[54] P. Biddulph *et al.*, Nucl. Instrum. Meth. A **340** (1994) 304.

[55] T. Ahmed *et al.*, Nucl. Instrum. Meth. A **364** (1995) 456.

[56] H. Bethe, W. Heitler, Proc. Roy. Soc. **A146** (1934) 83.

[57] S. Egli *et al.*, "Calculating Event Weights in Case of Downscaling on Trigger Levels 1–4", H1-04/97-517 (H1 interner Bericht).

[58] T.Ahmed et al, H1 Collaboration, Z. Phys. C **66** (1995) 529

[59] N. Gogitidze, Lebedev S. Levonian, H1 Internal Note, H1-02/96-471

[60] K.Piotrzkowski, "Experimental Aspects of the Luminosity measurement in the ZEUS experiment", PhD thesis,Institute of Nuclear Physics, Cracow Poland, 1993

[61] S. Levonian private communication, June 2006

[62] D. Wegener, HC Schulz Coulon, "Teilchendetektoren", Vorlesungsskript, Universität Dortmund, 2003

[63] H. C. Schultz-Coulon, E. Elsen, T. Nicholls, J. Coughlan and H. Rick, IEEE Trans. Nucl. Sci. **46** (1999) 915.

[64] H.Rick et al,"Calculating event weights in case of downscaling on tigger levels 1-4"
H1 internal note, H1-04/97-517 (1997)

[65] H1 Collaboration, "Guide to the simulation program H1SIM", H1 Software note 3 (1989)

[66] H1 Collaboration, H1rec user guide, unpublished

[67] R.Brun F. Carminati,"GEANT Detector description and simulation tool", CERN Program library W5013 (1993)

[68] G.A. Schuler and H.Spiesberger, Proc. Whorshop on HERA physic, edited
by W.Buchmuller and G. Ingelman (DESY, Hamburg, 1992), vol. 3, p.1419
DJANGO Manual,http://wwwthep.physik.uni-mainz.de/ hspiesb/djangoh/djangohs.html

[69] A.Kwiatkowski, H.Spiesberger, H.J.Mohring, Comp. Phys. Commun. **69** 155 (1992)
M.Boehm, H.Spiesberger, Nucl. Phys. B **294** (1987) 1081

[70] LEPTO 6.51 manual LEPTO 6.51 manual,http://www3.tsl.uu.se/thep/lepto

[71] L. Lönnblad, Ariadne version 4.12 program and manual, Comp. Phys. Commun. **71** (1992) 15
ARIADNE manual,http://www.thep.lu.se/ leif/ariadne/index.html

[72] G.Gustafson andU.Petterson, Nucl. Phys. B **306** (1988) 741
B.Anderson et al, Z. Phys. C **43** (1989) 625

[73] A.Muecke,R.Engel,J.P.Rachen,R.J.Protheroe and T.Stanev,
Comp. Phys. Commun. 124 (2000) 290,astro-ph/9903478

[74] R.Engel and J.Ranft, Phys. Rev. D **54** (1996) 4244
see also, PhD.,Ralph Engel, "Hadronic interactions of photons at high energies"
Universitaet-Gesamthochschuule-Siegen http://www-ik.fzk.de/ engel/phojet.html

[75] T.Sjoestrand and M.Bengtsson, Comp. Phys. Comm. **43** (1987) 367

[76] A.Blondel, F.Jacquet, "Proocedings of the Study of an *ep* facility for Europe", ed. A.Amaldi, DESY 79/48 (1979) 391

[77] Ursula Bassler, Gregorio Bernardi, Nucl. Instrum. Meth. A **361** (1995) 197
hep-ex/9412004

[78] Roman Poeschl, "Untersuchung der Ortsaufloesung des H1-Spaghetti-Kalorimeters unter besonderer Berueecksichtigung grosser Einschusswinkel der Primaerteilchen",
Diploma thesis,University of Dortmund, 1996
http://www-h1.desy.de/psfiles/theses/h1th-060.ps

[79] H1-H1rec routine

[80] J.Janoth, J.Stiewe, A.Meyer, H1 internal note H1-11/95-464
"An algorithm to calibrate the new H1 backward calorimeter SpaCal using the kinematic peak"

[81] J.Janoth and S.Schleif, "SpaCal monitoring with LED and their calibration" https://www-h1.desy.de/idet/icalo/spacal/notes/calib.notice3 .

[82] M. Dirkmann , H1 internal note H1-05/96-477,"Calibration of the SpaCal with Cosmics"

[83] Carsten Arndt, " Kalibration des H1 Spaghetti-Kalorimeter mit Halo Myonen",
Diploma Thesis, Universität Hamburg (1995)
http://www-h1.desy.de/psfiles/theses/h1th-031.ps

[84] A. Yuille et al, Harvard Robotics Laboratory Technical report no90-7 (1990)

[85] R.Wallny,"A Measurement of the Gluon Distribution in the Proton and of the Strong Coupling Constant alpha's from Inclusive Deep-Inelastic Scattering", PhD thesis,Univ. Zuerich,2001
http://www-h1.desy.de/psfiles/theses/h1th-284.ps

[86] H1 SpaCal group, Nucl. Instr. Meth. A **382** (1996) 395

[87] A.Zhokin and V.Efremenko, Minutes of ELAN DESY PWG. Meeting, 28.7.1995

[88] A. Meyer, "Measurement of the Structure Function $F2(x, Q^2)$ of the Proton at Low Q^2 with the H1 Detector at HERA Using the New Detector Components Spacal and BDC", PhD. Thesis, Hamburg, (1997)
http://www-h1.desy.de/psfiles/theses/h1th-084.ps.gz

[89] S. Glazov, "Measurement of the Proton Structure Functions $F_2(x, Q^2)$ and $F_L(x, Q^2)$ with the H1 Detector at HERA", PhD. Thesis, Berlin, Humboldt-University, (1998)
http://www-h1.desy.de/psfiles/theses/h1th-116.ps

[90] V.V. Arkadov, "Measurement of the Deep-Inelastic ep scattering cross section using the Backward Silicon Tracker at the H1 detector at HERA", PhD thesis, Humboldt-University Berlin, (2000)
http://www-h1.desy.de/psfiles/theses/h1th-226.ps

[91] J. Gayler, Private communication, June 2006

[92] U. Bassler, G. Bernardi, H1 Software note, H1/51-95, "Reconstruction of kinematic variables inside H1REC"

[93] see also H1PHAN analysis code

[94] H1 Collab., C. Adloff et al., Z. Phys. C **74** (1997) 221

[95] H1 Collab., C. Adloff et al., Eur. Phys. J. C **13** (2000) 609

[96] H1 Calorimeter group, Nucl. Instrum. Meth. A **336** (1993) 460

[97] C. Issever, "Entwicklung eines alternativen Gewichts-verfahrens fuer das H1-Kalorimeter", Diplomarbeit, Universität Dortmund, 1996
http://www-h1.desy.de/psfiles/theses/h1th-037.ps

[98] C. Issever, K. Borras, D. Wegener, Nucl. Instrum. Meth. A **545** (2005) 803

[99] C. Issever, "Messung der Protonstrukturfunktionen $F_2(x, Q^2)$ und $F_L(x, Q^2)$ bei HERA in radiativer ep-Streuung", PhD thesis, Universitaet Dortmund, 2000
http://www-h1.desy.de/psfiles/theses/h1th-219.ps

[100] Olaf Behrendt, "Measurement of the Proton Structure Function F_2 at low Q^2 at HERA" PhD. thesis, Dortmund University, (2005)

[101] Rainer Stamen, "Measurement of Deeply Virtual Compton Scattering at HERA" PhD. thesis, Dortmund University, (2001)
http://www-h1.desy.de/psfiles/theses/h1th-249.ps

[102] Victor Lendermann, "Measurement of the QED Compton Scattering Cross Section with the H1 Detector at HERA" PhD. thesis, Dortmund University, (2001) http://www-h1.desy.de/psfiles/theses/h1th-252.ps

[103] H1 Collab., T. Ahmed et al., Nucl. Phys. B **435** (1995) 3

[104] PDFLIB: The parton density functions library, version 8.04, MRST set 75, CERN

[105] Tomas Lastovic,"Measurement of the Inclusive Deep Inelastic Scattering Cross Section at Low Q^2", PhD Thesis,Humbdolt University Berlin, 2004

[106] Paper in preparation, Measurement of the proton structure function for low values of Q^2.

Gracias!!!!!

..... a Dios por darme la vida la fuerza y el amor.

Sehr schön war die Zeit, die ich als Doktorandin am Lehrstuhl für Experimentelle Physik V (E5) gehabt habe, und deshalb will ich ganz herzlich danke sagen. Zuerst will ich Professor Wegener ganz besonders danken, mir die Möglichkeit gegeben zu haben, an seinem Lehrstuhl zu arbeiten und Forschen zu lernen.

Herrn Prof. Spaan danke ich für seine Bereitschaft, zweiter Gutachter meiner Arbeit zu sein. An dieser Stelle will ich Prof. Schulz-Coulon auch danke sagen, der immer die positive Seite von Problemen gesehen hat und dadurch eine optimistische Atmosphäre in meine Promotionszeit gebracht hat, danke Hans-Christian.

Natürlich gab es außer schönen Zeiten auch Frustration zu bewältigen, wobei mir die E5 Lehrstuhl Mannschaft sehr viel geholfen hat. In erster Linie das E5-F_2-Team, Olaf, Victor, Katja und Hans-Christian, die immer Zeit für meine "Bump"-Kreationen gehabt haben und mit großem Interesse bei vielen Gelegenheiten die Plots gemeinsam diskutiert haben. Außerhalb von E5 gehören zum F_2-Team Sasha Glazov, Alexey Petruskin und Ewelina Lobodzinska, die auch immer Zeit gehabt haben, um auf meine Fragen zu antworten. Zu Katja ein besonderes Danke, für die vielen konstruktiven Kommentare zu meiner Analyse und während des Zusammenschreibens. Zu allen Danke! Ohne Euch wäre diese Arbeit fast unmöglich gewesen!

Die gute Harmonie innerhalb der Gruppe zeichnet E5 besonder aus. Zuerst Olaf, der Autor von [100], mit dem ich immer eine "großes Tennis" Analysezeit gehabt habe, vielen Dank, Olaf, für Deine Hilfe und Deine Freundschaft. Die tolle Umgebung von E5 haben auch Marc-Oliver, Christoph, Victor, Mitch, Christopher, Martin, Katja, Klaus, Jesko, Stephan, Jörg, Andreas, Dirk, Moritz, Daniel, Michael und natürlich Kristin! geschaffen. Dank Euch allen dafür, daß Ihr mir die Stimmung vom Ruhrgebiet gezeigt habt.

Zu meiner lieben Familie auch Danke! Leider muss ich jetzt auf Spanisch schreiben sonst verstehen sie nichts: muchas gracias mami, papi, gordita y todos! por su comprension y cariño a

lo largo de mi vida y por la fuerza que me han dado a través de las largas conversaciones telefónicas. Espero pronto estar alla y entregarles mi tesis con un fuerte beso y abrazo. También espero que las gráficas de mi trabajo sean del agrado de mis queridos sobrinos y sobrinas.

Ein emotionales Danke gehört meinem Lieblings-Christoph, ohne Dich wäre meine Zeit nicht so schön gewesen, danke für's immer da sein und für Deine Liebe. Auch weil du machmal Frijoles und Chile zum Abendbrot essen mußtest, wenn ich ein bisschen Mexiko brauchte. Auch für Deine Geduld, um mein Español-Deutsch-English zu entschlüsseln. Der Leser meiner Arbeit wird es Dir danken. Jetzt fehlen uns nur die 6? Auch Familie Wissing bin ich sehr dankbar, "Mutti" H. Wissing und Henrike für die schöne und großartige Zeit zu Weihnachten, wo ich immer familiäre Wärme gefühlt habe.

Zu Elke ein spezielles Danke, Du bist einer meiner Engel in Deutschland gewesen. Vielen dank für Deinen Rat, Deine Briefe und Deine liebevolle Freundschaft. Zu Dieter, Jan und Moritz auch Danke dafür mir die Möglichkeit gegeben zu haben, ein Stückchen von Eurer Familie zu haben.

Und natürlich ein großes Danke an Dich Beate, für Deinen Rat und Deine Zeit, die Du immer für mich hast, seit ich nach Deutschland gekommen bin. Unsere Kuchenpausen werde ich nie vergessen und auch nicht unsere Diskussion über "Gott und die Welt". Ich hoffe, daß wir bald endlich zusammen ins Kino gehen können.

An dieser Stelle möchte ich auch gerne meinen Freunden und Geschwistern danken: Virginia, Marciano, Tere, Aurora, Sergio, Jesús, Miriam, Jóse, Hernán, Jacinta, Yvonne und "prima-"Lety, die trotz große Entfernung mir immer nahe waren, und mir immer E-mails geschickt haben, auch wenn ich fast "nie" zurückgeschrieben habe.

Zum Schluß, will ich dem DAAD und der Universität von Dortmund danken, ohne ihre finanzielle Unterstützung wäre mein Studium in Deutschland vollig ummöglich gewesen. Außerdem will ich mich bei den Professoren in Mexiko A. Zepeda, G. Herrera und G. Contreras für ihren Rat und ihre Gutachten bedanken.

Diese Arbeit wurde mit Mitteln des Bundesministeriums für Bildung und Forschung unter der Projektnummer 05 H1 4PEA/6 gefördert.